Nanoscale Modification of Copper for Novel Methanol and Water-Gas Shift Catalysts

Schumacher, Nana Maria Pii

Publication date:
2008

Document Version
Publisher's PDF, also known as Version of record

Ph.D. thesis

Center for Individual Nanoparticle Functionality
Department of Physics
Technical University of Denmark

Nanoscale Modification of Copper for Novel Methanol and Water-Gas Shift Catalysts

Nana Maria Pii Schumacher

August 2007

Preface

This thesis is submitted in candidacy for the Ph.D. degree from the Technical University of Denmark, DTU. Funding was supplied by DTU, Haldor Topsøe A/S, and the Copenhagen Graduate School for Nanoscience and Nanotechnology. The presented work was done from August 2004 to August 2007 at the Interdisciplinary Research Center for Catalysis, ICAT, and Center for Individual Nanoparticle Functionality, CINF, at the Department of Physics under the supervision of Professor Ib Chorkendorff, CINF, and Dr. Jesper Nerlov, Haldor Topsøe A/S, whom I thank for their inspiration and assistance.

I would also like to thank Professor Manos Mavrikakis and Ph.D. student Lars Grabow from University of Wisconsin-Madison for the joint work on the vibrational aspects of adsorbed carbonate. Discussions of the experimental data and theoretical insight on the behavior of carbonate in connection with Cu and Pt systems were invaluable. Furthermore, I had the pleasure of collaborating with Ph.D. Søren Dahl, Ph.D. Astrid Boisen, and Dr.Ir. Ton Janssens, Haldor Topsøe A/S on studies of the water-gas shift reaction.

In connection with the overhaul of the experimental chamber and everyday maintenance, several people played an important role. I would like to thank Assistant Professor Martin Johansson and Technical Assistant John Larsen for help and advice, as well as Hans-Christian Sørensen and Dan Schacham from the workshop who manufactured anything from custom gaskets up to a new manipulator rod and made useful comments about the resale value of stainless steel from UHV chambers. Furthermore, I thank Poul Andersen for his help in connection with troubleshooting and repair of the control boxes.

I enjoyed working with Ph.D. Michael Andersen who taught me to operate and maintain the equipment, and Ph.D. Klas Andersson, whom I thank for excellent team work during the last six months of my studies as well as proof reading together with Ph.D. Jakob Engbæk. A huge thanks goes out to all of my friends and colleagues for the unique social atmosphere, and last but not least, my husband Ph.D. student Torsten Lund for his loving support during a time when he was busy with his own thesis.

Nana Maria Pii Schumacher
Kgs. Lyngby, August 2007

Summary

This thesis consists of two parts. The first addresses the interaction of CO_2 and H_2 with pseudomorphic and rough copper overlayers deposited on a platinum (111) single crystal, whereas the second part focuses on computational and experimental investigations of the reactivity trends for low temperature water-gas shift over several transition metals.

Evidence for dissociative adsorption of CO_2, carbonate formation, carbonate hydrogenation, and formate synthesis under high pressure is presented and the relevance to methanol synthesis is discussed. Intermediates are identified using in situ polarization modulation infrared reflection absorption spectroscopy at pressures up to 500 mbar and electron energy loss spectroscopy in ultra-high vacuum. The observed vibrational modes of carbonate are consistent with a tridentate configuration lying nearly flat on the surface. Density functional theory studies present steps and defects as the likely sites for carbonate adsorption, and reproduce the observed vibrational frequencies.
Temperature programmed desorption reveals a broad desorption state for CO_2 peaking around 450 K for 1 ML Cu, and X-ray photoelectron spectroscopy shows that approx. one third of the oxygen accumulated on the surface upon CO_2-exposure remains after TPD, indicative of carbonate decomposition. Furthermore, it is observed that small amounts of preadsorbed atomic oxygen significantly lowers the activation barrier for carbonate formation.
The hydrogenation of carbonate has been monitored with XPS as well as TPD, and a considerable CO_3 loss is found when it is subjected to 0.2 bar H_2 at room temperature. The presence of formate is not clearly observed, possibly due to rapid hydrogenation of the formate species itself.
Formate synthesis from a 0.5 bar gas mixture of 70 % CO_2 and balance H_2 has been shown to occur on Cu/Pt(111) with an optimal temperature around 353-363 K. Formate decomposes into CO_2 and H_2 at 415 K for 1 ML Cu, which is slightly lower than previously reported on low-index Cu surfaces, but in good agreement with studies on Cu-based catalysts. This suggests the reactivity of the stretched Cu is significantly different compared to Cu(111). At higher Cu coverages (4.4 ML) only small amounts of formate is synthesized and carbonate is present.

Low-temperature water-gas shift reactivity trends on transition metals are investigated with the use of a microkinetic model based on a redox mechanism. It is established that the adsorption energies for carbon monoxide and oxygen to a large extent can describe

changes in the remaining activation and adsorption energies through linear correlations. It was sought to reduce the number of descriptors to one reduced energy by employing a relationship between the binding energies of atomic oxygen and carbon monoxide. The behavior of the reaction rate is, however, too complicated to be described in a simple way using a single descriptor.

When comparing the results with experimental data it is found that the model predicts the order of catalytic activities for transition metals fairly well, although it fails to quantitatively describe the experimental data. This discrepancy could be due to the assumption that the redox mechanism dominates and to the neglect of adsorbate interactions. The model predicts that the activity of copper may be improved by increasing the binding strengths of carbon monoxide and oxygen to the surface, thus suggesting possible directions for improving the catalyst.

Water-gas shift activity measurements for several transition metals supported on inert $MgAl_2O_4$ are correlated to the binding energies of atomic oxygen and carbon monoxide to elucidate the modeling results. It is found that the metals may be divided into a group with weak CO adsorption and one with strong CO adsorption. The experimental results suggest that the activity could be further improved by modifying the Cu catalyst such that the oxygen adsorption strength is increased, while keeping the CO adsorption fairly unaffected.

Resumé

Denne afhandling består af to dele. Den første omhandler interaktionen af CO_2 og H_2 med pseudomorfiske og ujævne kobber-overlag deponeret på en platin (111) én-krystal, mens den anden del fokuserer på beregningsmæssige og eksperimentelle undersøgelser af reaktivitetstrends for lav-temperatur vand-gas skift over adskillige overgangsmetaller.

Beviser for dissociativ adsorption af CO_2, karbonat-dannelse, karbonat-hydrogenering og formatsyntese ved højt tryk præsenteres, og relevansen for metanolsyntesen diskuteres. Intermediære molekyler identificeres ved anvendelse af in situ polarisationsmoduleringsinfrarød-reflektions-absorptions-spektroskopi ved tryk op til 500 mbar samt elektronenergitabs-spektroskopi i ultrahøjt vakuum. De observerede karbonat-vibrationer er i overensstemmelse med en tridentat konfiguration, som ligger næsten fladt på overfladen. Densitetsfunktionaleteori-studier viser, at trin og defekter er sandsynlige steder for karbonatadsorption, og reproducerer endvidere frekvenserne for de observerede vibrationer.
Det konstateres med temperatur-programmeret-desorption, at CO_2 desorberer i et bredt område med en top omkring 450 K for 1 ML Cu, og røntgen-fotoelektron-spektroskopi viser, at ca. en tredjedel af ilten, der blev ophobet på overfladen under CO_2-påvirkningen er forblevet der efter TPD, hvilket indikerer karbonat-dekomponering. Det er endvidere blevet observeret, at små mængder af præadsorberet atomar ilt sænker aktiveringsbarrieren for karbonat-dannelse signifikant.
Hydrogeneringen af karbonat er blevet fulgt med XPS samt TPD, og et betydeligt CO_3 tab findes, når prøven udsættes for 0.2 bar H_2 ved stuetemperatur. Tilstedeværelsen af format er ikke tydeligt observeret, sandsynligvis på grund af en hurtig hydrogenering af formaten selv.
Formatsyntese ud fra en 0.5 bar blanding af 70 % CO_2 og 30 % H_2 er påvist på Cu/Pt(111) med en optimal temperatur omkring 353-363 K. Format dekomponerer til CO_2 og H_2 ved 415 K for 1 ML Cu, hvilket er en smule lavere end hvad der førhen er rapporteret for lav-indeks Cu overflader, men i god overensstemmelse med studier af Cu-baserede katalysatorer. Dette tyder på, at reaktiviteten af det modificerede kobber er signifikant anderledes i forhold til Cu(111). Ved større Cu-mængder (4.4 ML) bliver kun små mængder format syntetiseret, og karbonat er til stede.

Lav-temperatur vand-gas skift reaktivitetstrends på overgangsmetaller undersøges ved at anvende en mikrokinetisk model baseret på en redox-mekanisme. Det påvises, at adsorptionsenergierne for kulilte og ilt i høj grad kan beskrive ændringer i de andre aktiverings-

og adsorptionsenergier gennem lineære korrelationer. Det er blevet tilstræbt at reducere antallet af deskriptorer til en reduceret energiparameter ved at beskrive en sammenhæng mellem bindingsenergierne for atomar ilt og kulilte. Imidlertid er reaktionshastighedens adfærd for kompliceret til at kunne beskrives på en simpel måde ved brug af en enkelt deskriptor.
Ved sammenligning af resultaterne med eksperimentelle data findes det, at modellen forudsiger rangordenen for de forskellige katalytiske aktiviteter af overgangsmetallerne glimrende, selvom den fejler ved den kvantitative beskrivelse af de eksperimentelle data. Denne uoverensstemmelse kan stamme fra antagelserne om, at en redox-mekanisme dominerer, og at adsorbatinteraktioner kan negligeres. Modellen forudsiger, at aktiviteten af kobber kan forbedres ved at forhøje bindingsstyrken af kulilte og ilt til overfladen, hvilket afdækker muligheder for at forbedre katalysatoren.
Vand-gas skift aktivitetsmålinger for adskillige overgangsmetaller på et inert $MgAl_2O_4$-underlag korreleres til bindingsenergierne af atomar ilt og kulilte for at belyse modelleringsresultaterne. Det findes, at metallerne kan inddeles i en gruppe med svag CO adsorption og en med kraftig CO adsorption. De eksperimentelle resultater tyder på, at aktiviteten kan forbedres ved at modificere Cu-katalysatoren således, at ilt-adsorptionsstyrken forhøjes, mens styrken af CO-adsorptionen forbliver stort set uændret.

Abbreviations

AES	Auger Electron Spectroscopy
BEP	Brøndsted-Evans-Polanyi
DFT	Density functional theory
EELS	Electron energy loss spectroscopy
FTIR	Fourier transform infrared spectroscopy
FWHM	Full width half maximum
HPC	High pressure cell
IMFP	Inelastic mean free path
ISS	Ion scattering spectroscopy
L	Langmuir ($1 \cdot 10^{-6}$ torr·s)
LEED	Low energy electron diffraction
ML	Monolayer
PM-IRRAS	Polarization modulation infrared reflection absorption spectroscopy
PW91	Perdew-Wang 91
QMS	Quadrupole mass spectrometer
QE	Quasi equilibrium
RCS	Rate controlling step
RPBE	Revised Perdew-Burke-Ernzerhof
RWGS	Reverse water-gas shift
STM	Scanning tunneling microscopy
TOF	Turn-over frequency
TPD	Temperature programmed desorption
UHV	Ultra-high vacuum
WGS	Water-gas shift
XPS	X-ray photoelectron spectroscopy

Contents

Chapter 1

Introduction

1.1 The surface science approach to heterogeneous catalysis

The modern chemical and petrochemical industry is widely dependent on heterogeneous catalysis. Areas of application include the production of fertilizers, cracking and desulphurization of oil, as well as pollution reduction.
A catalyst is a substance that without being consumed itself facilitates the progression of a reaction. It does not alter the equilibrium, but merely lowers the activation barrier, thus increasing the reaction rate. A typically heterogeneous catalyst consists of nano-sized metal particles on an oxide support. When utilizing these materials in an industrial production, there are however several issues that must be addressed, as limited particle stability, poisoning by impurities in the reactants feed, or blocking of active sites by the deposition of carbon may lead to deactivation. Furthermore, the cost of the process may be reduced significantly if the activity and selectivity toward a certain product are improved.

The main objective in surface science both theoretically and experimentally is to obtain insight into what determines the reactivity of a given catalyst and to understand the mechanism, which describes the elements of the catalyzed reaction. These steps will typically consist of adsorption of reactants, dissociation, recombination, and finally the desorption of products from the catalyst. This provides insight into how materials should be engineered, and will hopefully remove some of the tedious trial and error experiments which have been and to some extend still are the only means of finding new and improved catalysts.
Computational tools such as density functional theory (DFT) [1] which is a quantum mechanical method used to study the electronic structure of many-body systems, and microkinetic modeling [2, 3] where a mathematical description of the basic surface processes is obtained by utilizing statistical mechanics, have been applied to search for new catalysts. This has recently led to the proposal of novel materials for the hydrogen evoulution reaction [4], and CO methanation [5].
In experimental surface science the typical model system is a metal single crystal with

a well-defined lattice facet exposed. Although studies of the interaction of different high purity gases with these model surfaces may to some extend yield information about the reaction mechanisms, the conditions under which the experiments are conducted are far from the industrial processes, which often take place at high pressures (20 bar and above). Experimental surface science mostly applies ultra-high vacuum in the $1{\cdot}10^{-10}$ to the $1{\cdot}10^{-5}$ mbar range, as electrons and ions are used to probe the sample. Recent advances have improved methods such as X-ray photoelectron spectroscopy (XPS) and transmission electron microscopes (TEM) enabling them to go to several mbar [6, 7], but in order to examine systems under ambient conditions, infrared spectroscopy must be employed.
Both experimental and computational investigations of the water-gas shift (WGS) reaction as well as the methanol synthesis will be presented in this thesis. The two processes are summarized in the next section together with a presentation of research within the fields.

1.2 Water-gas shift reaction and methanol synthesis

The water-gas shift reaction is an important component of several industrial processes. It is mainly used for the production of high-purity hydrogen, which is needed for e.g. ammonia synthesis. In industrial applications the reaction is run at pressures around 25-35 bar. To achieve the highest feasible conversion, two adiabatic stages with cooling in between are applied [8]. A high temperature stage at 580-720 K with a catalyst based on iron oxide structurally promoted with chromium oxide is followed by a low temperature stage in the range 480-510 K, where the typical industrial catalyst is copper with zinc oxide and aluminum oxide. The copper catalyst undergoes deactivation at temperatures higher than 570 K, as the copper particles sinter because of surface migration [9].

$$\begin{aligned} &\mathrm{CO} + \mathrm{H_2O} \rightleftharpoons \mathrm{CO_2} + \mathrm{H_2} \\ &\Delta H^o_{298K} = -41 \text{ kJ/mol} \end{aligned} \tag{1.1}$$

In recent years there has been renewed interest in the WGS reaction in connection with fuel cell-powered vehicles, where hydrogen is obtained through partial oxidation and steam reforming of hydrocarbons. The reformed fuel contains 1-10% CO [10], which apart from being a pollutant, also poisons the Pt anode in the fuel cell, because of its strong adsorption to the electrode surface [11]. Lowering of the CO content is limited by the reaction equilibrium at the operating temperature of the conventional $Cu/ZnO/Al_2O_3$ catalyst in the reformer system. The development of a more active catalyst would allow one to achieve a higher conversion and reduce the volume and hence the weight of the system.

Water-gas shift is also an inherent part of methanol synthesis, which is performed in the temperature range 500-550 K and at pressures between 50 and 100 bar over the same $Cu/ZnO/Al_2O_3$ catalyst. The latter was introduced by ICI in 1966 [12], replacing the less active ZnO/Cr_2O_3 catalyst developed by BASF, which required substantially higher

temperature and pressure (300 bar and above 600 K) [13].

The by far largest use for methanol is in the manufacture of a variety of chemical compounds. These include the petrol additive methyl tert-butyl ether ($CH_3OC(CH_3)_3$) abbreviated MTBE, dimethyl ether (CH_3OCH_3) abbreviated DME, formaldehyde (CH_2O), and acetic acid (CH_3COOH), which in turn are used in the production of polymers, paints, and solvents.
Emerging areas of application include the usage of methanol as a turbine fuel for electric power generation due to a reduction of NO_X and a removal of SO_2 emission. Furthermore, methanol is added to wastewater as it speeds up the bacterial degradation of harmful nitrates [14]. It is also an effective energy carrier, as it is an excellent basis chemical for the production of hydrogen, which may in turn be used in fuel cells. Methanol may however also be employed as a fuel in direct methanol fuel cells (DMFC).

The synthesis gas is made by steam reforming (1.2) of natural gas and the water-gas shift reaction (1.1) over Ni-based catalysts.

$$\begin{aligned} C_nH_m + nH_2O &\rightleftharpoons nCO + (n + \frac{m}{2})H_2 \\ \Delta H^o_{298K} &> 0 \text{ kJ/mol} \end{aligned} \tag{1.2}$$

A non-stoichiometric ratio of 5% CO, 5% CO_2, and 90% H_2 is typically used for the methanol synthesis. The overall reaction scheme (1.3) may be written as the hydrogenation of carbon monoxide,

$$\begin{aligned} CO + 2H_2 &\rightleftharpoons CH_3OH \\ \Delta H^o_{298K} &= -91 \text{ kJ/mol} \end{aligned} \tag{1.3}$$

but in reality the synthesis should be depicted as the hydrogenation of CO_2 (1.4) combined with the water-gas shift reaction (1.1). The WGS reaction runs much faster than the synthesis and must be taken into the equilibrium considerations for the overall reaction [15].

$$\begin{aligned} CO_2 + 3H_2 &\rightleftharpoons CH_3OH + H_2O \\ \Delta H^o_{298K} &= -47 \text{ kJ/mol} \end{aligned} \tag{1.4}$$

Reviews of work on methanol synthesis and decomposition have been done by Klier [16], Waugh [17], Nakamura et al. [18], Liu et al. [19], as well as Rozovskii and Lin [20].

1.2.1 Reaction mechanism

It has been a much debated topic whether the reaction takes place with CO or CO_2 as the source of carbon for methanol. Isotope labeling experiments have however shown that methanol is formed from CO_2 [21, 22], and Chorkendorff and coworkers have demonstrated that methanol can be produced from a mixture of H_2 and CO_2 at up to 4 bar over a Cu(100) single crystal [23, 24]. Bowker et al. [25] furthermore described the CO_2 hydrogenation as the general path to methanol.
The activation and successive hydrogenation of CO_2 to formate (HCOO) have been suggested to proceed through the reaction of either adsorbed or gaseous CO_2 and adsorbed atomic hydrogen [26, 27]. Furthermore, a carbonate (CO_3) may be created by the interaction of surface oxygen formed from dissociative adsorption of CO_2 with another CO_2 molecule. The presence of carbonate and its hydrogenation to formate have been shown by Waugh and co-workers [28, 29, 30]. Whereas the reaction of adsorbed CO_2 and H_2 have been adapted in microkinetic models [26, 31], the carbonate route has been given almost no attention [32].
The production of methanol from carbon dioxide and hydrogen is believed to proceed through a number of hydrogenation steps from formate to methoxy (CH_3O) and finally to methanol [18, 25, 26, 33]. The assignment of the rate controlling step as well as the presence of different intermediates and hydrogenation products are however discussed [23, 34].
It is clear that controversy still exists about the reaction mechanism of methanol synthesis on the industrial $Cu/ZnO/Al_2O_3$ catalyst [19], and as will be seen in the next section, the involvement of different sites. In this report, focus will however be on the activation of CO_2 and subsequent hydrogenation to formate. Different mechanisms relevant for the water-gas shift reaction will be presented in chapter 7.

1.2.2 The Cu-Zn synergy

The $Cu/ZnO/Al_2O_3$ catalyst is comprised of nano-sized copper clusters supported on zinc oxide and aluminum oxide, where the latter is believed to be rather inactive. In spite of a great number of studies, the nature of the active sites for methanol synthesis and the role of the ZnO-support are still subjects of debate. It is known that the combination of Cu and ZnO increases the reactivity and that the dynamics of nano-sized particles are central for the understanding of this system [35]. Different suggestions for the active site (metallic Cu or special site model) as well as the role of ZnO (morphology, spillover, or Cu-Zn alloy model) are presented by Dulub et al. [36] and reviewed by Nakamura et al. [18] as well as Liu et al. [19].

That metallic Cu serves as the active site has been supported by Chinchen et al. [37], who reported a linear relationship between the activity and the total Cu surface area, and found that Cu on other supports than ZnO/Al_2O_3 exhibited comparable rates to the Cu-Zn system. Rasmussen et al. [23] as well as Yoshihara et al. [38, 39] also found that

the reactivity of Cu surfaces could explain the rates observed for industrial catalysts.
It has furthermore been established that the methanol synthesis is structure dependent, and Yoshihara et al. [38, 39] concluded that the Cu(110) facet is the most active for synthesis. This was supported by Nakamura and co-workers [40] who studied methanol synthesis by the hydrogenation of CO_2 over several Cu facets and found that the density of different Cu facets was correlated to the reactivity for methanol synthesis. The activity decreased in the order (110) > (311) > (100) > (111).
Topsøe and Topsøe [41] also found that the active copper species during synthesis with mild reducing conditions is metallic and predominantly exposes the (110) facet. Varying reduction potential of the gas however influences the nature of the Cu surfaces in Cu/ZnO reversibly, including the formation of a CuZn surface alloy at severe reducing conditions. The observation of alloy formation has been further investigated by Greeley et al. [42] utilizing DFT calculations.

Different variations of the special site model with active sites such as Cu^+, Cu-Zn, or Cu-O-Zn have also been proposed. The existence of Cu^+ in a ZnO matrix has been supported by Klier and co-workers [16, 43, 44], whereas Okamoto et al. [45] concluded that the active site is a Cu^0-Cu^+ species forming a two-dimensional epitaxial layer on the ZnO support. Furthermore, the presence of Schottky junctions between copper and the oxide has also been reported to affect the catalytic behavior [46].
The active Cu-Zn site is supported by Nakamura and co-workers, who found that two different sites are active for CO and CO_2 hydrogenation, respectively [18]. In industrial catalysts the formation of a Cu-Zn surface alloy is responsible for the promotion of methanol synthesis activity from the hydrogenation of CO_2 due to the creation of a Cu-Zn site [47, 48, 49], whereas the CO hydrogenation occurs on a Cu^+ site or a Cu-O-Zn site [18].

The influence of the ZnO on the activity has apart from the alloy formation been suggested to be due to a change in morphology of the Cu particles thus exposing facets with different activities. In an oxidizing environment, non-wetting conditions arise and the Cu particles will obtain a spherical shape, whereas a reducing environment results in wetting of the Cu particles [50, 51] leading to a flat, disc-like shape with a large surface area where the most active (110) facet is exposed [39, 41]. These conclusions have been supported by studies of the behavior of the catalyst with and without the Zn component [52].
Günter et al. [53] furthermore established that the ZnO support induces a strain in the Cu nanoparticles, which leads to an improvement of the reaction rate, and these findings were later confirmed by Wagner et al. [51]. The morphology model has also been supported by a microkinetic model taking changes in the particle shape into account [31].

The last suggestion, the spillover model, depicts a situation where ZnO acts as a reservoir and site for H_2 dissociation, as suggested by Spencer and co-workers [54, 55]. Hydrogen may then spillover to the Cu and aid in the hydrogenation of intermediates. This does however not influence metallic Cu as the site for CO_2 hydrogenation.

1.3 Objective and outline

The overall purpose of this work has been to obtain a more detailed understanding of the reactivity of Cu-based catalysts for the water-gas shift reaction and the methanol synthesis by means of both experimental and computational work.
The model system chosen is a bimetallic system comprised of pseudomorphic copper overlayers grown on a platinum (111) single crystal which due to the induced stretching of the Cu lattice represents a modified and more reactive Cu(111) surface. Especially the role of CO_2 and its activation for methanol synthesis is given attention. In order to bridge the inevitable pressure gap that ultra-high vacuum experiments create compared to industrial processes, surface species are identified at both high pressure conditions and in UHV using in situ polarization modulation infrared reflection absorption spectroscopy, abbreviated PM-IRRAS.
The inspiration for making copper more reactive came from recent work on a microkinetic model describing the reactivity of the water-gas shift reaction on several transition metals [56]. This model is presented together with further investigations and experiments performed on the WGS reaction. The gained fundamental insight may potentially constitute the basis for the development of a new generation of methanol and water-gas shift catalysts.

The outline of this thesis is as follows. Chapter 2 contains a description of the experimental setup, and chapter 3 summarizes the surface science methods, which have been applied in this project. Chapter 4 is dedicated to the theory behind polarization modulation infrared reflection absorption spectroscopy as well as the description of the setup. Due to the relevance when interpreting vibrational spectroscopy spectra, a brief overview of vibrational theory, and the effect of adsorption upon the vibrational modes as well as the interaction with infrared radiation are presented in chapter 5.
The experimental and computational results for CO_2 and H_2 interaction with the bimetallic Cu-Pt system are described and discussed in chapter 6, whereas the microkinetic model of the water-gas shift reaction, as well as an analysis of experimental results in connection with the conclusions of the theoretical work are presented in chapter 7. Finally, an overall conclusion and an outlook for the systems are given in chapter 8. Papers and manuscripts written during the project period may be found at the end of this thesis after the bibliography.

Chapter 2

The experimental setup

2.1 Apparatus

The experimental setup consists of an ultra high vacuum (UHV) chamber with a base pressure of approx. $1 \cdot 10^{-10}$ torr as well as a high pressure cell (HPC). They can be separated with a lock that utilizes a Cu-gasket [57], which makes it possible to run reactions at several bar in the cell, while maintaining UHV conditions in the main chamber. A vertical manipulator allows transfer of a sample between the two compartments. The setup is shown alongside a schematic overview in figure 2.1.

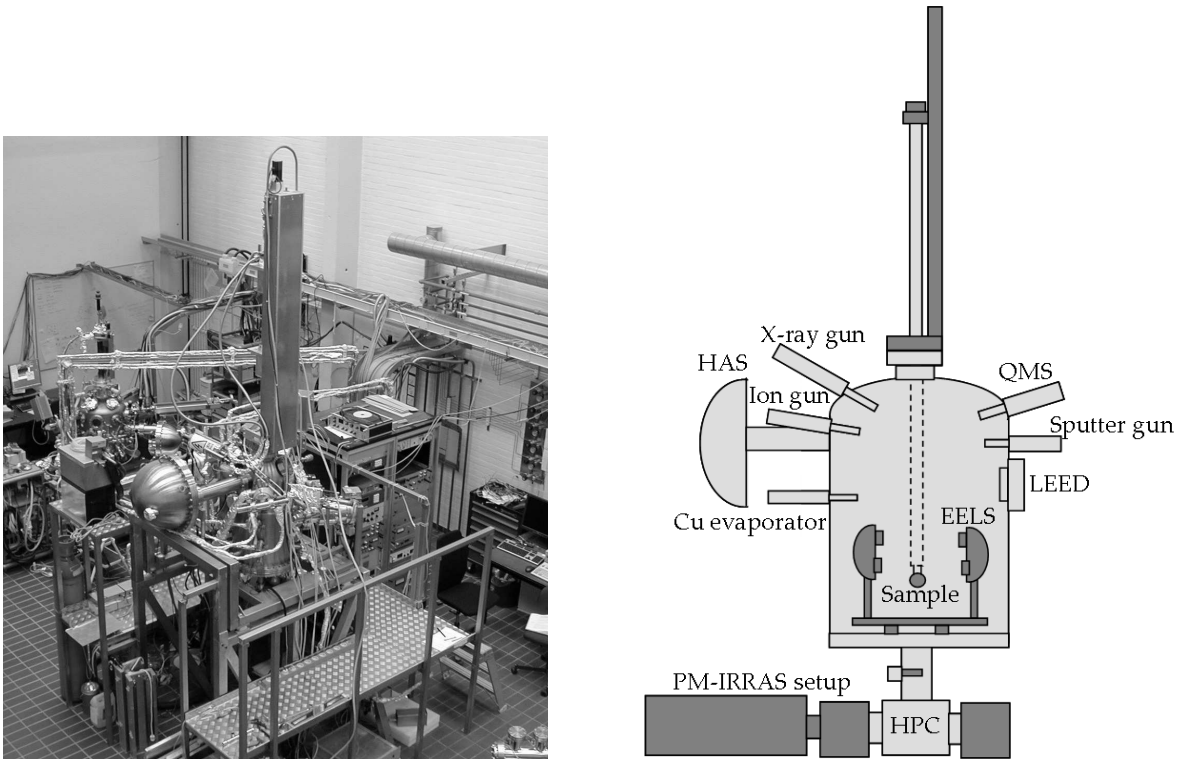

Figure 2.1: The experimental setup.

The HPC and the flanges mounted on it are made of Arne steel to prevent formation of nickel carbonyls when applying high pressures of CO. To accommodate an infrared spectroscopy installation, the cell is fitted with ZnSe windows supplied by SOREM that allow for transmission of infrared radiation, and the geometry of the cell is such that the radiation can be reflected of the metal crystal with an angle of 82° between the beam and the surface normal. The HPC can withstand pressures of up to 5 bar, which is limited by the ZnSe windows and bellows. A sniffer that is connected to a quadrupole mass spectrometer (QMS) mounted on the UHV chamber is installed in order to follow gas phase concentration changes during reaction.

The main UHV chamber is equipped with metal evaporators (at present Cu and Ag), as well as several standard surface science techniques which are presented in the next chapter. The chamber is pumped by two turbopumps with capacities of 240 l/s and 500 l/s, respectively. The small pump is also used for differential pumping of the quadrupole mass spectrometer and the ion gun. Two ion pumps, both 25 l/s capacity, are used for differential pumping of an X-ray gun and of the rotational platform for the manipulator. A titanium sublimation pump is also fitted, but currently not in operation.

The sample is a platinum single crystal supplied by Metal Crystals & Oxides Ltd. cut in the (111) direction with a diameter of 10 mm and a thickness of 3 mm, see figure 2.2. It is mounted using a hairpin-shaped 0.5 mm tungsten wire which is fastened onto the feed-throughs on the manipulator end. The thermocouple wires are secured in a hole in the crystal with several pieces of tungsten wire. By applying up to 30 A the sample may be heated resistively to above 1500 K. Cooling is achieved by pumping pressurized air, ethanol or liquid nitrogen into the hollow manipulator. With pressurized air 300 K is reached, ethanol yields about 265 K, and liquid nitrogen cools the crystal down to approx. 80 K. Sample heating, movement of the manipulator, and various other control functions are handled using software written in Labview.

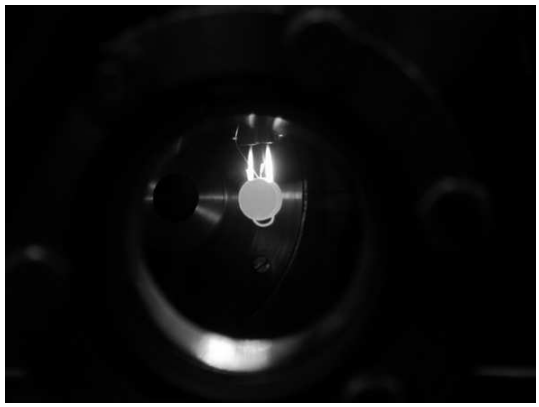

Figure 2.2: The Pt crystal mounted onto the manipulator.

The setup was overhauled during the time period where the presented experiments were conducted. The manipulator rod was replaced, as the thermocouple had to be changed from the nickel-free type C[1] to type K[2] due to the limited low temperature range of type C. The design of the manipulator was also changed, and the cabling to the actuators was revised in order to prevent accidental cutting of cables during movement of the sample.

2.2 Gas inlet system

The gas inlet system is pumped with a small 240 l/s turbo pump, which can be bypassed at high pressures such that a roughening pump can pump directly on the lines. Capacitance baratrons with ranges up to 10 mbar, 1000 mbar, and 30 bar are mounted close to the line to the high pressure cell providing an accurate reading in a wide pressure range.
The available chemicals are 99.93 % CH_3OH, deionized H_2O, N48 purity CO_2, N55 purity O_2, and N60 H_2, CO, Ar, and He. Several cleaning procedures are applied to obtain higher purity before use. CO is led over an active carbon filter and a cooling trap immerged in liquid N_2 for removal of Ni-carbonyl, H_2 is passed over a reduced Cu catalyst cooled with liquid N_2, and CO_2 is purified further by several freeze-pump-thaw cycles using liquid nitrogen, which remove residual O_2. CH_3OH and H_2O are also cleaned using freeze-pump-thaw cycles.

[1] 95% W, 5% Re positive leg and 74% W, 26% Re negative leg. Temperature range 0 - 2320 ^{o}C.

[2] Chromel (90% Ni, 10% Cr) positive leg and alumel (95% Ni, 2% Mn, 2% Al, 1% Si) magnetic negative leg. Temperature range -200 to 1250 ^{o}C.

Chapter 3

UHV experimental methods

The surface science techniques available on the ultra-high vacuum chamber include low electron energy diffraction (LEED), X-ray photon spectroscopy (XPS), ion scattering spectroscopy (ISS), electron energy loss spectroscopy (EELS), and temperature programmed desorption (TPD). Moreover, the high pressure cell is equipped with a polarization modulation infrared reflection absorption spectroscopy (PM-IRRAS) setup which will be the subject of chapter 4. Summaries of each technique are given in the following sections. More extensive reviews can be found in [13], [58], and [59].

3.1 Electron energy loss spectroscopy

EELS, which is a method for studying the vibrations of molecules adsorbed on the sample surface, was pioneered by Propst and Piper in the 60's [60]. The method involves the bombardment of a sample with a monoenergetic beam of electrons. The signal is optimized without a sample in straight through mode where the monochromator and the analyzer are set in a 180° arrangement. When an adequate signal has been obtained, the angle is changed to 90° and the signal is again optimized in specular mode, where the electron beam is reflected of the surface. The setup is shown in figure 3.1.
The spectrum is obtained by scanning the kinetic energies of the electrons arriving at the analyzer. Most of the electrons that are reflected on the sample surface do not interact with the adsorbates and will be scattered elastically. The ones that do interact, experience discrete energy losses due to three scattering mechanisms. The one that gives rise to the most intense peaks in the spectrum, is dipole scattering, where energy is transferred from the electron to a vibrational mode of the adsorbate due to a long range interaction with the dynamic dipole. Similar to the selection rules for infrared spectroscopy, which are presented later, only the vibrations that lead to a dipole change normal to the surface is seen.
The second mechanism is impact scattering which is a short range interaction, where the electrons are scattered on the atomic core potential. This means that interaction with all vibrational modes are allowed, but the intensity of the losses is rather low.
A third mechanism called negative ion resonance scattering which depicts the situation

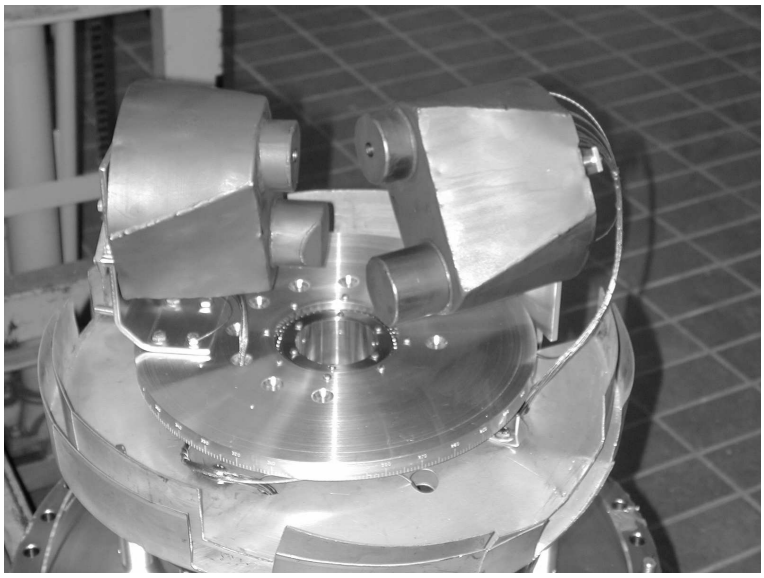

Figure 3.1: EELS setup. The monochromator is situated to the right and the analyzer to the left. The latter is mounted on a turn table.

where an incident electron for a brief moment is trapped in an empty, high lying orbital in the adsorbate also leads to losses. This mechanism is however rarely observed. The loss mechanisms and the theory have been reviewed by Thiry et al. [61].

The EELS spectrum consists of a large peak at the primary energy from the elastically scattered electrons that have not undergone losses. In specular mode the losses from dipole scattering will dominate, but if the setup is moved off-specular the much weaker losses due to impact scattering can be observed. EELS provides complementary information to infrared spectroscopy as it is not restricted to detection of the infrared active vibrations. The resolution of the setup is found as the FWHM (full width at half maximum) of the elastic peak. Newer equipment can typically reach a resolution of 20-30 cm^{-1} (about 3-4 meV), whereas the present setup could only be optimized to about 16 meV.
UHV conditions are needed together with magnetic shielding of the setup as low energy electrons are utilized. Furthermore, it is required that the sample is flat and conducting. Although EELS has a fairly low resolution compared to infrared spectroscopy, the method is highly sensitive and can in principle detect all vibrational modes. An extensive review of the method has been done by Ibach [62].

3.2 X-ray photoelectron spectroscopy

The principle behind XPS[1] is the absorption of a photon by an atom, leading to the emission of a core electron. The kinetic energy obtained by the emitted electron is then

[1]Also abbreviated ESCA - Electron Spectroscopy for Chemical Analysis.

given as

$$E_{kin} = hv - E_B - \varphi_{sample} \tag{3.1}$$

where hv is the energy of the photon, E_B is the binding energy of the electron referred to the Fermi level, and φ_{sample} is the work function of the sample. As the radiation employed is monochromatic, the energy distribution of the electrons will display fairly discrete peaks corresponding to the specific energy levels. This allows for the identification of elements, since each give rise to characteristic peaks in the XPS spectrum. The peak intensities are in turn related to the concentration of the element, and it is therefore also possible to determine the relative quantity at the sample surface. Furthermore, the measured binding energy of an element may display small shifts due to the chemical state of the atom. Reference data is available in [63] or the NIST XPS database [64].

Figure 3.2: The X-ray gun. Lower left inset shows the Mg/Al anode, and upper right inset shows the end cap on the anode housing. An Al-foil window is fitted.

Several sources of radiation may be used, each having different energies and distributions of the photons. Two that are commonly employed are aluminum and magnesium, which give rise to the primary radiation lines Mg Kα centered at $hv = 1253.6$ eV, and Al Kα radiation centered at $hv = 1486.6$ eV. The photoelectrons emitted from the sample thus have a kinetic energy in a range from 0 eV to the energy line characteristic of the chosen anode. In this energy region the electrons have a short inelastic mean free path (IMFP), which ensures the surface sensitivity of the method.
Drawbacks of XPS are that it is not sensitive to hydrogen or helium and generally must be carried out under UHV. However, recent advances have made it possible to employ XPS at pressures up to 1 mbar [6].

3.3 Ion scattering spectroscopy

In ISS, mono-energetic noble gas ions, typically He^+, with a primary energy E_0 of 1-2 keV are bombarded onto a sample, where they are elastically scattered by the surface atoms. The energy of the backscattered ions with mass M_i is characteristic of the mass of the target atoms, M_s, due to the conservation of energy, eq. 3.2, and momentum, eq. 3.3.

$$\frac{1}{2}M_i v_0^2 = \frac{1}{2}M_i v_1^2 + \frac{1}{2}M_s v_s^2 \tag{3.2}$$

$$M_i \vec{v_0} = M_i \vec{v_1} + M_s \vec{v_s} \tag{3.3}$$

v_0 and v_1 are the initial and final velocities of the probe ion, and v_s is the velocity of the target atom. A relation between the energy of the probe ion before and after scattering, E_0 and E_1, can then be found when the angle between the analyzer and the ion gun, θ, is known. For $M_s > M_i$ the relation takes the form

$$\frac{E_1}{E_0} = \Big[\frac{\sqrt{M_s^2 - M_i^2 \sin^2\theta} + M_i \cos\theta}{M_s + M_i}\Big]^2 \tag{3.4}$$

This allows for the determination of the mass of the target atom, M_s.

The ISS method is very surface sensitive as there is a high neutralization probability for the low energy noble gas ions. 99% of the ions which hit the surface will be neutralized. Furthermore, the method has a large scattering cross section.
The sputtering damage to the sample surface can be kept low by using light ions and small gas doses, but it is then difficult to distinguish between elements of similar mass. This can be counteracted with heavier probe ions like Ne^+ or Ar^+, which will however increase surface damage. Moreover, it is not possible to detect elements which are lighter than the probe ions used.

3.4 Low energy electron diffraction

LEED is employed to study the structure of a sample surface and ordered adsorbate layers by examining diffraction patterns of electrons reflected on the sample. A monochromatic beam of low energy electrons, typically $E_p < 200$ eV, is generated with an electron gun and directed toward the sample. A retarding field analyzer (RFA), which consists of several concentric hemispherical grids, is placed in front. The inner grid is held at ground and the middle at a negative potential just below E_p which ensures that only the elastically scattered electrons will contribute to the diffraction pattern. Electrons with lower energy are reflected back to the grounded grid. Between the last grid and the fluorescent screen, where the diffraction pattern of the backscattered electrons can be observed, there is a 2-5 keV difference to accelerate the electrons.

The wave length of the electrons is given by the deBroglie relation, eq. 3.5,

$$\lambda = \frac{h}{p} \tag{3.5}$$

where $p = \sqrt{2mE_p}$ is the electron momentum. From 3.5 it can be found that the range of wavelengths for electrons with a kinetic energy of 20-200 eV is comparable with atomic spacings, which is necessary for diffraction effects to take place. Furthermore, the inelastic mean free path of an electron in this energy range is low, ensuring high surface sensitivity. When the Bragg condition, eq. 3.6, is satisfied, that is, the difference in the path between the waves of the scattered electrons is equal to an integral number of wave lengths, n, constructive interference may be achieved.

$$n \cdot \lambda = d \cdot \sin(\theta) \tag{3.6}$$

d is the distance between the atoms, and θ is the angle between the scattered electron and the surface normal.

The diffracted electrons will lead to a reciprocal pattern on the fluorescent screen. From this, one can find the size and structure of the unit cell. The real space vectors, $\vec{a}_1$ and $\vec{a}_2$, and the corresponding reciprocal space vectors, $\vec{a}_1^*$ and $\vec{a}_2^*$, are related such that [65],

$$\vec{a}_1 \cdot \vec{a}_2^* = \vec{a}_1^* \cdot \vec{a}_2 = 0 \tag{3.7}$$

$$\vec{a}_1 \cdot \vec{a}_1^* = \vec{a}_2 \cdot \vec{a}_2^* = 1 \tag{3.8}$$

which in effect means that $\vec{a}_1 \perp \vec{a}_2^*$ and $\vec{a}_2 \perp \vec{a}_1^*$ and that $|\vec{a}_n| = 1/(|\vec{a}_n^*|\cos(\varphi))$, where φ is the angle between the two vectors.
When an adsorbate layer is present on the substrate, another reciprocal lattice is obtained. The resulting LEED pattern is however not just a superposition of both reciprocal lattices, but also displays all possible combinations between them. The interpretation of the patterns is therefore not always trivial.

3.5 Temperature programmed desorption

This very useful and simple method is used for analysis of the adsorption, decomposition, and reaction processes of adsorbates. The sample is placed in front of a quadrupole mass spectrometer and is then heated such that the temperature increases linearly with time, typically with a ramp of 1 - 5 K/sec, see equation 3.9, where T_0 is the starting point, and β is the heating rate. The intensity variation of preselected mass fragments are then recorded as a function of time and later correlated to the sample temperature.

$$T(t) = T_0 + \beta \cdot t \tag{3.9}$$

The temperature of maximum desorption, the shape of the desorption peak, and the heating rate can be analyzed to provide information of the binding energy and the desorption kinetics. Moreover, the peak area is proportional to the surface coverage.

If an infinite pumping capacity is assumed, it is possible to neglect readsorption. In this case the desorption rate, r_{des}, is given as

$$r_{des} = \frac{-d\theta_X}{dt} = v \cdot \theta_X^n \cdot \exp(\frac{-E_{des}(\theta_X)}{R \cdot T}) \tag{3.10}$$

where θ_X denotes the coverage of adsorbate X.

If it is furthermore assumed that the preexponential factor, v, and the desorption energy, E_{des}, are independent of the coverage, a relation can be found for the desorption rate. Eq. 3.11 describes the first order, $n = 1$, situation:

$$E_{des} = k_B T_{max}^2 \ln\left(\frac{k_B T_{max}^2 v}{E_{des}\beta}\right) \tag{3.11}$$

where T_{max} is the temperature at which r_{des} has its maximum value. Generally, the interpretation and treatment of the TPD data is not trivial. v and E_{des} are usually very dependent of the coverage, and it is difficult to obtain a good estimate of the preexponential factor v. In a situation where the transition state of a desorbing molecule is similar to the chemisorbed state, a value of 10^{13} can be assumed [13].

Chapter 4

Polarization modulation spectroscopy

Polarization modulation infrared reflection absorption spectroscopy, abbreviated PM-IRRAS[1], is a Fourier transform infrared (FTIR) spectroscopy method which utilizes different polarization states of the radiation to distinguish between the absorption by adsorbates on a sample surface and absorption by the gas phase [66, 67]. P-polarized radiation orthogonal to the surface can due to an enhancement of the electric field upon reflection be absorbed by vibrational excitation of surface species whereas the parallel s-polarized radiation cannot [68, 69]. The method is highly surface sensitive and can be used under non-UHV conditions and at elevated temperatures.
In the following sections the electromagnetic theory behind the use of different polarizations is presented, and the experimental setup is described. The last section is dedicated to the theoretical description of the PM-IRRAS signal and the computational treatment.

4.1 Electromagnetic radiation theory

Infrared radiation covers the range of the electromagnetic spectrum between approximately 1 and 1000 μm, where the lower limit is bounded by visible radiation, and the upper limit by microwave radiation. The infrared range is typically split up into three subparts, which are defined as near, mid and far infrared, see table 4.1. In the type of spectroscopy applied here, part of the middle range (1000-4000 cm^{-1})[2], where molecular vibrations are found, is used.

[1] Many abbreviations such as PM-IRAS, PM-RAIRS, PEM-RAIRS, or PM-FTIR also exist.

[2] In infrared spectroscopy, the vibrations are usually described by the wavenumber $\tilde{v} = 1/\lambda$ given in reciprocal centimeters (cm^{-1}). This gives the relation $c = v \cdot \lambda = v/\tilde{v}$, where c is the speed of light and v is the frequency in Hz. $\tilde{v}$ is proportional to energy and is related by 8.0655 cm^{-1} = 1 meV.

Table 4.1: Categorization of infrared radiation, [59].

Region Unit	Wavelength [μm]	Wavenumber [cm^{-1}]	Energy [meV]	Detects
Near	1 - 2.5	10000 - 4000	1240 - 496	Overtones
Middle	2.5 - 50	4000 - 200	496 - 25	Molecular vibrations
Far	50 - 1000	200 - 10	25 - 1.2	Lattice vibrations

Electromagnetic radiation consists of an electric and a magnetic field oscillating in phase perpendicular to each other. The vibrational excitation of a molecule is due to the interaction of the electric field with a change in the dipole moment of the molecule. The dipole moment, μ, is given in equation 4.1, where the first term μ_0 is the contribution from the permanent dipole, and the second term describes the change in dipole moment caused by a vibration given as the deviation from the equilibrium distance r_e.

$$\mu = \mu_0 + (r - r_e)\left(\frac{\delta\mu}{\delta r}\right)_0 + ... \tag{4.1}$$

The electric field of the planar harmonic electromagnetic wave incident to the sample surface is displayed in eq. 4.2.

$$\vec{E_i} = \vec{E}_{0i}\cos(\vec{k}\cdot\vec{x} + \omega t) \tag{4.2}$$

The amplitude is given by $|\vec{E}_{0i}|$, and the phase by the expression $\vec{k}\cdot\vec{x} + \omega t$, where $\vec{k}$ is the wave vector, a unit vector in the direction of propagation, $\vec{x}$ is a position vector, ω is the angular frequency, and t is the time.

When the wave interacts with a crystal surface the law of reflection states that the angle between the incoming beam and the surface normal, θ_i, is equal to the angle between the reflected beam and the surface normal, θ_r. Furthermore, the surface normal, the incoming, and the reflected beams define a plane, which a called the plane of incidence, see figure 4.1. It is convenient to consider the incident radiation as the superposition of two plane-polarized beams; p-polarized with the electric field parallel to the plane of incidence and s-polarized with its electric field perpendicular to the plane of incidence.

The reflected wave is described by:

$$\vec{E_r} = \vec{E}_{0r}\cos(\vec{k}\cdot\vec{x} + \omega t + \varphi) \tag{4.3}$$

The resulting phase change, φ, due to the reflection depends both on the incidence angle and the state of polarization of the radiation. The amplitude and phase relationships between reflected and incident light may be found using the Fresnell equations, see eq. 4.4 and 4.5. They yield the reflection coefficients, r_s and r_p, of the s- and p-polarized components describing the ratio between the amplitude of the reflected and incident light, $r = |\vec{E}_{0r}|/|\vec{E}_{0i}|$.

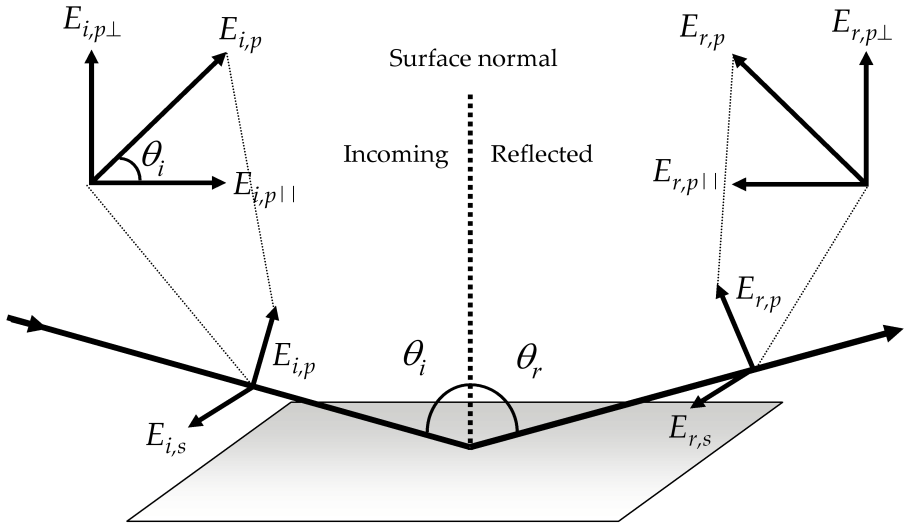

Figure 4.1: Sketch of the electric field for incident and reflected p and s-polarized radiation. Inserts depict the parallel and orthogonal components of the p-polarized part of the radiation.

$$r_p = \frac{n_t \cos(\theta_i) - n_i \cos(\theta_t)}{n_t \cos(\theta_i) + n_i \cos(\theta_t)} \tag{4.4}$$

$$r_s = \frac{n_i \cos(\theta_i) - n_t \cos(\theta_t)}{n_i \cos(\theta_i) + n_t \cos(\theta_t)} \tag{4.5}$$

θ_t denotes the angle of the transmitted beam in the solid to the surface normal. n_i and n_t are the refractive indices of the media of the incident beam and the transmitted beam. For a nonabsorbing media the refractive index is defined as the ratio between the speed of light in vacuum and in the medium, $n = c/v$. For an absorbing media n is complex and given as $n = n_0 + \kappa i = c/v + \kappa i$, where κ is the extinction coefficient, which indicates the amount of absorption loss when the electromagnetic wave propagates through the material. For the present system, $n_i = 1$ as the incident beam travels in vacuum, and $n_t = 4.70 - 19.40i$, which is found for Pt, when the beam has an energy of 0.25 eV [70]. The angle between the transmitted wave and the surface normal, θ_t, can be found with Snells law, eq. 4.6.

$$\frac{n_i}{n_t} = \frac{\cos(\theta_t)}{\cos(\theta_i)} \tag{4.6}$$

It is noted that when there is total external reflection, as found for a metal surface, θ_t is not a real angle.

The reflectance, $R_i = |r_i|^2$, which describes the ratio between the reflected power and the incident power, as well as the phase change, $\varphi_i = \arg(r_i) = \arctan(\mathrm{Im}(r_i)/\mathrm{Re}(r_i))$, are shown in figure 4.2 a and b. For s-polarization there is a phase change of approximately

$\varphi = -180°$ for all incidence angles. This results in destructive interference at the surface and hence a very small field, which furthermore makes interactions with dipoles parallel to the surface weak. In contrast, the reflectance and phase shift for the p-polarized radiation vary strongly with the incidence angle. At $\theta_i < 70°$ small shifts are obtained, but above that value the phase shifts rapidly leading to $\varphi = -180°$ at $\theta_i = 90°$ yielding a cancellation of the field at the surface. However, close to $\theta_i = 90°$ the incident and reflected field vectors add constructively resulting in a standing wave with a large component normal to the surface.

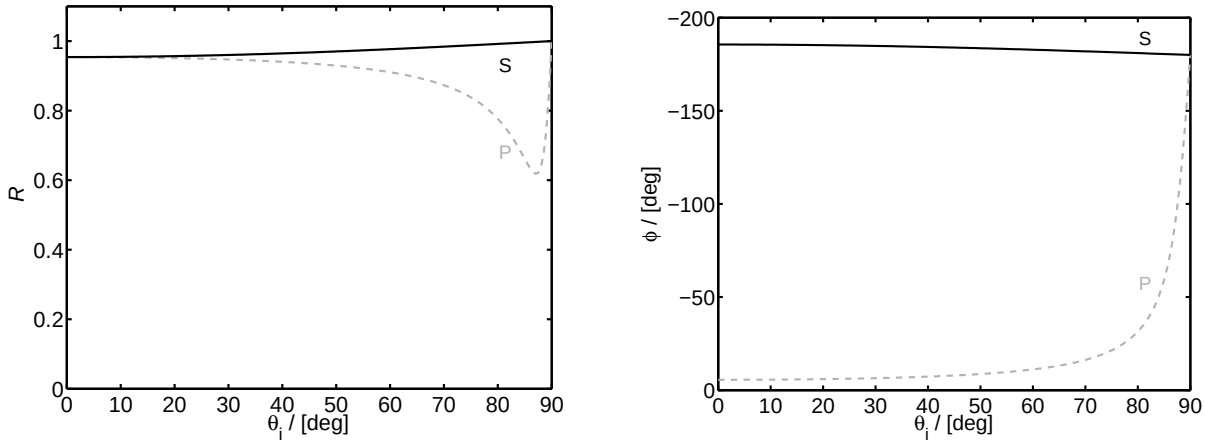

a) b)

Figure 4.2: a) Reflectance of incident s- and p-polarized radiation as a function of the incidence angle, and b) Phase shift of incident s- and p-polarized radiation as a function of the incidence angle. $n_t = 4.70 - 19.40i$ was used. Phase graphs reproduces results from [71].

By adding the incident and reflected waves and making use of the relation $|\vec{E}_{0r}| = r \cdot |\vec{E}_{0i}|$, it can be shown that the resulting amplitude, $|\vec{E}_0|$, at the surface may be given by eq. 4.7:

$$|\vec{E}_0| = \sqrt{|\vec{E}_{0,i}|^2 + (|\vec{E}_{0,i}||r|)^2 + 2|\vec{E}_{0,i}|^2|r|cos(\varphi)} \tag{4.7}$$

which holds true for both the s- and p-polarized radiation. Furthermore, the parallel and perpendicular component of the p-polarized radiation can be found by the relationships $\vec{E}_{0,i,p\perp} = \vec{E}_{0,i,p}\sin(\theta_i)$ and $\vec{E}_{0,i,p||} = \vec{E}_{0,i,p}\cos(\theta_i)$, see figure 4.1. It is noted that $E_{i,p||}$ and $E_{r,p||}$ are opposed, which corresponds to an introduction of an additional 180° phase shift into the equation. The normalized electric field at the reflecting surface for s-polarized radiation and the two components of the p-polarized radiation as a function of the incidence angle, are shown in figure 4.3a. It is seen that close to $\theta_i = 90°$ the constructive interference results in a large amplitude of the perpendicular p-polarized radiation, whereas the amplitudes of the parallel part as well as the s-polarized radiation are negligible.

When the metal is covered by adsorbates, see figure 4.4, the situation is somewhat different. The absorption may be estimated by applying that the absorption will be proportional to $|\vec{E}_0|^2$ and the distance traveled through the adsorbate layer [72]. As this distance is proportional to $1/\cos(\theta_i)$ the maximum absorption may be found at the maximum value of $|\vec{E}_0|^2/\cos(\theta_i)$. This relationship is shown as a function of incidence angle in figure 4.3b. It is seen that s-polarized radiation and the parallel component of the p-polarized radiation generally display very small amplitudes at all θ_i, whereas the perpendicular part exhibits larger values with a maximum just below 90°. This also has implications for the orientation of the dipoles of the molecules, as only dipoles with a component that is perpendicular to the surface will be able to absorb the radiation. The influence of the overlayer will not be analyzed further here, but the reader is referred to [69, 73, 74].

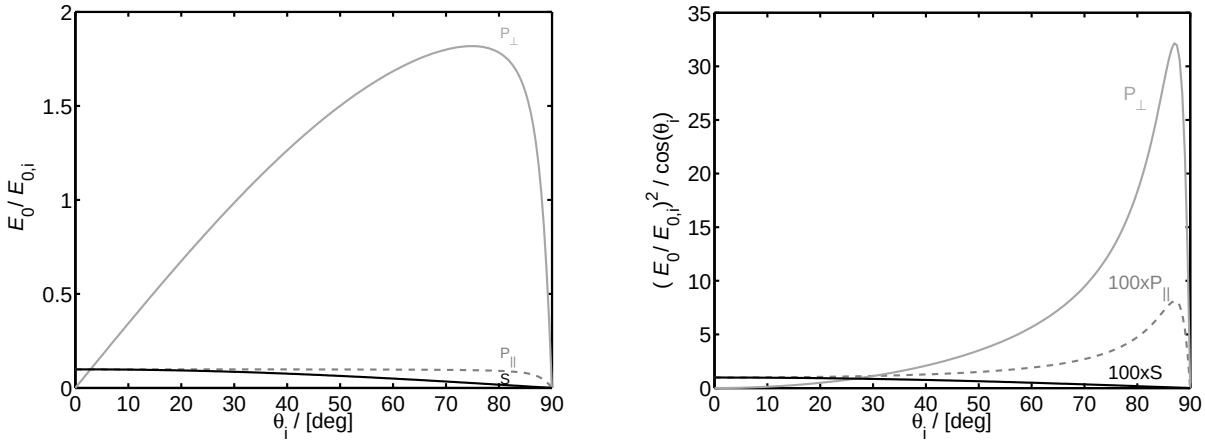

a) b)

Figure 4.3: a) Normalized electric fields at the reflecting surface for s-polarized radiation and the two components of the p-polarized radiation as a function of the incidence angle. b) Total absorption intensity for vibrational excitation. $n_t = 4.70 - 19.40i$ was used.

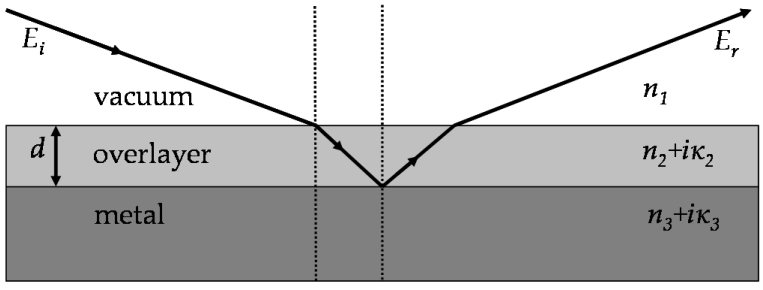

Figure 4.4: Three-layer model depicting the light impinging on a metal surface covered by a layer of adsorbates.

The presented behavior of the different radiation components must be taken into account when designing the experimental setup. Since constructive interference for p-polarized

radiation, and thus the highest absorption, is found just below an incidence angle of 90°, an optimal geometry will employ a grazing incidence of the radiation onto the sample surface.

4.2 PM-IRRAS setup

The PM-IRRAS setup is shown in figure 4.5. The spectrometer containing the infrared source and interferometer is a Nexus module supplied by Thermo Nicolet, who has also delivered the MCT (HgCdTe) detector. The PEM-90 photoelastic modulator has been supplied by Hinds Instruments, and the demodulator by GWC Technologies. ZnSe windows have been fitted onto the high pressure cell in order to allow transmission of the beam.

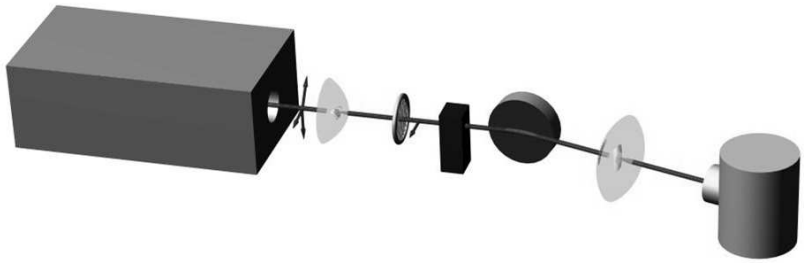

Figure 4.5: The PM-IRRAS setup. From left to right: IR-source and interferometer, lens, polarizer, modulator, crystal, lens, and MCT-detector. Picture courtesy of Ph.D. Michael Andersen, [75].

The interferometer splits the beam from the IR source with a KBr beam splitter. One half is reflected of a fixed mirror, and the other half of a mirror moving with a constant velocity. The returning beams are then recombined at the beam splitter and a interferogram signal which is the sum of the constructive and destructive interferences over time is produced. An internal calibration laser is used to keep track of the position of the moving mirror. The signal is then focused with a planar convex lens onto a polarizer which converts the unpolarized beam into one with a single linear polarization perpendicular to the sample surface. Next, the photoelastic modulator (PEM), see figure 4.6a, modifies the signal into different states of the light. This is done by applying periodically stress and strain to a ZnSe crystal slab using a piezoelectric element. The photoelastic modulator and demodulator use a modulation frequency in the 100 kHz range. The optimum in signal depends on the amplitude of the stress applied, as there is only a full 180° or π phase shift at one specific frequency. Modulation efficiency is lowered at all other frequencies, which results in a humped background of the signal. This optimum can be chosen on the equipment manually and must be tuned to correspond to the frequency from the intermediate under investigation to obtain the best signal to noise ratio.

The beam is then reflected on the sample surface at an incidence angle between the beam and the surface normal of 82°, according to the aforementioned theory. The interferogram signal is then focused with a biconvex lens onto the MCT detector, see figure 4.6b, recorded, and Fourier transformed into its component curves. The MCT detector has its optimal spectral response from 1000 to about 2000 cm^{-1} with coverage up to 4000 cm^{-1} It must be cooled with liquid nitrogen and is then able to operate at low temperature for over 14 hours before a refill is needed [76].
The lenses, polarizer, modulator, and detector outside the Nexus module are all exposed to air, and absorption bands from water and CO_2 are present in the unmodulated spectra, but not in the PM-IRRAS demodulated spectra. A dehumidifier and filter is fitted to the system to minimize these absorption bands and to protect the beam splitter in the interferometer.

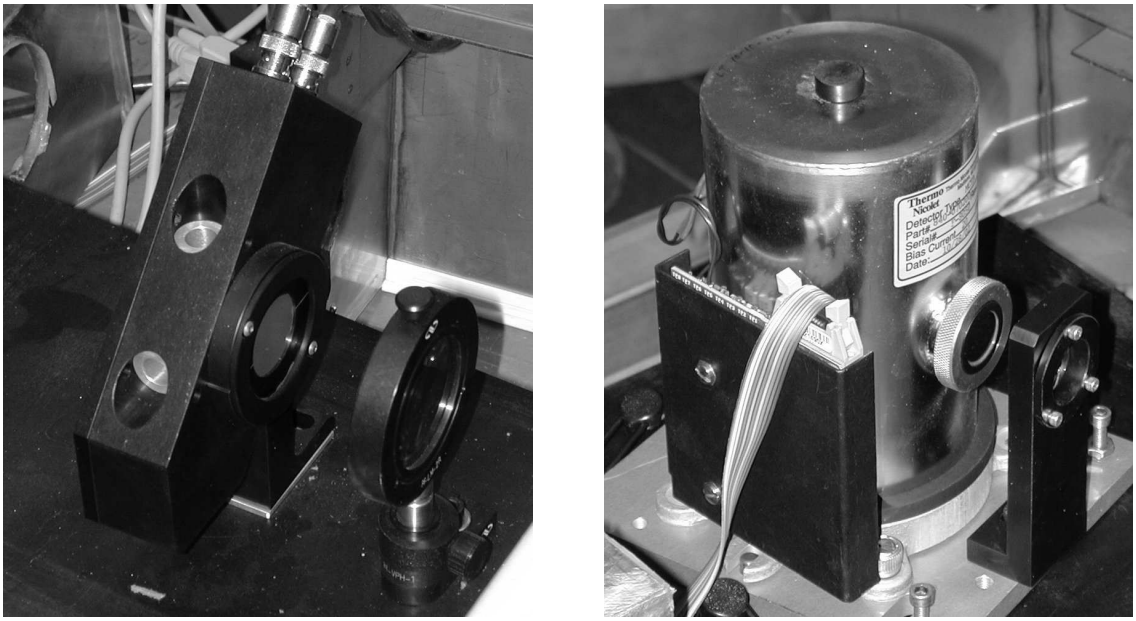

a) b)

Figure 4.6: a) Polarizer and photoelastic modulator optical head. b) MCT (HgCdTe) IR detector.

4.3 Theoretical treatment of the PM-IRRAS signal

The p-polarized radiation interacts with both the adsorbates and the gas phase, whereas s-polarized radiation only interacts with the gas phase. The signal from the surface species are thus the difference between them. To remove contributions from the gas phase, it is necessary to normalize with the sum of s and p. Ideally the differential reflectance spectrum, eq. 4.8, would be the ratio of the difference spectrum $(I_p - I_s)$ and the sum spectrum $(I_p + I_s)$, where I_p and I_s are the intensities of the p- and s-polarized radiation,

but as it shall be seen in the following, additional terms will be introduced due to the nature of the experimental setup.

$$\frac{\Delta R}{R} = \frac{R_p - R_s}{R_p + R_s} = \frac{I_p - I_s}{I_p + I_s} \tag{4.8}$$

As mentioned, the polarizer only allows passage of radiation that is p-polarized with respect to the sample surface. The PEM setup then modulates the polarization by straining and compressing the ZnSe crystal in the optical head, which leads to changes in the birefringence. The PEM head has a strain axis of $\pi/4$ or 45° relative to the incoming p-polarized radiation from the polarizer, see figure 4.7. For a specific (chosen) wave length the maximum retardation is π along this axis, thus yielding a linear s-polarization state. The PEM has a nominal oscillation frequency[3] $\omega_n = 50$ kHz and is run in half-wave retardation, see figures 4.7 and 4.8.

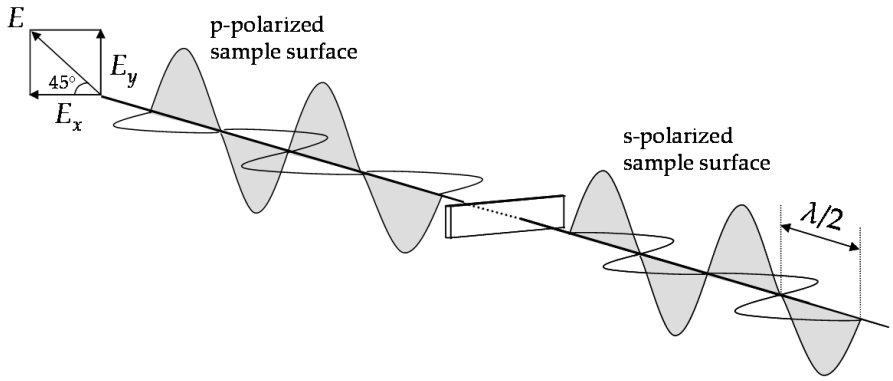

Figure 4.7: Half wave retardation for one specific frequency. The incoming p-polarized radiation is converted to the s-polarized state.

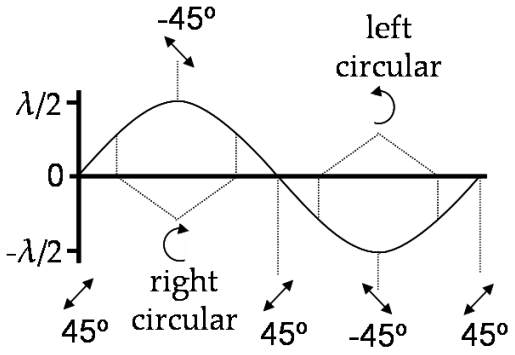

Figure 4.8: Retardation as a function of time. A full modulator cycle is shown [77].

[3]It is noted that $2\omega_n$ is the modulation frequency.

The intensity after interaction with the PEM is given as eq. 4.9 [78, 79].

$$I(t) = \frac{1}{2}[I_p + I_s + (I_p - I_s)\cos(\varphi_0 \cos(\omega_n t))] \tag{4.9}$$

The relative phase shift is $\varphi(t) = \varphi_0 \cos(\omega_n t)$, where φ_0 is the maximum phase shift introduced by the PEM. φ_0 is proportional to the applied modulation voltage, V_m, and the frequency, v. This implies that one cannot achieve a perfect s-polarization state as all frequencies are present simultaneous in the signal. From equation 4.9 the intensity $I(t)$ at 0°, 90°, 180°, and 270° is found as, [78],

$$I(t) = I_p \qquad \omega_n t = \frac{1}{2}\pi, \frac{3}{2}\pi \tag{4.10}$$

$$I(t) = \text{''}I_s\text{''} = I_s + (I_p - I_s) \cdot \frac{1 + \cos(\varphi_0)}{2} \qquad \omega_n t = 0, \pi \tag{4.11}$$

This leads to the spectrum

$$\frac{I_{diff}(v)}{I_{sum}(v)} = \frac{\frac{1}{2}(I_p - I_s)(1 - \cos(\varphi_0))}{(I_p + I_s) + \frac{1}{2}(I_p - I_s)(1 + \cos(\varphi_0))} \tag{4.12}$$

$$\approx \frac{1 - \cos(\varphi_0)}{2}\left[\frac{I_p - I_s}{I_p + I_s}\right] \tag{4.13}$$

Here it has been assumed that $(I_p + I_s) >> (I_p - I_s)$ which is a good approximation in a satisfactory range around $\varphi_0 = \pi$ on most metals. It is seen that the true reflectance spectrum is multiplied with a function $(1 - \cos(\varphi_0))/2$. As φ_0 varies with frequency a theoretical description of the background variation is thus obtained.

Several polarization artifacts arising between the PEM and the detector must according to Buffeteau et al. [67] also be taken into account. These effects are described by the overall responses C_p and C_s, of the setup for p and s linear polarizations, and are introduced in the equation for the difference signal, eq. 4.14, as the ratio $\gamma = C_p/C_s$.

$$\frac{I_{diff}(v)}{I_{sum}(v)} \approx \frac{1 - \cos(\varphi_0)}{2}\left[\frac{\gamma I_p - I_s}{\gamma I_p + I_s}\right] \tag{4.14}$$

As there is no additional polarization-sensitive optics between the sample and the detector for the present setup, no additional terms due to the instrumentation are introduced, and a γ close to 1 is expected.

Two methods for obtaining the differential interferogram from the detector signal are generally in use. Lock-in amplifiers [79, 67] have some inherent problems, as their high time constants limit the mirror speed of the interferometer, and hence the collection of the interferogram to about 5-10 kHz. Another method, which is the one that is implemented on the present setup, was developed by Corn and co-workers [78, 80], who used real-time

sampling electronics achieving sampling rates of 50-100 kHz. That is, the acquisition is limited by the speed of the PEM, and not the amplifier [81, 82]. The electronics produce the sum and difference interferograms, which are then Fourier transformed from the time domain to the frequency domain to yield the two spectra.

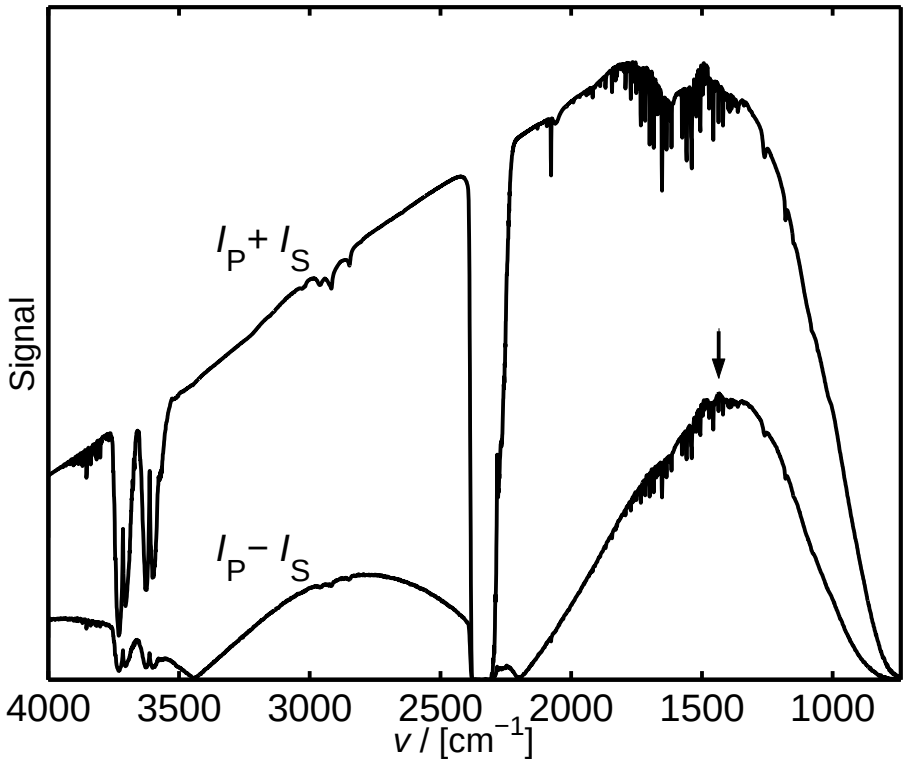

Figure 4.9: I_{sum} and I_{diff} versus wave number. φ_0 was set to π at 1350 cm^{-1}. The sum spectrum shows absorption bands from H_2O and CO_2. A peak at 1435 cm^{-1} from carbonate (CO_3) is hard to distinguish.

Examples of the separate sum and difference signals are given in figure 4.9. Because of the air present outside the high pressure cell, the sum spectrum, $(I_p + I_s)$, always contains clear absorption bands due to H_2O from 1300 to 2000 cm^{-1} and above 3400cm $^{-1}$, as well as CO_2 bands in the ranges 2200-2400 cm^{-1} and 3500-3750 cm^{-1}. The latter are however dominant in this figure, as the high pressure cell was filled with CO_2, when the spectrum was acquired.

The background for the sum spectrum follows the intensity distribution from the infrared source. This, together with the bands from atmospheric H_2O and CO_2, may be removed by obtaining a reference spectrum before the introduction of the gas into the high pressure cell. The gas spectrum is often given in terms of the absorbance, A

$$A = \log\left(\frac{1}{T}\right) = \log\left(\frac{I_{ref}}{I_{ads}}\right) \tag{4.15}$$

where I is the intensity at a specified wavelength λ which has interacted with the sample, and I_0 is the intensity of the incident radiation. The absorbance is as stated in the Beer-Lambert-Bouguer law proportional to the length that the radiation passed through in the gas and the concentration of the absorbing species. The transmittance $T = I/I_0$, however, varies exponentially.

The difference spectrum, $(I_p - I_s)$, which is also shown in figure 4.9 is seen to display the highest intensity around 1350 cm^{-1}, where the maximum phase shift, $\varphi_0 = \pi$, has been chosen. As was the case for the sum spectrum, bands from H_2O and CO_2 dominate making it difficult to identify a peak at 1435 cm^{-1} due to a vibration of carbonate (CO_3) adsorbed on the sample surface. By taking the ratio of the two signals, the differential reflectance spectrum, figure 4.10, is produced. Here the contributions from the gas phase are almost completely removed and the carbonate peak is distinct.

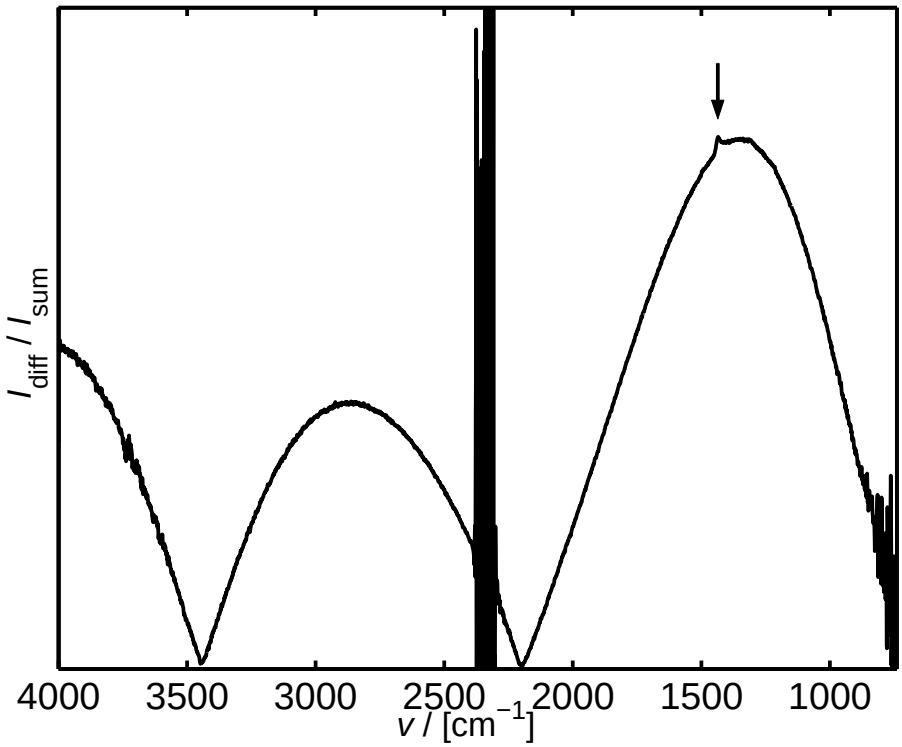

Figure 4.10: The differential reflectance spectrum. A peak at 1435 cm^{-1} from carbonate (CO_3) is distinct.

In figure 4.11 the background has been removed thus obtaining a flat baseline in a limited range. Aside from the distinct peak at 1435 cm^{-1} two peaks at 1310 cm^{-1} and 1215 cm^{-1} are now also recognizable.

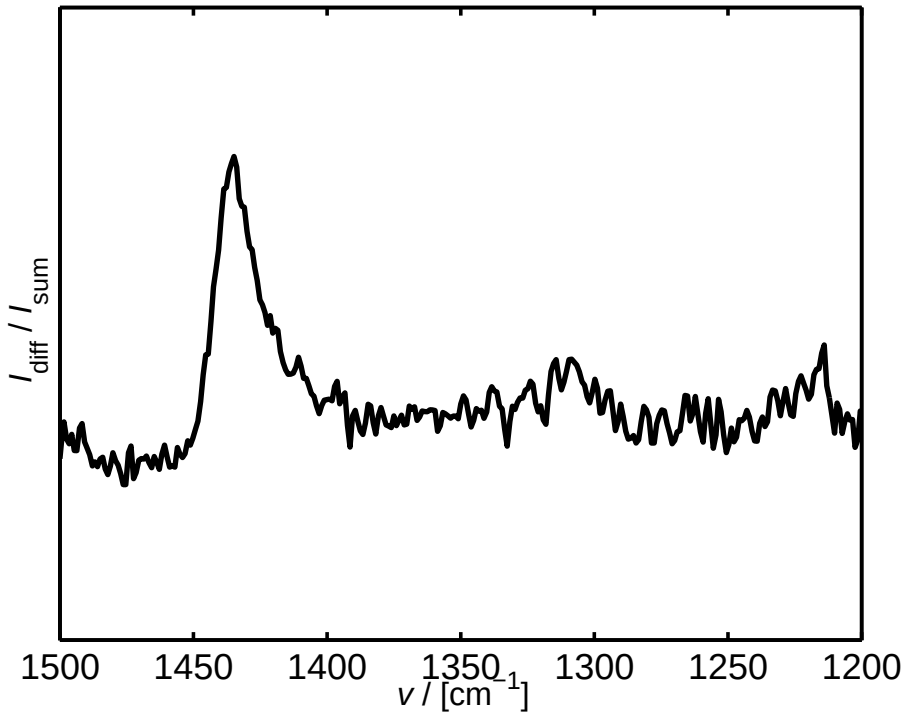

Figure 4.11: The differential reflectance spectrum with the background removed.

Chapter 5

Molecular vibration theory

Several effects may influence the vibrational modes when a molecule adsorbs on a metal surface, causing a deviation from the frequencies that are observed in the gas phase. These effects also have implications for the absorption of radiation as well as the lines shape of the absorption peaks. As knowledge of the behavior is necessary to interpret vibrational spectra and identify interactions between adsorbates, the theoretical descriptions of these mechanisms are summarized in the upcoming sections.

5.1 Molecular vibrations - basics

A molecule with n atoms will have a number of vibrational modes given by $3n-5$ for a linear configuration and $3n-6$ for a non-linear. This corresponds to three degrees of freedom for each atom minus translations (x, y, z) and rotations (r, θ, and ϕ in the non-linear case).
There are generally two categories of internal vibrations. Stretching describes changes in distance between atoms along the bond axis, and bending is a change in the angle between multiple bonds. The subtypes are depicted in figure 5.1.
The vibrational energy levels, E_n, of a diatomic molecule are given as eq. 5.1, when the harmonic oscillator approximation, eq. 5.2, is used to describe the potential, $V(r)$. It is only valid for small deviations of r from the equilibrium distance between the atoms, r_{eq}.

$$E_n = hv(n+\frac{1}{2}) \tag{5.1}$$

$$V(r) = \frac{1}{2}k(r-r_{eq})^2 \tag{5.2}$$

Here n is a positive integer that depicts the level number, h is Planck's constant, and v is the vibrational frequency. The force constant, k, depends on the strength of the nuclei repulsions, electron repulsions, and electron-nuclei attractions. Although k only describes the potential well curvature, it may still be used as an estimate of bond strength as the

curvature is usually correlated with the depth of the well [59].

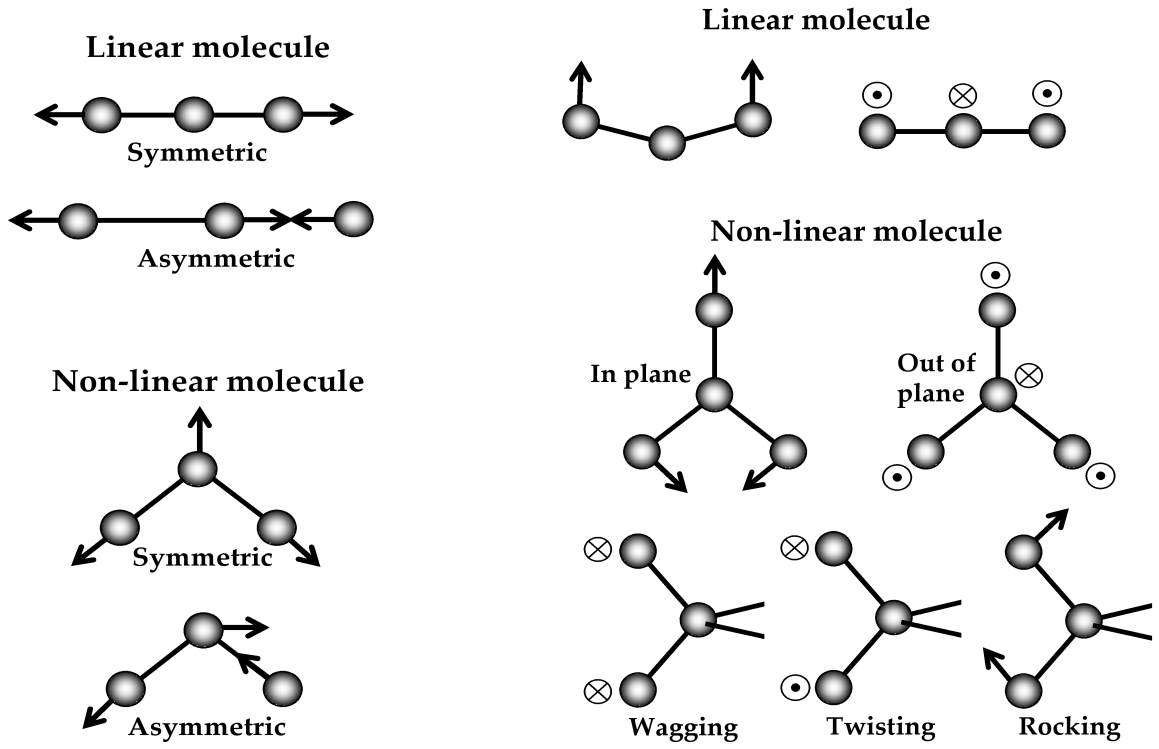

Figure 5.1: Fundamental vibrations for linear and non-linear molecules. a) Stretching modes, and b) bending modes.

The vibrational frequency of the molecule is given as:

$$v = \frac{1}{2\pi}\sqrt{\frac{k}{\mu}} \quad , \quad \mu = \frac{m_1 m_2}{m_1 + m_2} \tag{5.3}$$

where μ is the reduced mass of the two atoms, and m_i is the mass of the individual atoms. It is seen that an increase in bond strength and a decrease in the reduced mass causes an increase of the frequency.

5.2 The influence of adsorption on vibrations

When a molecule adsorbs on a rigid substrate, M, translations and rotations become hindered. The number of vibrational modes is then determined by the number of internal

modes plus the number of frustrated rotational and translational modes. Furthermore, the internal vibrations may be influenced through several mechanisms. According to the extensive review by Hoffmann [69] important effects include mechanical renormalization, dipole-dipole interaction, image dipole interaction, and chemical shift.

5.2.1 Mechanical renormalization

Mechanical renormalization describes the mechanical shift in internal frequency that arises when a molecule adsorbs on the surface. For a diatomic molecule Lucas and Mahan[1] found that the shift can be calculated as

$$\Delta v = v - v_0 = v_0 \cdot \frac{k_{M-m_2}}{k_{m_1-m_2}} \cdot \frac{\mu^2}{2 \cdot m_2^2} \tag{5.4}$$

Here v_0 is the internal vibration frequency of the molecule in the gas phase, and v is the frequency after taking the renormalization into account. $k_{m_1-m_2}$ and k_{M-m_2} are the force constants for the internal vibration, $m_1 - m_2$, and the stretch between the surface and the second atom, $M - m_2$.
A shift to higher frequencies for the internal vibration is obtained due to this effect, which has been predicted to be about 2.5 % for the CO molecule. This simple model neglects vibrations of the substrate. If taken into account, larger shifts are predicted, which mainly influence the $M - m_2$ bond. Mechanical renormalization cannot in itself account for the experimental observations, as a downward shift in frequency upon adsorption is generally found [69].

5.2.2 Chemical shift

The chemical shift effect arises due to chemisorption where there is charge transfer between the molecule and the metal surface. Eichens and Pliskin [83] observed the importance of this phenomenon for the adsorption of CO on different sites of supported transition metals, and the Blyholder backbonding model [84, 85] provided the first theoretical description. A donation from the molecules bonding orbital (5σ for CO) to the metal d-band and a back donation from the d-band to an antibonding orbital ($2\pi*$ for CO) weakens the internal bond and hence causes a lowering of the frequency. The size of the $2\pi*$ occupation due to back donation has been correlated to the frequency range for CO [69]. The size is dependent on the charge environment on the metal surface and is thus influenced by the coverage of adsorbates, and by the adsorption of electron donors such as hydrocarbons or acceptors such as alkali metals on the surface.

[1] As referenced in [69]

5.2.3 Image dipole interaction

Another effect that influences the internal bond as well as the absorption of different polarizations of infrared radiation is the image dipole interaction. A molecule with a dipole in the vicinity of a metal surface will induce an image dipole inside the metal, see figure 5.2. When the dipole is parallel to the surface the image dipole almost entirely cancels out the effective dipole, and as no strong parallel dipole field is found, s-polarized radiation is not absorbed. In contrast, a dipole orthogonal to the surface causes an enhancement of the dipole field and thus an enhanced absorption of p-polarized radiation. This phenomenon is called the surface selection rule.

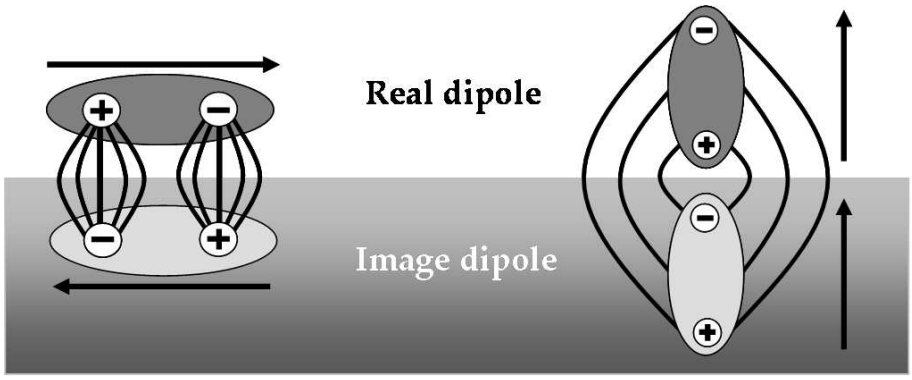

Figure 5.2: Imaging of dipoles in a metal

A downward shift in vibrational frequency is also induced due to the vibrational coupling between the dipole and the image, see equation 5.5, [86, 87, 69].

$$\left(\frac{v}{v_0}\right)^2 = 1 - \frac{\alpha_v/4d^3}{1-\alpha_e/4d^3} \tag{5.5}$$

where v_0 and v are the vibrational frequencies before and after taking the image dipole interaction into account. α_v is the vibrational and α_e the electronic polarizability[2] of the molecule. d is given as the distance between the image and the dipole. The model is found by assuming undamped vibrations and that α_e is constant in the range of frequencies that is of interest. It is difficult to obtain precise numbers for the shift caused by image dipole interaction, as the three parameters, α_v, α_e, and d, are quite hard to determine. For a CO molecule downward shifts of 1 to 2.5 % have been estimated.

[2]The polarizability is defined as the relative tendency of a charge distribution to be distorted.

5.2.4 Dipole-dipole interaction

As well as image dipoles interact with molecule dipoles, there is also an interaction between dipoles set up by several molecules. The introduced shift may be described as, [87, 88, 89]

$$\left(\frac{v}{v_0}\right)^2 = 1 + \frac{\theta\alpha_v U}{1 + \theta\alpha_e U} \tag{5.6}$$

U denotes the coupling matrix summed over all dipoles and image dipoles, θ is the coverage, v_0 is the original vibrational frequency of the molecule in absence of any interaction with other adsorbed molecules, and v is the frequency when including the dipole-dipole effect. It is evident from eq. 5.6 that the shift in frequency is always positive.

The dipole-dipole coupling also has implications on infrared spectroscopy. The intensity of the absorption bands generally depends on the amplitude of the electric field at the surface, the orientation of the dipole moment to the field, and the amount of adsorbed molecules. According to [88, 89] the strength of the infrared absorption at a specific frequency, v, may be estimated by

$$A(v) \approx nv\mathrm{Im}(\alpha_{eff}(v)) \tag{5.7}$$

where n is the number of molecules per unit area, and α_{eff} is the effective polarizability of the adlayer, which is described in terms of the electronic polarizability, and the vibrational polarizability by

$$\alpha_{eff} = \alpha_e + \frac{\alpha_v}{1 - (v/v_0)^2} \tag{5.8}$$

The absorption intensity for a surface with coverage θ up to a full monolayer may be estimated by equation 5.9, [88].

$$\int A(v)dv \approx \frac{\theta\alpha_v U}{(1 + \theta\alpha_e U)^2} \tag{5.9}$$

Eq. 5.9 shows how the integrated intensity depends on the dielectric screening due to the electronic polarizability, α_e, of the molecule. Pfnür et al. [90] observed this screening effect for CO adsorbed on Ru(0001). The intensity versus coverage behavior with a maximum obtained at $\theta_{CO} = 0.33$ was explained by an increasing vibrational coupling due to larger islands on the surface. This results in a depolarization of the molecule and hence a decrease in absorption intensity.

5.3 Peak shape and broadening

A number of effects govern the broadening of absorption bands, which are usually divided into two groups; inhomogeneous and homogeneous broadening [69].

Homogeneous broadening arises as a result of phonon coupling or charge transfer fluctuations leading to damping of the vibrational mode. Phonon coupling may lead to broadening for low frequency modes like the stretch between a metal and an adsorbate, e.g. a metal-oxygen stretch. However, for internal stretches with a high frequency like the one in CO, the effect is considered negligible. Periodic charge fluctuations are on the other hand considered to contribute to the broadening. This is for example seen for CO adsorbed on a metal surface where the antibonding $2\pi^*$ orbital is partially filled due to overlap with the metal d-band. The vibration causes a stretch of the CO bond which leads to a fluctuation of the filling degree of the orbital.

Inhomogeneous broadening results from variations in intermolecular interactions or slight differences in adsorption sites resulting in differences in the chemical shift. An ordered layer will give a sharp, symmetric peak, and deviations from this behavior may be illustrated by the variation of coverage, mobility of the adsorbates, and nature of the intermolecular forces.
At low coverage the situation is determined by the mobility and the intermolecular forces. With low surface mobility which is for example obtained at low temperature, a highly disordered layer will result in an asymmetric peak. If the intermolecular forces are repulsive (e.g. CO), an increase in mobility will maximize the intermolecular distances and hence a symmetrical shape is obtained. If the forces on the other hand are attractive (for example due to hydrogen bonding), a situation with adsorbate island formation occurs. Depending on the distribution between islands and single molecules a splitting of the band may result. If the islands are large the bands may also be asymmetric due to the altered surroundings for the molecules at the rims of the islands.
At high coverage the scenario is dominated by intermolecular repulsion. If a high diffusion barrier is present, different domains may be created leading to two distinct peaks in the spectrum. In the case of a low diffusion barrier, the variation of adsorption sites may result in peak broadening.

Chapter 6

Interaction of CO_2 and H_2 with Cu/Pt(111)

Microkinetic modeling[1] of the water-gas shift reaction activity trends covering several transition metals has suggested that the activity of copper-based catalysts can be improved by increasing the binding energy of both carbon monoxide and oxygen to the surface [56]. Ways to achieve a stronger binding include introduction of low coordination sites as well as stretching of the Cu lattice by growing a pseudomorphic layer on top of a host metal with a larger lattice constant. This will result in a narrowing of the d-band due to a larger nearest neighbor distance and hence a decrease in overlap between the electron orbitals of the Cu atoms. As the electron filling degree must be preserved, the d-band will shift up in energy[2]. This leads to stronger binding of the adsorbates and higher reactivity [91, 1]. As CO_2 is involved in WGS and known to be the main source of carbon in methanol synthesis [21, 22, 92], it is interesting to examine the interaction of it as well as the reaction with H_2 employing a well-defined model system that can emulate both stretching of the Cu lattice and roughness.

6.1 Properties of the copper / platinum (111) system

Although a given metal is estimated to be more reactive as a pseudomorphic layer on top of another metal, it is not necessarily possible to realize that configuration, as the stability depends on the mixing and segregation energy of the two metals. Generally, bulk or surface alloying as well as phase separation may occur, and phase diagrams must be used to check the behavior of a given bimetallic system. A large collection of diagrams for transition metals is found in [93].
A bimetallic system that possesses the required properties is copper deposited on platinum, as the lattice spacing for Cu(111) is 8% smaller than that of Pt(111), leading to a strained Cu overlayer. Cu/Pt(111) has been thoroughly investigated experimentally

[1] A description of the model and the results are given in chapter 7.
[2] This is only valid for the late transition metals. The center shifts down for filling degrees below 0.5.

[94, 95, 96, 97, 98, 99, 100, 101, 102, 103, 104, 105, 106] and theoretically [99, 91, 107, 108] during the last three decades.
Scanning tunneling microscopy (STM) and He atom scattering (HAS) have revealed that the growth of copper is pseudomorphic with nucleation at the step sites of the Pt surface [102]. Two-dimensional dendritic Cu islands are formed at room temperature and grow from the step edges coalescing into a defective pseudomorphic overlayer as coverage increases. The second layer commences growth before the first is complete and is rotationally commensurate to the Pt substrate with a lattice parameter closer to that of bulk Cu(111) [97].
Holst et al. [102, 103] furthermore examined the structure of Cu on Pt(111) at different deposition temperatures. No reconstruction was observed at 340 K, but a highly defective surface was grown. Higher deposition temperatures yielded smoother overlayers. At 450 K a reconstruction that was assigned to take place in the Pt substrate was observed.
A Cu/Pt near surface alloy has recently received attention as a possible catalyst for water-gas shift [108]. Alloying has been found to set in around 550 K using AES data [96] and work function measurements [97]. Unfortunately, no ISS studies have been conducted except for Cu deposited on the vicinal Pt(12 12 11) facet where the onset of surface alloying is found above 350 K [109]. A steady dissolution of Cu into the bulk is obtained upon heating [106], and at temperatures above 1350 K the Cu will move out of the Pt bulk and evaporate [110].
The Cu/Pt system has mainly been probed using oxygen [105, 104], hydrogen, and carbon monoxide [95, 97, 98, 101]. No studies have to the authors' knowledge employed high pressure conditions, examined CO_2 interaction, or conducted formate synthesis with this surface.

6.2 Experiments

6.2.1 Experimental procedure

The platinum (111) single crystal was cleaned using cycles of oxygen exposure of 10^{-6} mbar at 850 K, sputtering with Ar, and annealing at 1270 K. This was repeated until no impurities were detected with XPS and ISS.
Cu was deposited on the Pt(111) crystal through physical vapor deposition with a rate of approx. 0.2 ML/min. The sample was then characterized using XPS and ISS in order to determine the amount of copper deposited, and then transferred to the high pressure cell.
As earlier described, the N48 grade CO_2 was purified further with several freeze-pump-thaw cycles using liquid nitrogen, before it was led into the high pressure cell at room temperature. Cleanliness was checked by exposing the Pt(111) crystal to 0.5 bar CO_2. No adsorbed oxygen was subsequently observed with XPS other than a signal due to adsorbed CO from the background pressure of the chamber. The N60 hydrogen was passed over a reduced Cu catalyst cooled with liquid nitrogen before use. Unless otherwise

stated, the sample was subjected to 0.5 bar CO_2 at room temperature for carbonate formation experiments, or a 0.5 bar 70:30 gas mixture of CO_2 and H_2 for formate synthesis experiments.

6.2.2 Characterization of the Cu/Pt system

The copper overlayer was examined using X-ray Photoelectron Spectroscopy (XPS) and Ion Scattering Spectroscopy (ISS). XPS spectra of the sample before and after deposition of 1 ML Cu are shown in figure 6.1, where the assignments of the main peaks are given. The Cu 3s and Cu 3p peaks at approx. 75 eV, 77 eV, and 122.4 eV are masked by the large Pt $4f_{5/2}$ and $4f_{7/2}$ peaks, and Auger lines[3] for Cu are seen in the interval 500-800 eV.

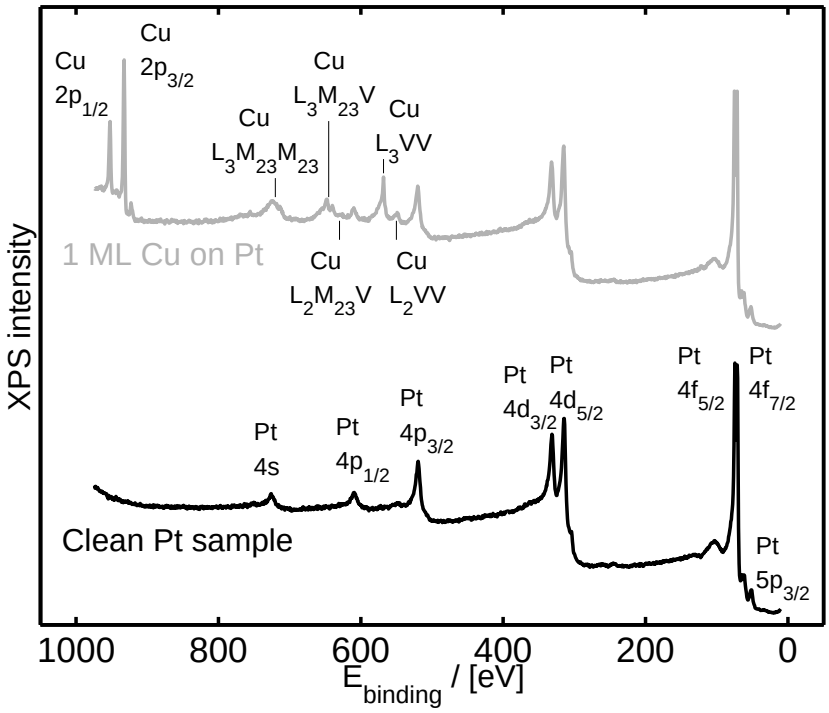

Figure 6.1: Spectra of the clean Pt sample (bottom) and 1 ML Cu on the Pt sample (top). Several Auger peaks from Cu are seen.

The coverage was determined by comparing ISS and XPS data sets for different deposition times, see figure 6.2. Representative spectra are depicted in figure 6.3, where ISS spectra for different amounts of Cu are shown, as well as figure 6.4a and b where close-ups of the Cu 2p region and the Pt 4f region of the XPS spectra are shown. It is seen that the Cu 2p peaks are shifted approximately 1 eV toward lower binding energy at low coverages.

[3]Auger lines arise when an ionized atom relax back to a lower energy state. One electron falls from a higher level to fill an initial core hole. The energy released by this process is simultaneously transferred to another electron which overcomes its binding energy and leaves with a well-defined kinetic energy. These processes are monitored with Auger Electron Spectroscopy (AES).

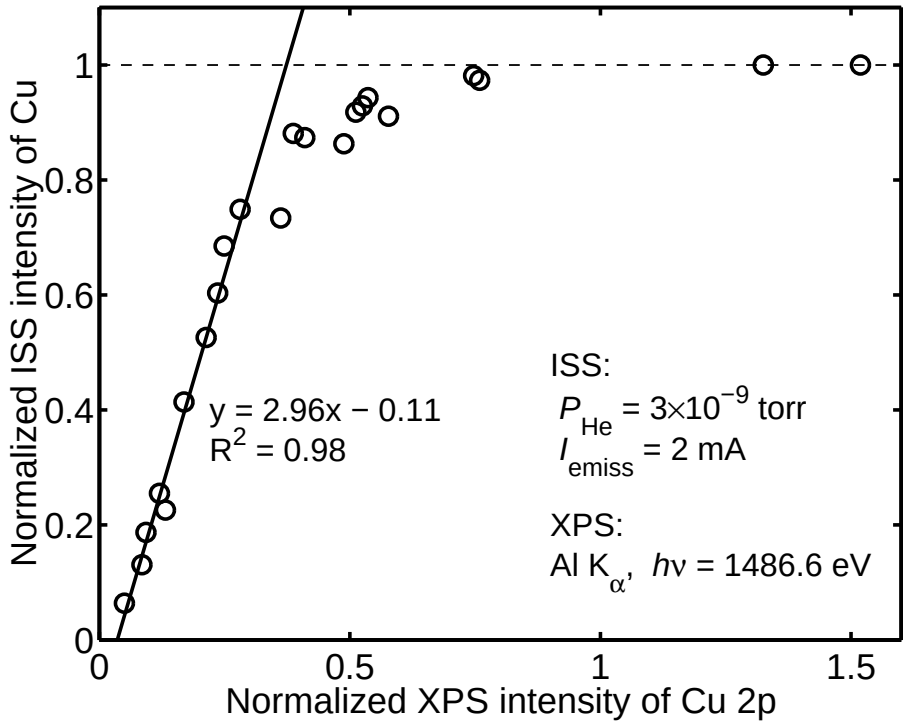

Figure 6.2: Intensity of ISS Cu signal versus intensity of Cu 2p from XPS. For ISS the data was normalized against the sum of the Pt and Cu signals. For XPS Cu signals were normalized against the Pt 4f signal.

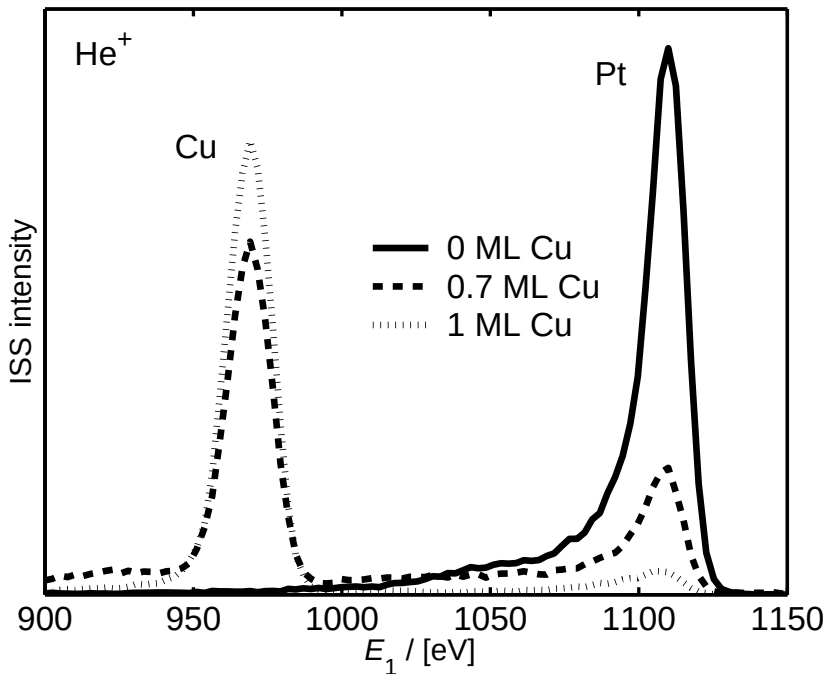

Figure 6.3: ISS spectra of the Cu and Pt signals are shown for 0 ML, 0.7 ML, and approx. 1 ML Cu.

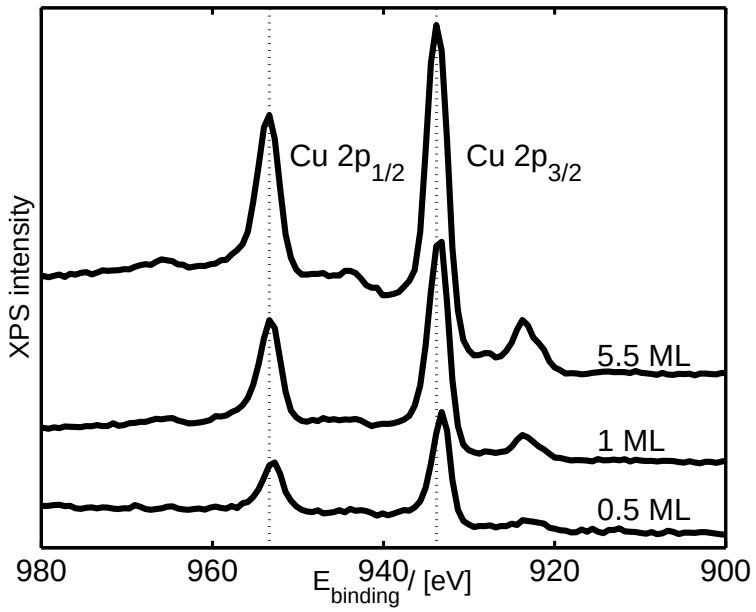

a)

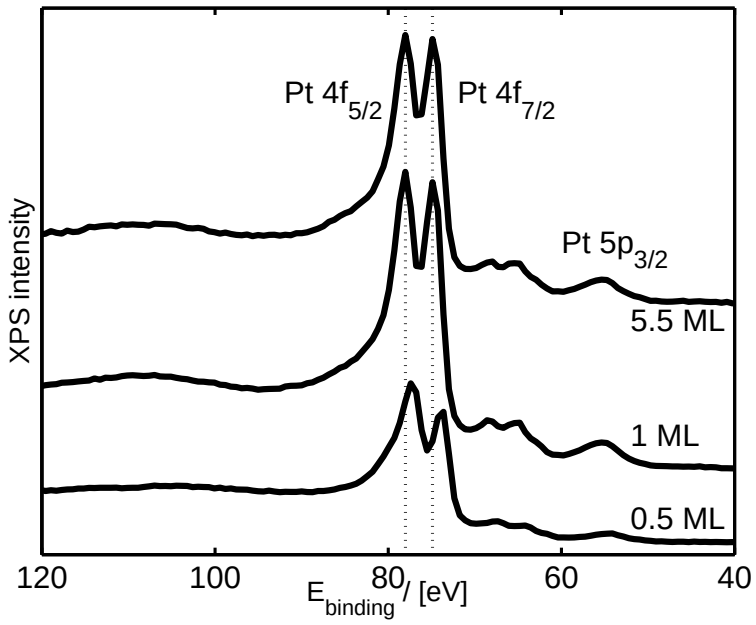

b)

Figure 6.4: XPS spectra of a) The Cu 2p region and b) The Pt 4f region. The Cu and Pt signals are shown for 0.5 ML, 1 ML, and 5.5 ML Cu. Lines are inserted to highlight a shift in binding energy.

In figure 6.2, ISS intensities for Cu were normalized with the sum of the Pt and Cu intensities, and Cu 2p XPS signals were normalized to Pt 4f. It is seen by the deviation of data points above ISS intensities of 0.8 from the linear fit that matters are complicated by the growth of the second layer before the first layer is complete. LEED revealed the emergence of weak rosette patterns around the main first order Pt-spots for 0.6 ML Cu deposited at 425 K indicating onset of second layer formation around this point. Beneath 0.6 ML only the spots due to a lattice with the same spacing as Pt(111) was observed indicating pseudomorphic growth, although the presence of small second layer islands that are not detectable with LEED cannot be excluded. The LEED image obtained for about 1 ML Cu deposited at 425 K is shown in figure 6.5. It resembles the image obtained by Paffett et al. [97] for 1.3 ML and Tsay et al. [104] for 1.2 ML closely. It is seen that the second Cu layer has a larger lattice constant than the first and that it grows rotational commensurate to the Pt(111).

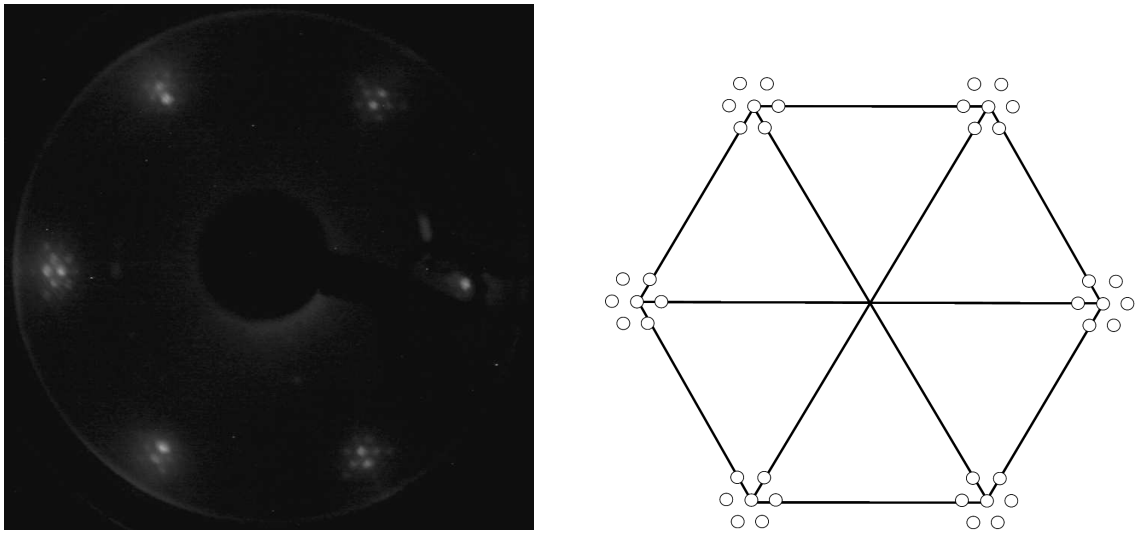

a) b)

Figure 6.5: a) LEED superspots from 2$^{\text{nd}}$ layer before saturation of 1$^{\text{st}}$ ML. $\theta = 0.87$ ML $T_{\text{deposition}} = 425$ K. $E = 64.8$ eV. Picture taken by Ph.D. K. Andersson. b) Schematic of the spots.

The deposition rate of Cu was determined using a linear fit of data points up to 0.6 ML coverage, where ISS spectra are expected to represent the coverage fairly well. The amount of Cu above this point was then estimated on the basis of the deposition rate as it was concluded that the XPS signal for the Cu $2p_{3/2}$ peak would be a poor estimate due to island formation. It is noted that the normalized XPS signal in figure 6.2 seems to have a value different from zero when no ISS signal is present. An explanation may be that alloying is occurring at the Pt steps at the early stages of growth.
The dendritic growth of the copper islands from the platinum steps and uncompleted coalescence seen with STM [102, 103] together with the LEED patterns from the present

study, point to a highly defective surface. Surface defects, steps, and kinks should hence be abundant, and it is clear that defects may rule the game around 1 ML Cu. Furthermore it cannot be excluded that intermediates may induce a reconstruction of the Cu layer during reaction, which for example has been observed for oxygen on Cu(110) [111]. STM studies of the Cu/Pt(111) system with intermediates would be needed to investigate this scenario further.

The onset of surface alloying was determined by heating the sample from 350 K to 600 K with about 1 ML Cu in intervals of 10 K. For each step an ISS spectrum was taken keeping the sample at the selected temperature for 1 min, see figure 6.6.

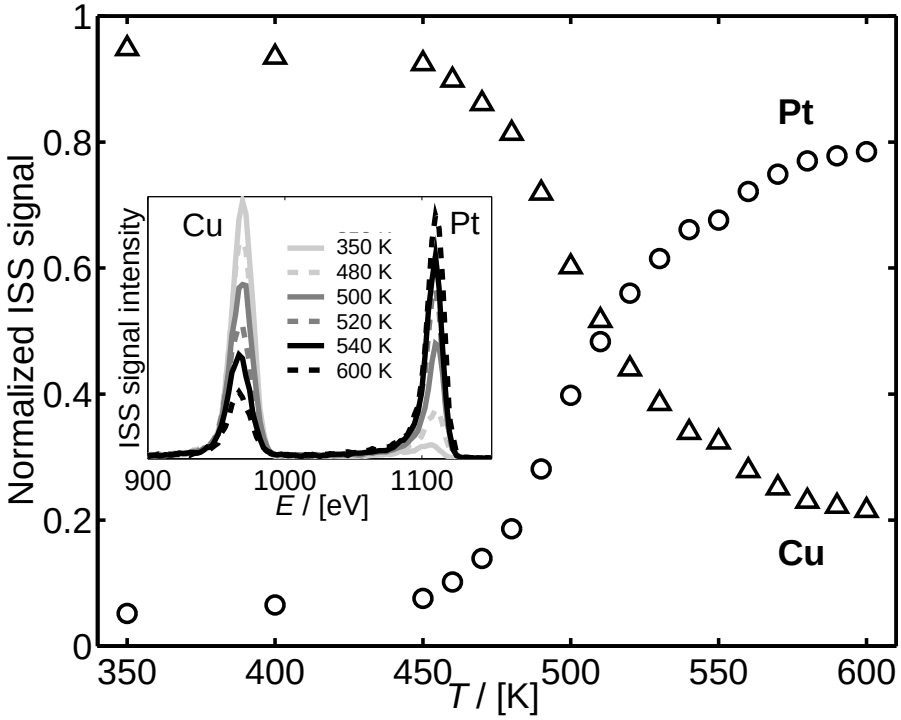

Figure 6.6: The normalized ISS intensities of Cu and Pt during heating. Inset shows raw ISS data.

For data comparison, the same sample was used throughout the experiment. Several precautions were taken to minimize sputter effects, e.g. lowering of He pressure and emission current, together with an increase of the area rastered, while still maintaining an adequate signal. In order to estimate the removal of Cu caused by the small amount of sputter damage during ISS, the decrease in intensity of the first three measurements at low temperature was determined and compared to the observed changes in the following measurements. This did not change the result evident from the figure that surface alloying sets in at 460 K. This temperature is quite low compared to other studies of the system, where alloying around 525-550 K have been reported from AES, LEED, and work function measurements [96, 97, 106]. Our result is, however, similar to the aforementioned onset of a reconstruction of the Pt surface which was also evident in the Cu overlayer as

seen with STM [103]. Further increase in temperature merely leads to a higher rate of Cu migration into the Pt bulk [106].

6.2.3 Carbon dioxide interaction

The importance of CO_2 chemistry on copper surfaces in connection with methanol synthesis and the water-gas shift reaction is well-established. As mentioned previously, methanol is synthesized from a mixture of CO, CO_2, and H_2, with CO_2 hydrogenation being the major pathway [24]. Through isotope labeling experiments, CO_2 has been shown to be the source of carbon in methanol formation [21, 22].
Extensive reviews regarding the surface chemistry of carbon dioxide on several metals have been published by Solymosi [112], and by Freund and Roberts [113]. CO_2 physisorbs on most transition metals, and has only been stabilized on copper on stepped and rough surfaces [114, 115], in connection with alkali doping [116], or by co-dosing oxygen [117].
Several studies have examined the reactivity of CO_2 with the low index Cu surfaces Cu(111), Cu(110), and Cu(100). Habraken et al. [118] observed no interaction of CO_2 with a clean or oxygen covered Cu(l11) surface at 297 and 637 K with exposures up to $5 \cdot 10^5$ L, and Campbell et al. [119] found very slow dissociation of CO_2 with 50 torr at 490 K for Cu(111). Rodriguez et al. [120] employed doses of up to 350 L on a Cu (110) surface at 110 and 250 K, but were also unable to dissociate CO_2. Similar studies by Fu and Somorjai [114], Krause et al. [121], Ernst et al. [122], and Funk et al. [123] found no reaction at low temperature and CO_2 doses for the (110) surface. In stark contrast to these observations, Wachs and Madix [124] reported that 99 % the adsorbed CO_2 on a Cu(110) crystal dissociated into CO and surface oxygen, but unfortunately the pressure and temperature applied were not stated. Moreover, Schneider and Hirschwald [125] reported dissociation on this surface. These results have, however, been disputed [126, 127, 122], and the reactivity may have been due to surface defects.
Dissociative adsorption has only been found at temperatures above 400 K and at pressures of several mbar [119, 128, 129]. Nakamura et al. [128] established that high pressure was required for the reaction to occur on Cu(110), and similarly CO_2 was observed to dissociate on Cu(100) under high pressure (900 mbar) by Rasmussen et al. [129].
Except for a study by Carley et al. [117], who observed that carbonate (CO_3) could be stabilized by co-adsorbing oxygen with CO_2 on Cu(110), stabilization of CO_2 has not been observed on low index Cu surfaces. A different scenario is found on the higher index and rough copper surfaces where reactivity is enhanced. The dissociation to carbon monoxide and oxygen has been reported to occur under UHV conditions for Cu(311) at 150 K [114] and for Cu(332) at 95 K [115]. Studies of polycrystalline Cu [130, 131, 132] have also revealed CO_2 dissociation, although photoinduced reaction should in some cases be considered [133, 134].
A number of studies on stepped single crystals [115, 117], polycrystalline Cu [132], and industrial $Cu/ZnO/Al_2O_3$ catalyst [135, 136] have speculated or observed that carbonate species are present on the surface during reaction. It is clear that additional studies are needed that can provide further insight into the interaction of CO_2 with copper surfaces.

Vibrational spectroscopy experiments

Cu overlayers of 0.4 ML and up to 5.5 ML were subjected to high pressures of CO_2 at room temperature. PM-IRRAS spectra recorded at pressures ranging from 550 down to 10 mbar for 0.9 ML Cu are shown in figure 6.7. A sharp, strong feature was seen at 1435 cm^{-1} similar to results from Millar et al. on Cu/SiO_2 [28]. It shifted down in energy to 1410 cm^{-1} as the pressure was decreased and disappeared when the CO_2 had been pumped out. A stationary feature that persisted in vacuum at 1315 cm^{-1}, and a weak peak at 1215 cm^{-1} - 1205 cm^{-1} (not shown) that presented behavior similar to the 1435 cm^{-1} feature, were also identified.

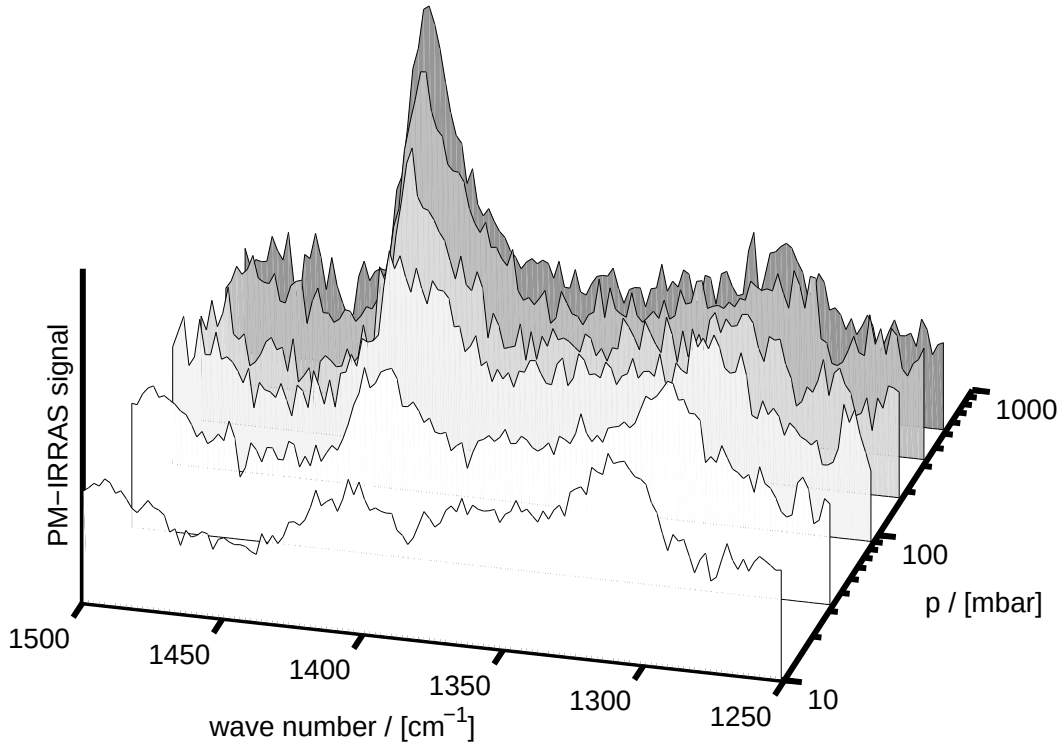

Figure 6.7: PM-IRRAS spectra taken at CO_2 pressures from 550 mbar down to 10 mbar at room temperature.

Subsequent EELS spectra showed peaks at approx. 280, 820, 1050, and 1300 cm^{-1}, see figure 6.8, where the latter vibration at 1300 cm^{-1} is identical to the one seen with PM-IRRAS. The features observed are broad due to the low resolution of the EELS equipment, but despite extensive optimization it was not possible to obtain a FWHM smaller than 19 meV. The vibrations identified here are very similar to those reported in studies done by Stuve et al. on the interaction of CO_2 with an Ag(110) single crystal predosed with oxygen [137]. They assigned the vibrations to the metal - oxygen stretch, v(M-O), the out-of-plane CO_3 deformation, $\pi(CO_3)$, the C-O stretch, v(CO), and the symmetric O-C-O stretch, v_s(O-C-O), respectively. This ensemble of vibrations suggest that the carbonate is lying nearly flat on the surface, as the out-of-plane deformation where the carbon atom

moves back and forth through the plane described by the oxygen atoms are seen. None of the vibrations found at high pressure or under UHV conditions are related to adsorbed CO_2, see table 6.1.

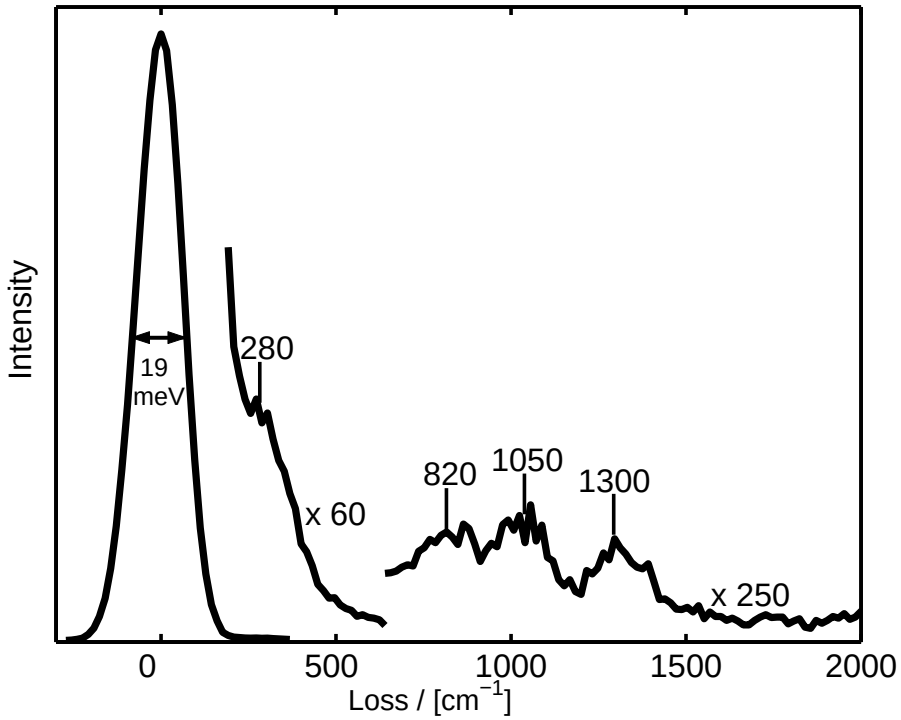

Figure 6.8: EELS spectrum taken after the high pressure experiment. A primary energy of 8 eV was used, and the resolution was 19 meV. Peaks are observed at approx. 280, 820, 1050, and 1300 cm^{-1}.

To clarify and support the experimental evidence, the binding and vibrational states of the carbonate species was examined further on several Cu and Pt systems utilizing DFT calculations performed by Ph.D. student Lars Grabow, and Professor Manos Mavrikakis from University of Wisconsin-Madison. The adsorption was examined on a variety of Cu, Pt, and Cu/Pt alloy surfaces using the Dacapo total energy code [139, 140]. A full description of the calculations may be found in [141].
The specific systems studied were Cu(111), Pt(111), 1 ML Cu on Pt(111) (overlayer), Pt-Cu-Pt(111) (sandwich), and Cu/Pt 1:1 mixed overlayer on Pt(111). For all systems the (111) surface for 2x2 and 3x3 unit cells and the (211) facet on a 3x2 unit cell were studied. The only exception was the Cu/Pt 1:1 mixed overlayer, where only (111) surfaces were examined. Relative intensities were estimated based on dipole changes along the z-axis, perpendicular to the surface, and the IR selection rule hence applies.
It was observed that CO_3 binds as a bidendate species to all (111) surfaces and through all three oxygen atoms on (211) facets with the exception of Pt(211). Monodendate binding geometries were also probed through the calculations, but those states were not stable. On Cu exposing (111) surfaces the two binding O atoms always sit on bridge positions,

Table 6.1: Observed vibrational frequencies compared to results from Stuve et al. [137] together with their assignments. * Hidden by 1360 cm^{-1} peak

	CO_2		CO_3	
Assignment from [137]	Gas, [138] as referenced in [137]	Adsorbed Ag, [137]	Adsorbed Ag, [137]	Adsorbed Cu/Pt, this work
v(M-O)			270	280
Bend, δ(O=C=O)	667	660		
$\pi(CO_3)$			850	820
v(CO)			1050	1050
δ(O=C=O) overtone	1286	1280		
v_s(O-C-O)			1360	1310
v_s(O=C=O)	1333	*		
v_a(O=C=O)	2349	2350		

whereas on Pt exposing (111) surfaces the O atoms are always on top of Pt atoms. On the alloyed Cu/Pt overlayer on top of Pt(111), CO_3 shows hybrid binding to a Pt-top and a Cu-Cu bridge site. It is found that CO_3 binds almost flat at the step on all (211) surfaces, see figure 6.9, except for Pt(211), where top-top binding on two step atoms is observed. For all systems, states adsorbed on steps are generally 0.5 to 0.7 eV more stable than on flat terraces, which indicate that steps are the dominant adsorption sites.
The systems with CO_3 lying flat on a (211) step site exhibit frequencies which are similar to the ones observed in the EELS spectrum, see tables 6.2 and 6.3, whereas no reasonable agreement is found for any of the studied (111) surfaces. For flat surfaces the most intense peaks are around 1800 cm^{-1}, but according to experiments, the strongest peaks are at lower energies. It is therefore concluded that CO_3 preferably adsorbs to steps or step defects based on the considerably enhanced binding energy and the close match of observed and calculated frequencies on those sites.

It is found that all three O atoms interact with the metal surface atoms and thus, it is difficult to compare to literature assignments which are for monodendate or bidendate species, as the modes are somewhat different in the tridendate case. The v(CO) mode is rather a CO_3 star vibration where all three O atoms vibrate simultaneously. Furthermore, it is in some cases hard to clearly distinguish between a symmetric vs. asymmetric (O-C-O) stretch on for example Cu/Pt(211). That is probably due to the very asymmetric way CO_3 is bound to the step. When comparing to experimental literature, [142], the high pressure 1410 - 1435 cm^{-1} feature is similar to an asymmetric O-C-O stretch from a simple carbonate, which is listed at 1415 cm^{-1}. It is speculated that at high pressure the carbonate is raised slightly from the surface due to repulsive adsorbate interactions, which leads to the observation of the O-C-O stretch in PM-IRRAS spectra before purging of the high pressure cell. As pressure decreases, the energy is decreased due to less repulsion,

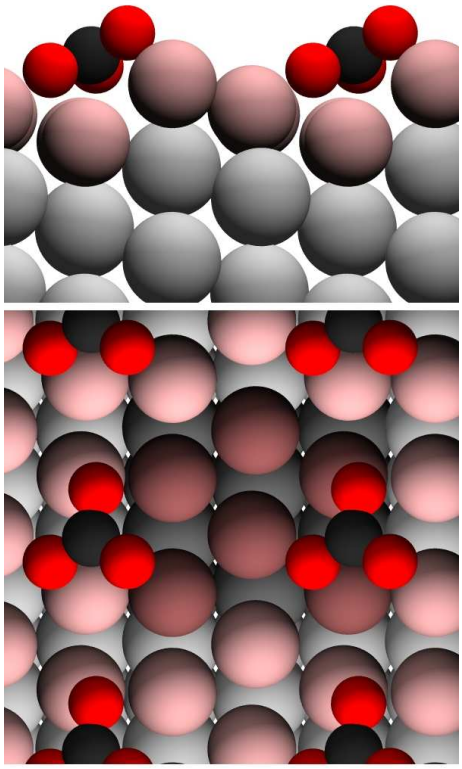

Figure 6.9: Carbonate adsorbed on Cu on Pt(211). The unit cell region is shaded dark. Picture courtesy of Ph.D. student Lars Grabow.

Table 6.2: Comparison of DFT calculations on stepped surfaces and spectroscopic results for vibrational frequencies in cm^{-1}. [a] For the tridentate CO_3 it is difficult to make a clear distinction between the symmetric and asymmetric (O-C-O) stretches. [b] For the tridentate CO_3 v(CO) is a star vibration where all three O atoms vibrate simultaneously.

Mode	Observed	Stepped surfaces			
	EELS/IR	Cu(211)	Pt(211)	1 ML Cu on Pt(211)	Pt-Cu-Pt(211)
v_a(OCO)[a]	1310 /	1447 /	1163	1282 /	1201 /
v_s(OCO)[a]	1435-1410	1262	946	1402	1448
v(CO)[b]	1050	1004	1634	1021	989
$\pi(CO_3)$	820	773	733	751	757
v(M-O)	280	299/245	342	284/309	342/300/148

Table 6.3: Comparison of DFT calculations on flat surfaces and spectroscopic results for vibrational frequencies in cm^{-1}. [a] For the tridentate CO_3 it is difficult to make a clear distinction between the symmetric and asymmetric (O-C-O) stretches. [b] For the tridentate CO_3 v(CO) is a star vibration where all three O atoms vibrate simultaneously.

Mode	Observed	Flat surfaces				
	EELS/IR	Cu(111)	Pt(111)	1 ML Cu on Pt(111)	Pt-Cu-Pt(111)	Cu/Pt on Pt(111)
v_a(OCO)[a]	1310 /	969	1222	969	1242	1134
v_s(OCO)[a]	1435-10	891	961	892	974	878
v(CO)[b]	1050	1759	1629	1742	1611	1688
$\pi(CO_3)$	820	768	710	768	721	749
v(M-O)	280	281/236	314/278	301/215/174	309	309/220

and the carbonate settles down to a point where only the weak 1310 cm^{-1} stretch can be distinguished. It has not been possible to assign the 1205 cm^{-1} high pressure mode. It is most likely some type of O-C-O stretch.

It was not always possible to detect the carbonate with vibrational methods. Certain conditions had to be met in order to get a signal in the spectra. First of all, a high CO_2 pressure had to be applied immediately, as slow inlet in stages of 10 mbar gave a high oxygen coverage which in effect poisoned the surface. This reduced the amount of carbonate produced significantly. Furthermore, an increase in the amount of deposited Cu above 2 ML made it very difficult to detect the carbonate, although it was later observed with TPD and XPS, as presented in the next section. For comparison, similar high pressure experiments were also done on the pristine Pt(111) surface as a blank sample and on a surface alloy corresponding to a Cu/Pt ratio of 1:2, which was produced from 1 ML Cu by annealing the sample briefly at 573 K. Neither of these samples showed any features in PM-IRRAS or EELS spectra except for small amounts of adsorbed CO.

Subsequent TPD and XPS experiments

Following the spectroscopic examinations of the adsorbed species formed during exposure to 0.5 bar CO_2 at room temperature, TPD and XPS were employed to study the decomposition of the carbonate and to estimate the coverage. TPD spectra were recorded in the 300-600 K range with a heating rate of $\beta = 2$ K/s for samples with different amounts of Cu dosed at 425 K on the platinum crystal, as well as the Cu/Pt surface alloy. Spectra for mass 28 and 44 are shown in figure 6.10 together with 0.5 ML CO adsorbed on the clean Pt(111) crystal as a reference. No hydrogen was observed during any of the experiments, and the maximum temperature employed was kept low enough to avoid desorption of the surface oxygen.

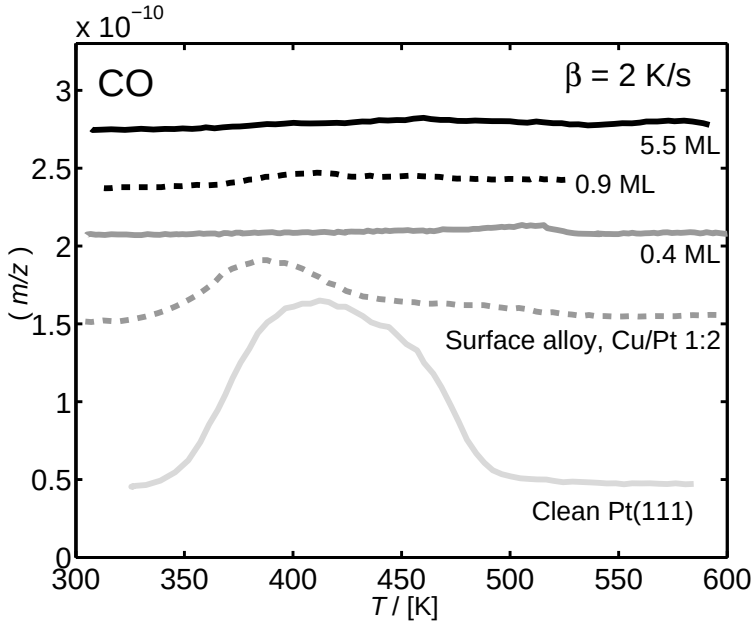

a)

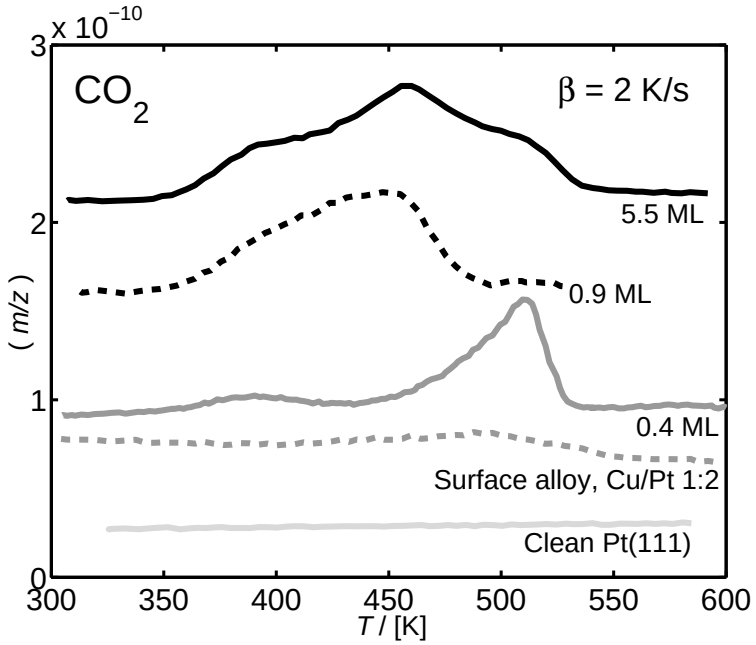

b)

Figure 6.10: TPD spectra of a) CO - mass 28, and b) CO_2 - mass 44 for different amounts of Cu on the Pt(111) crystal, a surface alloy, and the clean Pt(111) crystal. Spectra taken after subjection to 0.5 bar CO_2 are shown for 0.4, 0.9, and 5.5 ML Cu deposited at 425 K as well as the Cu:Pt=1:2 surface alloy produced by flashing 1 ML Cu on Pt to 573 K. The pure Pt crystal predosed with 0.5 ML CO at room temperature is shown for comparison. The temperature ramp was $\beta = 2$ K/s.

The surface alloy did not promote a dissociation of CO_2 or formation of carbonate, but instead adsorbed CO from the background pressure of the chamber. According to the TPD spectrum, figure 6.10a, it was bound weaker than CO adsorbed on a Pt(111) surface. This agrees with prior observations in literature [96] where CO TPDs reveal a lowering of the maximum desorption rate by 100 K. A very weak CO_2 feature is visible in the TPD spectrum for the alloy, figure 6.10b, but it is most likely due to small patches of unalloyed Cu on Pt.
For 0.4 ML Cu which should correspond to a pseudomorphic stretched Cu layer with a low degree of island formation, no CO or H_2 were observed. However, two CO_2 features, a very weak and broad at 390 K and a large and sharp at 510 K with a shoulder toward lower temperature, emerged, see figure 6.10b. At 0.9 ML where second layer Cu islands are present, these features had merged leading to one broad feature with a maximum at 450 K. For even higher Cu coverages where Cu(111) bulk properties are expected to return [97], a more complicated CO_2 spectrum was obtained, probably due to a highly defective surface with extensive island growth. The desorption feature had broadened further to a range of 180 K consisting of a main peak at 460 K with both high and low temperature shoulders. The complicated pattern for the decomposition of carbonate is not explained easily, since the features above 460 K is undoubtedly connected to the onset of surface alloying. As such the features is not related to the magnitude of the binding energy, but to reconstruction of the surface.
It is also seen in figure 6.10b that the amount of carbonate on 5.5 ML Cu is comparable to the amount produced on 0.9 ML, if not larger. This is interesting, as the carbonate on multiple Cu layers was not detected with the vibrational spectroscopy methods. It suggests a somewhat different arrangement of the carbonate at high pressures on the multilayered Cu/Pt(111) system compared to the 0.9 ML Cu/Pt(111) system, although scrambling of the signal due to surface roughness must also be taken into account.

XPS spectra of the O 1s region, figure 6.11a, and C 1s region, figure 6.11b, for the 1 ML Cu/Pt(111) system were recorded before and after TPD. An oxygen peak was initially observed at a binding energy of 531 eV. The area was calibrated with an 0.5 ML CO reference, and it was established that the oxygen peak corresponded to a coverage of approx. 0.9 ML, or 0.3 ML CO_3. In the carbon region a peak was observed at 289 eV with an area corresponding to 0.2 ML. This is in accordance with the ratio expected for carbonate when taking experimental uncertainties into account. Moreover, the carbon peak had disappeared and one third of the adsorbed oxygen was left on the surface after decomposition of the carbonate during TPD, supporting the decomposition step:

$$CO_3{}^* \rightarrow CO_2\ (g) + O^*$$

where * denotes an adsorption site.

Shifts for binding energies of O 1s have been examined on Pt by Norton [143], on Ni by Behm and Brundle [144], and on Cu(110) promoted with Cs and oxygen by Carley et al.

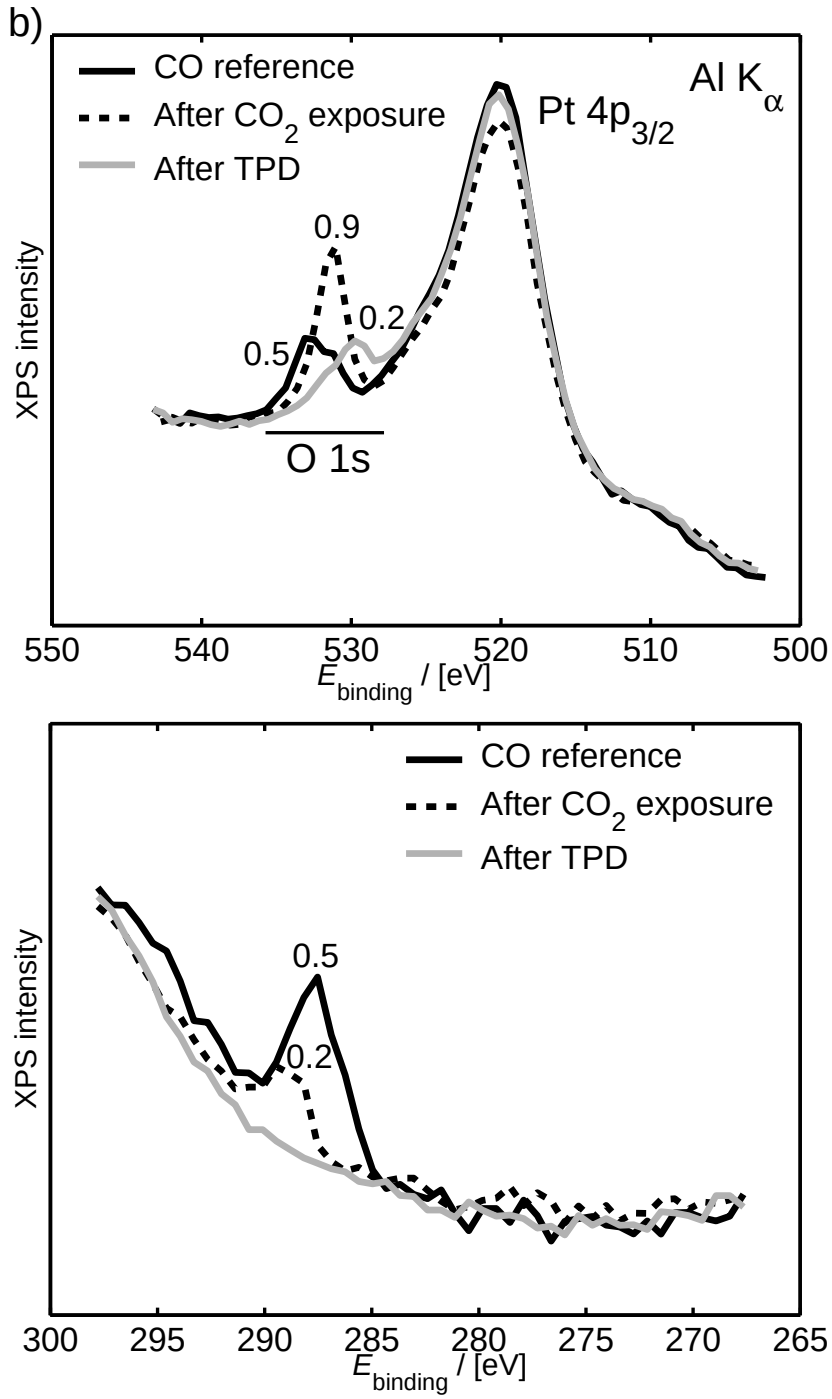

Figure 6.11: XPS spectra for a) oxygen 1s and platinum $4p_{3/2}$. b) carbon 1 s. Before and after TPD on 1 ML Cu/Pt(111). The spectrum for 0.5 ML CO is shown as reference.

[117]. A comparison of their results to this work is found in table 6.4, and it is seen that the positions of the different oxygen species found in the present study agree very well with literature. Furthermore, it was found throughout the experiments that the Cu 2p peaks were not affected by the subjection to CO_2.

Table 6.4: Binding energy of the 1s oxygen core-level for CO_3, CO_2, CO, and O compared to results from the present study. Data on Pt from Norton [143], Ni from Behm et al. [144], and Cs-Cu(110) from Carley et al. [117].

	E_{bin} (Pt) [143]	E_{bin} (Ni) [144]	E_{bin} Cs-Cu(110) [117]	E_{bin} (This work)
CO_2	534.5	-	536	-
CO	532.7	-	533	533.0
CO_3	-	531.2	531	531.1
O	530.2	-	529.8	530.0

Effect of predosed oxygen

Several groups have shown that a pre-existing oxygen coverage influence the amount of carbonate that may be formed during CO_2 exposure [132, 145]. To investigate the effect on the present system, 6 L oxygen corresponding to an 0.15 ML coverage on 0.9 ML Cu/Pt(111) were dosed before high pressure CO_2 exposure at room temperature. This yielded no significant difference for the outcome of the experiment. At 0.3 ML oxygen the carbonate formation reaction was inhibited as previously observed for polycrystalline Cu [132], and for low coverages of preadsorbed oxygen the missing oxygen needed for the equilibrium amount of adsorbed CO_3 was formed by dissociation of CO_2 during high pressure exposure. To elucidate the reaction mechanism, isotope experiments were also conducted. Predosing 6 L $O_2{}^{18}$ and subsequent exposure to 0.5 bar of CO_2 for approx. 30 minutes led to a total exchange of the surface oxygen. No isotopes (mass 46 for $CO^{16}O^{18}$, and mass 48 for CO_2^{18}) were detected in TPD above normal levels for the gas used. Furthermore, only O^{16} was left on the surface after TPD, when checked with ISS, which clearly allows for the distinction of O^{16} and O^{18}, as shown in [75] and figure 6.12. Thus, at high pressure the process is highly dynamic.

Formation of carbonate under UHV conditions was also examined, as predosed oxygen is needed to produce carbonate on Ag in this situation [146]. 2000 L CO_2 were dosed at room temperature with the ion gauge turned off to avoid dissociation of CO_2. It was observed that carbonate in small amounts could be formed on 1 ML Cu when 6 L O_2^{18} had been predosed. In the TPD spectrum, see figure 6.13, two distinct peaks at 450 K and 515 K for both CO_2^{16} and $CO^{16}O^{18}$ as well as a very weak signal for CO_2^{18} are found. ISS subsequently showed no remaining O^{18} left on the sample, revealing a flip in the carbonate geometry. A blank experiment without predosed oxygen was also performed, and as expected no carbonate could be formed in UHV under these conditions.

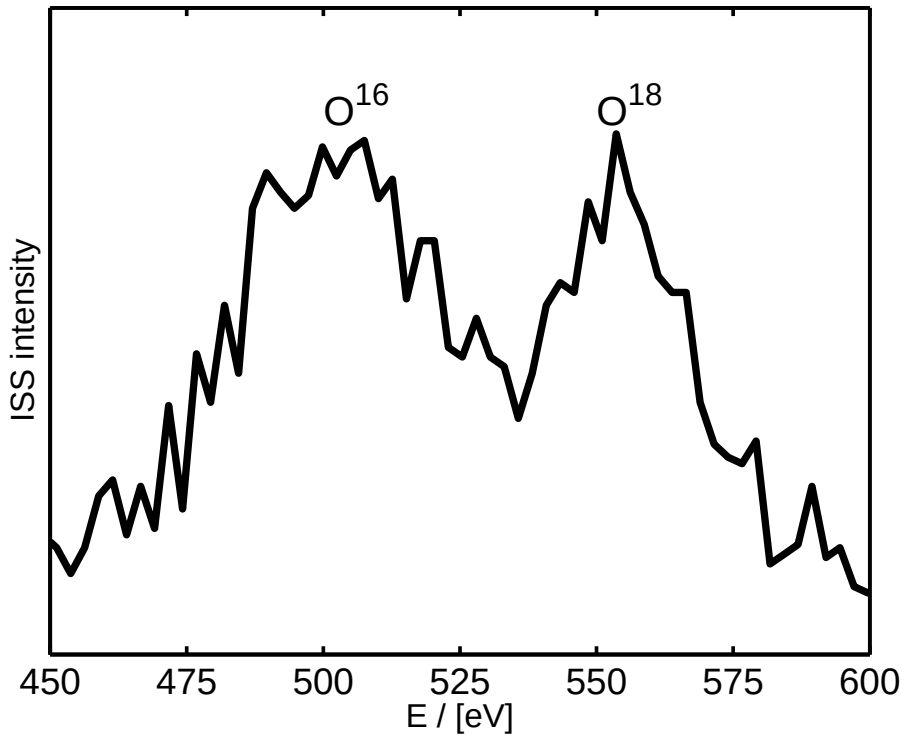

Figure 6.12: ISS spectrum of O^{16} and O^{18} on 1 ML Cu/Pt(111).

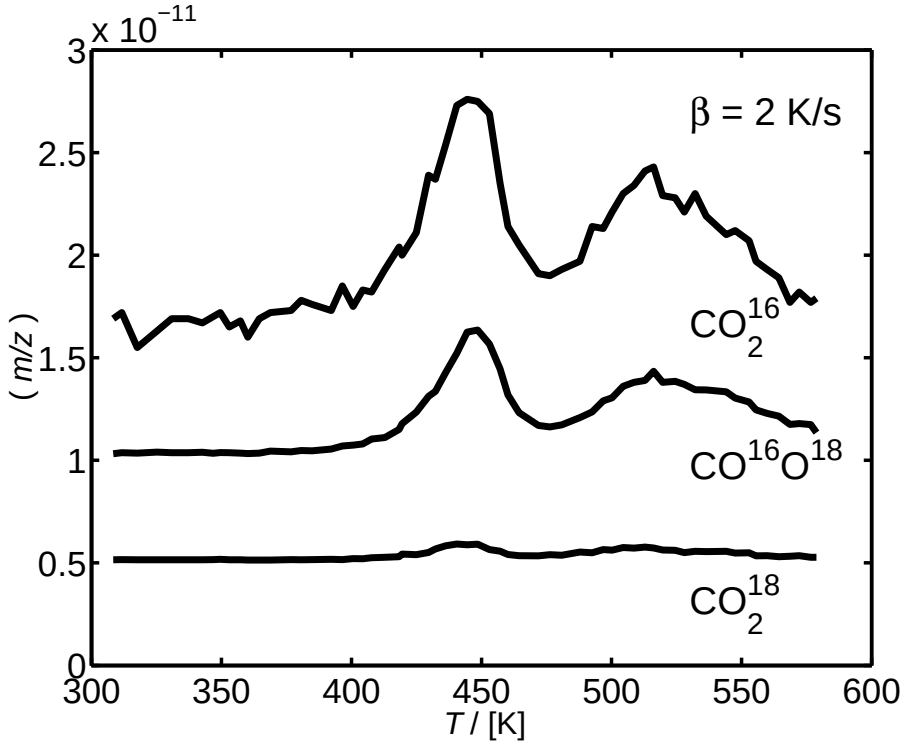

Figure 6.13: TPD spectrum of CO_2^{16} (mass 44), $CO^{16}O^{18}$ (mass 46), and CO_2^{18} (mass 48). 1 ML Cu/Pt(111) dosed with 6 L O_2^{18} and subsequently 2000 L CO_2.

6.2.4 Formate synthesis and decomposition

The presence of formate (HCOO) during methanol synthesis has been established in several investigations of Cu-based catalysts [25, 147, 148, 149], as well as single crystal studies [23, 24]. It is considered a stable intermediate formed due to carbon dioxide hydrogenation in the reaction mechanism for the synthesis [26, 150]. The interaction between CO_2 and H_2 has apart from the reaction between adsorbed or gaseous CO_2 [27] and adsorbed atomic hydrogen, been reported to proceed through the hydrogenation of a surface carbonate formed from the dissociative adsorption of CO_2 and subsequent interaction of surface oxygen with another CO_2 molecule [28, 30]. Despite numerous investigations, controversy still exists about the way that the entire methanol synthesis proceeds on the industrial $Cu/ZnO/Al_2O_3$ catalyst and the involvement of Cu, Zn, and Cu-Zn sites in the mechanism [18]. Fujitani et al. [33, 151] however found that the deposition of Zn on Cu(111) did not influence the rate of formate synthesis, but instead led to stabilization of formate and subsequent promotion of hydrogenation to methanol through a methoxy species. The formate synthesis results obtained on metallic Cu should hence still be relevant for Cu-based catalysts.
The first investigation of formate synthesis at high pressure on a Cu single crystal surface was reported by Taylor et al. [150], who produced the intermediate from a 2.3 bar 70:30 gas mixture of CO_2 and H_2 at 343 K. Several other studies on the decomposition of formate synthesized from H_2 and CO_2, as well as produced by adsorption and heating of formic acid (HCOOH), have been conducted on the low-index Cu facets Cu(111) [151], Cu(100) [152, 153, 150], and Cu(110) [124, 154, 155, 156, 157], as well as Cu powder and Cu/SiO_2 [158, 159, 160], the Cu/ZnO(0001) system [161], polycrystalline Cu and $Cu/ZnO/Al_2O_3$ [25]. Important spectroscopic evidence has been obtained by producing formate from formic acid, but in the present work focus is on the synthesis from CO_2 and H_2 due to the relevance for the methanol mechanism.
Although several studies of high-index Cu surfaces with alkali-metal promotion are reported [162, 163], no investigations of formate decomposition have to the authors' knowledge been reported on the clean surfaces. Nakamura and co-workers [40] studied methanol synthesis on several Cu facets including Cu(311) and reported the presence of formate on this surface. They found that the amount of formate after reaction was correlated to the reactivity for methanol synthesis and that the activity decreased in the order (110) > (311) > (100) > (111). TPD experiments were however not presented. In support of the structure sensitivity for methanol synthesis, Fu and Somorjai [114] found upon comparison of Cu(311) and Cu(110) that where Cu(311) displayed high reactivity toward CO_2 and D_2 dissociative adsorption, Cu(110) was relatively inactive.

The upcoming sections present PM-IRRAS, XPS, and TPD studies of formate synthesis and decomposition, as well as carbonate hydrogenation on Cu/Pt(111).

Formate synthesis - infrared spectroscopy

Formate synthesis was examined on 1 ML and 4.4 ML Cu on Pt(111), as well as the clean Pt sample, and a surface alloy corresponding to a Cu/Pt ratio of 1:2, produced from 1 ML Cu by annealing the sample briefly at 573 K. The sample was subjected to a 0.5 bar gas mixture of 70 % CO_2 and balance H_2, which was the ratio used by Taylor et al. [150]. The sample was then heated from 273 K to 363 K in 10 K steps followed by cooling and purging of the high pressure cell. After having kept the sample at a specific temperature for about 10 minutes, PM-IRRAS spectra were taken to monitor the evolution of formate using the characteristic symmetric O-C-O stretch band, [27, 150, 156]. It has previously been reported that the intensity of the vibrational mode is proportional to the coverage of formate [156]. The asymmetric O-C-O stretch which is usually located at higher wavenumbers [157], was not observed. The lack of this mode indicates a bidentate formate bound perpendicular to the surface.

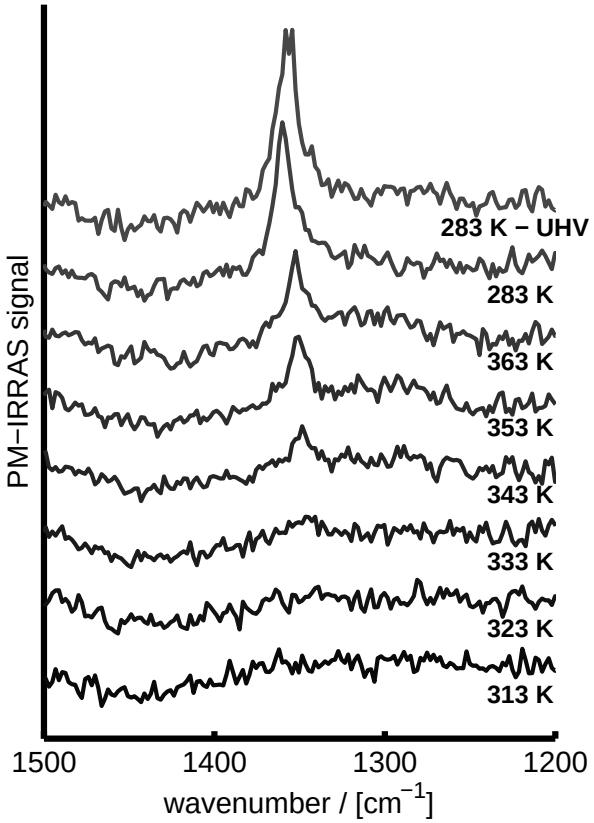

Figure 6.14: Evolution of formate in the temperature range 313-363 K on 1 ML Cu/Pt(111) from a 70%:30% mixture of CO_2 and H_2 corresponding to a total pressure of 0.5 bar. Effect of subsequent cooling and pumping out are depicted in the two uppermost graphs.

In figure 6.14 the spectra are depicted in the wavenumber range 1200 cm^{-1} to 1500 cm^{-1} for each 10 K step from 313 K to 363 K for the synthesis over 1 ML Cu/Pt(111). Formate

was readily formed on the modified Cu surface and was detectable above the noise level around 343 K at approx. 1348 cm^{-1}. This is in good agreement with other reports of the peak position for the symmetric O-C-O stretch of bridging bidentate formate on low-index Cu surfaces [27]. The amount of formate peaked at 1352 cm^{-1} when the temperature was raised to 363 K.
On returning to 283 K the amount increased significantly; possibly due to the second pass of the optimal temperature for the synthesis. The peak moreover shifted further up in energy to 1360 cm^{-1}, which may be explained by the increase in the repulsive interaction due to a larger amount of formate on the surface, as previously described by [156]. After pump out a downshift of 4 cm^{-1} to 1356 cm^{-1} was observed.
Formate was not detected with PM-IRRAS when large amounts of Cu had been deposited. Similarly, the experiments conducted on the pristine Pt(111) surface as a blank sample and on the surface alloy did not yield any features in the PM-IRRAS spectra except for small amounts of adsorbed CO.

Formate decomposition - TPD

After the high pressure experiment the sample was transferred back into the UHV chamber and temperature programmed desorption was performed with a heating rate of 2 K/s on the 1 ML and 4.4 ML Cu/Pt(111), as well as the 1:2 Cu:Pt surface alloy. The signals from masses 2, 28, and 44 for these systems are shown in figures 6.15, 6.16, and 6.17.

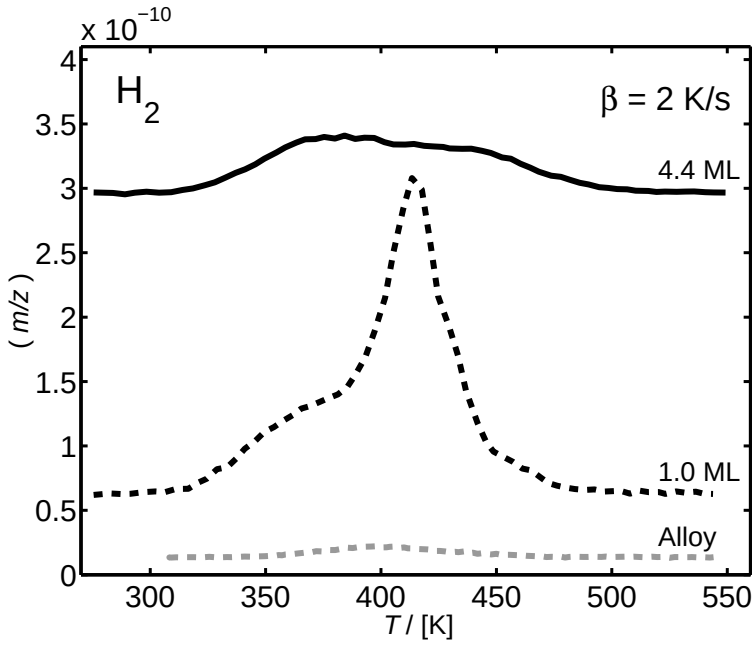

Figure 6.15: TPD spectrum of H_2 - mass 2 for different amounts of Cu on the Pt(111) crystal. Spectra taken after subjection to 0.5 bar 70% CO_2 and 30% H_2 are shown for a 1:2 Cu:Pt surface alloy, 1.0 ML, and 4.4 ML Cu deposited at 325 K. The temperature ramp was $\beta = 2$ K/s.

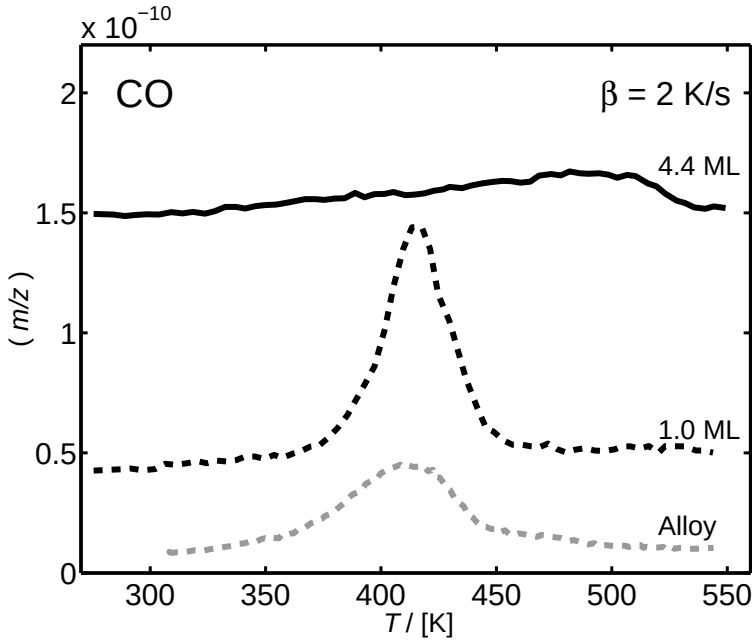

Figure 6.16: TPD spectrum of CO - mass 28 for different amounts of Cu on the Pt(111) crystal. Spectra taken after subjection to 0.5 bar 70% CO_2 and 30% H_2 are shown for a 1:2 Cu:Pt surface alloy, 1.0 ML, and 4.4 ML Cu deposited at 325 K. The temperature ramp was $\beta = 2$ K/s.

The alloy displays CO desorption, as seen in figure 6.16, whereas the signals from hydrogen and CO_2 are hardly visible. The TPD spectra for approx. 1 ML Cu where second layer island growth has begun, displays a H_2 desorption feature from 315 K to 500 K with a low temperature shoulder. The maximum desorption is found at 415 K. The low temperature shoulder is attributed to H_2 adsorbed on Pt(111), which according to Christmann et al. [164] desorbs at approx. 380 K at low coverage. Desorption may occur from the uncovered edges and the backside of the Pt crystal, as well as parts of the Pt surface that is exposed due to holes in the Cu adlayer. The Cu adlayer itself was found by Paffett et al. [97] not to adsorb H_2, as they observed complete poisoning of hydrogen adsorption employing 160 L H_2 at 150 K for 1.15 ML Cu on Pt(111). As the dissociative adsorption of H_2 however is an activated process facilitated by high vibrational energy [165], this does not rule out that hydrogen is indeed adsorbed on the Cu overlayer in the present study, where the pressure and temperature applied are significantly higher.
The CO_2 decomposition takes place from 365 K to 475 K with the same peak temperature, 415K, as found for H_2. The coincidence of the H_2 and CO_2 peaks is characteristic for the decomposition of formate [150]. At these temperatures the decomposition should furthermore not be influenced significantly by surface alloying, as the onset has been found at 460 K. Apart from a high temperature shoulder in the range 450 - 475 K the CO_2 feature is fairly sharp.
The CO signal for 1 ML Cu is located in the range 375 K to 455 K with a peak at 415 K more or less corresponding to the expected signal due to the cracking pattern for CO_2.

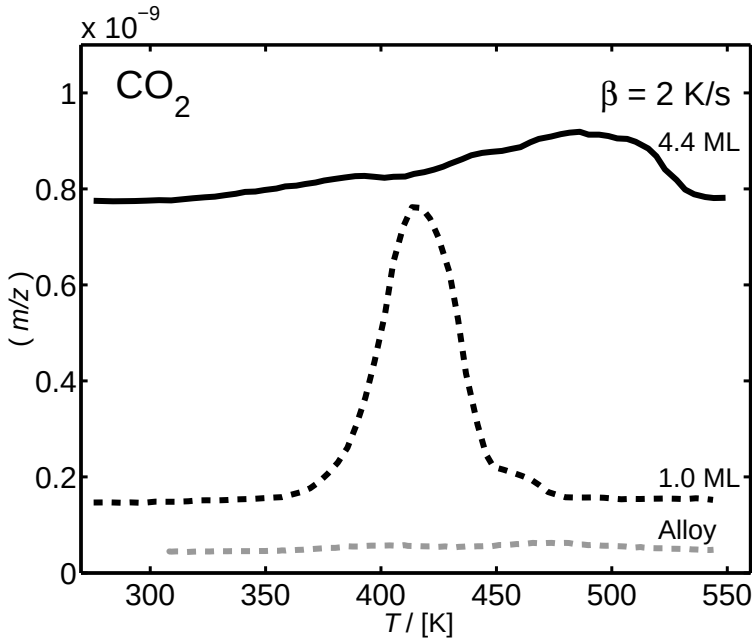

Figure 6.17: TPD spectrum of CO_2 - mass 44 for different amounts of Cu on the Pt(111) crystal. Spectra taken after subjection to 0.5 bar 70% CO_2 and 30% H_2 are shown for a 1:2 Cu:Pt alloy, 1.0 ML, and 4.4 ML Cu deposited at 325 K. The temperature ramp was $\beta = 2$ K/s.

The lack of CO adsorption is expected, as Paffett et al. [97] showed a linear relation for the poisoning effect of Cu coverage on Pt(111) toward CO adsorption.

At the highest amount of Cu, estimated to be 4.4 ML, the H_2 signal features a double peak and has broadened to the range 315 K - 520 K with peak maxima located at 385 K and 435 K. The CO_2 signal has also become more complicated. The desorption takes place from 310 K to 540 K with two shoulders at approx. 390 K and 445 K before the main peak at 485 K. The two shoulders coincide to some extent with the H_2 peaks, indicative of the formation of a small amount of formate below the detection limit of the infrared spectrometer. The high temperature CO_2 state is consistent with the previously observed decomposition of carbonate, and it is interesting that the formate synthesis does not seem to proceed as well on 4.4 ML Cu, as on lower amounts. The Cu layer is expected to relax into a bulk like Cu(111) lattice, which should correspond to the situation for Cu(111) [97]. It is speculated that the peaks from CO_2 and H_2 on 4.4 ML Cu/Pt(111) at approx. 450 K is due to decomposition of formate adsorbed on relaxed Cu(111) facets. As before on 1 ML Cu, the CO signal is attributed to the CO_2 cracking pattern.

6.2.5 Hydrogenation of carbonate

To address the possible connection between carbonate and formate for the hydrogenation of CO_2 in the methanol synthesis reaction mechanism, carbonate formed during high pres-

sure exposure as previously described, was subjected to hydrogenation. After formation of the carbonate in 360 mbar CO_2, the HPC was purged and the amount of carbonate that had been formed was quantified with XPS. The sample was then transferred back into the HPC, where it was subjected to 210 mbar H_2 at room temperature. XPS spectra were taken before and after the hydrogenation, see figure 6.18. It is found that the oxygen peak decreased to 0.4 of the original area after the adsorbed CO_3 was exposed to H_2. Subsequent TPD spectra, see figure 6.19, showed a similar drop in intensity of desorbing CO_2 compared to TPD spectra taken after carbonate formation. The H_2 desorbed from 340 K to 480 K and the peak was symmetric around the maximum at 410 K. CO_2 desorbed from 380 K to 510 K with a max. around 460 K, which is hard to determine as the peak is highly irregular. The overlap between H_2 and CO_2 in the range 380 - 480 K may indicate the presence of formate. This could not be proven with PM-IRRAS or EELS due to the very low concentration. Apart from the CO_2 cracking pattern a small peak around 400 K was also observed for CO.

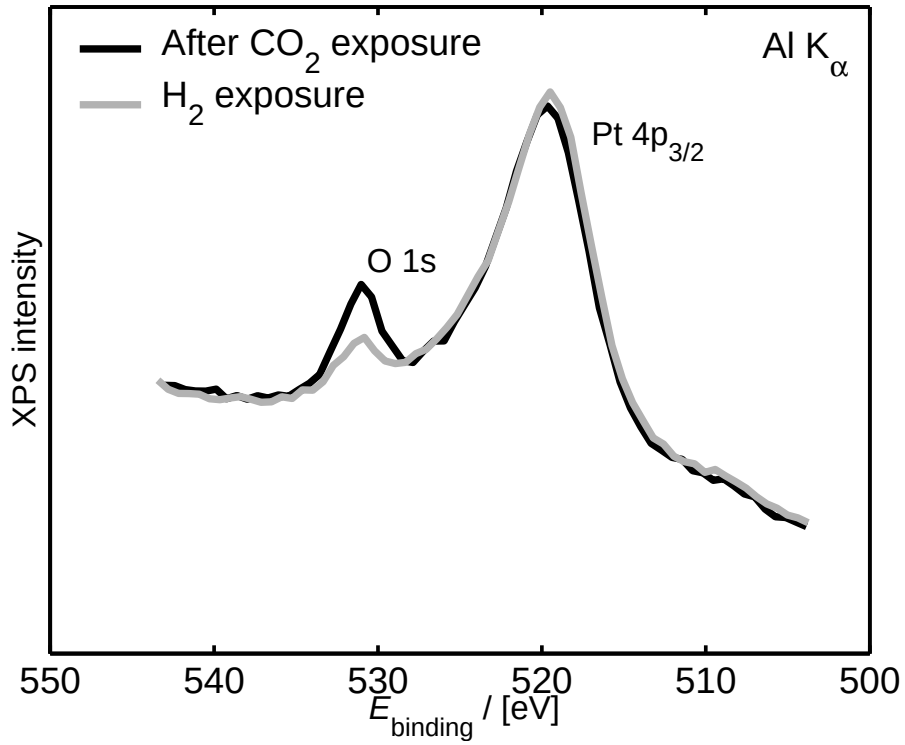

Figure 6.18: XPS spectra of the O 1s and Pt 4p region after the formation of carbonate from 0.3 bar CO_2 and after the hydrogenation of that carbonate with 0.2 bar H_2 at room temperature.

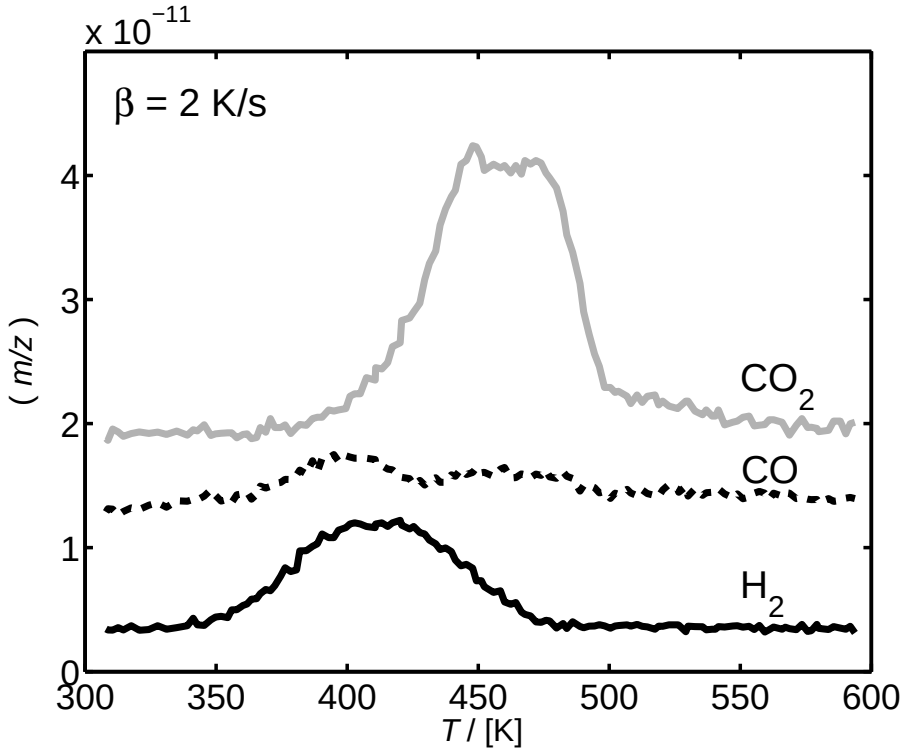

Figure 6.19: TPD spectrum of H_2, CO, and CO_2 after hydrogenation of carbonate at room temperature on 1 ML Cu/Pt(111). The temperature ramp was $\beta = 2$ K/s.

6.2.6 Discussion

Formate synthesis and decomposition

The formate synthesis on the modified Cu surface seems to behave as other systems reported in literature with a clearly visible symmetric O-C-O stretch around 1350-1360 cm^{-1} and an optimal rate in the 353-363 K range. It may seem that this supports the belief that the synthesis is structure insensitive [27], but no clear evidence can be given, as the apparent activation energy and rate were not established due to the fact that the sample differs in each experiment.

In this case, it is more interesting to look into the trends of the decomposition temperature on different Cu surfaces to establish whether the structure and density of the Cu surface have any influence on the reactivity. It was found that the decomposition temperature for formate on 1 ML Cu/Pt(111) is 415 K, which is somewhat low compared to TPD results obtained on low-index Cu. Fujitani et al. [151] reported that formate species synthesized from a 1.013 bar 1:1 mixture of H_2 and CO_2 at 353 K on Cu(111) started to decompose at 425 K, and disappeared at 480 K with a 0.5 K/s heating rate. The maximum desorption rate was estimated from the slope of their graph to be at approx. 460 K. Similar results were obtained on the Cu(100) facet with the adsorption of formic acid [152, 153] where the decomposition again set in above 425 K with a peak temperature of 460 K and 480 K, respectively. Evidence for the formate species produced from both formic acid

and by synthesis from a 2.3 bar 70:30 gas mixture of CO_2 and H_2 at 343 K on Cu(100) was presented by Taylor et al. [150]. The desorption temperature obtained with a heating rate of 2 K/s was lower than otherwise reported, as the TPD peak moved from 450 K at low exposures to 425 K at high exposures. This is more in line with our present work.

Any clear difference between the formate decomposition on the Cu(111) and the Cu(100) facets cannot be firmly deduced from these results, but somewhat higher peak decomposition temperatures are generally reported for the Cu(110) facet. Wachs et al. [124] found the decomposition of formate species formed from methanol oxidation to have a maximum at 470 K at a heating rate of 4-5 K/s, and Ying and Madix [154] obtained a similar result for formate derived from formic acid, as 473 K was found with a heating rate of 3.4 K/s. This was further corroborated with experiments where formate produced from formic acid as well as formaldehyde and oxygen was found to decompose at 480 K with a 4 K/s rate and at 470 K with 2 K/s [155, 157]. Lower temperatures were however obtained by Hayden et al. [156], as formate derived from formic acid was found to decompose with a peak maximum at 450 K.

Studies of formate decomposition on Cu/SiO_2 generally display lower peak decomposition temperatures. Yatsu et al. [160] presented TPD data for formate species synthesized from a mixture of 250 mbar CO_2 and 760 mbar H_2 at 381 K. The desorption peaks of CO_2 and H_2 were observed to coincide at 410 K with a heating rate of 2 K/min. A slightly higher temperature was obtained by Iglesia and Boudart [158], who found decomposition of formate on both Cu/SiO_2 and Cu powder catalysts predosed with formic acid (10-200 mbar, room temperature) in the range 400 K - 460 K. For H_2 a TPD spectrum peaking at 425 K was displayed. Millar et al. [159] studied the decomposition after dosing HCOOH around 300 K by monitoring the intensity of the symmetric O-C-O stretch with FT-IR while heating the sample at 6 K/s. They found decomposition peaked at 433 K on a reduced catalyst, and at 408 K on a reoxidized.
Systems more representative of the industrial catalyst were investigated by Yoshihara et al. [161] and Bowker et al. [25]. The Cu/ZnO(0001) system [161] was examined by dosing 3 L of HCOOH onto clean and Cu-predosed ZnO(0001) at 325 K. For 1.85 ML Cu with a rate of 5K/s a peak due to decomposition on Cu sites was found at 480 K, which is comparable to the results for most of the low-index surfaces. Bowker et al. [25], who examined both polycrystalline Cu and $Cu/ZnO/Al_2O_3$, found slightly lower temperatures. Codosing of 81 mbar H_2 and 81 mbar CO_2 at 305 K yielded a peak at around 430 K. After production of methanol at 500 K in a 10:80:10 mixture of CO_2, H_2, He and subsequent cooling in the reactant gas, the TPD with a rate of 20 K/s for the $Cu/ZnO/Al_2O_3$ catalyst yielded a CO_2 peak at 420 K which to a large extent coincided with the H_2 located at slightly lower temperature. The results obtained on Cu-based catalysts are in good agreement with the present result.

That the surface structure evidently has importance was as previously mentioned shown by Nakamura and co-workers [40], who found that the amount of formate after reaction

was correlated to the reactivity for methanol synthesis and that the activity decreased in the order (110) > (311) > (100) > (111). In support of this, it has been shown that Cu(311) displays high reactivity toward CO_2 and D_2 dissociative adsorption, whereas Cu(110) is relatively inactive [114]. Nakamura and co-workers [166] also reported that the activation energies and pre-exponential factor for formate decomposition varies significantly on the different low index facets of copper indicating that the decomposition of the formate species is structure sensitive. However, there seems to be no clear correlation between the density and structure of the Cu surface and the decomposition temperature of formate when reviewing the literature. If any, the consistency of the reports for the less close-packed Cu(110) suggests that formate decomposes at higher temperature, which is not in agreement with our observation of a lower temperature for a stretched Cu(111) surface. It is speculated that the Cu(110) surface experiences an adsorbate induced reconstruction to (2x1)O - an added row reconstruction involving Cu atoms that detach from step edges [111, 167]. A destabilization of Cu(110) due to formate has been observed by Harrington et al. [168] by exposure of the surface to formic acid.
The present result suggests that the location of the maximum desorption rate for formate moves down in temperature as the surface become stretched and hence less closed-packed. This may seem counter-intuitive as a stronger binding and thus a higher desorption temperature would normally be expected. The situation is however different when a decomposition mechanism is involved. From a potential energy diagram view point, the activation energy for the formate synthesis from CO_2 and H_2 may still be fairly high. If, however, a low barrier exists when going from formate to the decomposition products, that is, the internal bonds are weakened due to the stronger binding to the surface (filling of antibonding orbitals), decomposition will be favored at a lower temperature than on unmodified Cu(111).

Carbonate formation and hydrogenation

Evidence has been presented for the dissociation of CO_2 and subsequent formation of a stable carbonate species on Cu/Pt(111) when the surface is subjected to a high pressure of CO_2 at room temperature. PM-IRRAS spectra show a pressure dependence which is interpreted as a shift in position of the carbonate, and subsequent EELS spectra in UHV yield states that are consistent with a configuration lying nearly flat on the surface. DFT calculations present steps and defects as the most likely carbonate adsorption sites as the binding energy is 0.5-0.7 eV larger compared to flat terraces. Furthermore, the calculations yield frequencies close to those observed for stepped slabs.
Decomposition of the carbonate is seen in a wide temperature range in TPD with the main peak around 450 K for 0.9 ML Cu, and it is found with XPS that approx. one third of the adsorbed oxygen is left on the surface after TPD corresponding to the expected ratio for the decomposition. Furthermore, it was observed under UHV conditions that small amounts of preadsorbed atomic oxygen significantly lowers the activation barrier for carbonate formation. The production of carbonate must then be initiated by dissociation of CO_2 due to the following elementary steps, where * denotes a surface site:

$$CO_2\ (g) + * \rightarrow CO_2*$$
$$CO_2* \rightarrow CO(g) + O*$$
$$CO_2* + O* \rightarrow CO_3* + *$$

For methanol synthesis catalysts it has been found that the working copper surface is partially covered with adsorbed oxygen [169], and as mentioned earlier, there are several studies [135, 115, 117, 132] that have speculated or observed that a carbonate species is involved in the reaction steps on high index and rough Cu surfaces.

From the results presented in section 6.2.5, it is evident that carbonate is destabilized; in all probability due to hydrogenation resulting in formate as seen by [28]. The presence of the formate species is not firmly established, but this is however not necessarily surprising, since it may be hydrogenated itself under these conditions in agreement with previous results [170], where the hydrogenation was investigated at high H_2 pressure (5.8 bar) from 333 - 363 K. Usually, formate is believed to be formed in one step from adsorbed atomic hydrogen and CO_2, and there are not many proposals and theoretical approaches to reaction mechanisms which involve carbonate intermediates as a possible path for the hydrogenation of CO_2 [32]. Waugh [17, 30] has suggested a reaction mechanism, where the formation of a transient carbonate and subsequent hydrogenation to formate explains the activation of CO_2 and H_2. This has furthermore been observed experimentally by Millar et al. on Cu/SiO_2 [28]. It thus seems that the key step is the activation of CO_2 through a carbonate intermediate, and that this activation is necessary to produce formate:

$$CO_2\ (g) + * \rightarrow CO_2*$$
$$CO_2* \rightarrow CO(g) + O*$$
$$CO_2* + O* \rightarrow CO_3* + *$$
$$H_2\ (g)\ 2* \rightarrow 2\ H*$$
$$H* + CO_3* \rightarrow HCOO* + O*$$

The examination of the methanol and formate synthesis, as well as the decomposition on high-index copper single crystal surfaces is somewhat overlooked and deserves attention, as it may help to elucidate the connection between carbonate and formate. It is evident that strained Cu(111) overlayers behave differently than pristine Cu(111) in relation to the interaction with CO_2 and the formate synthesis. It is however also clear that further studies with other techniques such as STM are needed to elucidate the mechanism of carbonate and formate hydrogenation, as well as the presence of a possible adsorbate induced reconstruction of the surface.

6.2.7 Summary and conclusions

The conclusions of the presented interaction of CO_2 and H_2 with a strained and rough Cu overlayer on Pt(111) may be summarized as follows:

- Deposition of Cu on a Pt(111) crystal at a substrate temperature of 425 K results in the onset of second overlayer formation at around 0.6 ML Cu. Surface alloy formation is found to set in around 460 K, which is low compared to other investigations in the literature.

- It has been shown by means of PM-IRRAS, EELS, XPS and TPD that dissociative adsorption of CO_2 occurs when subjecting the Cu/Pt(111) sample to 0.5 bar CO_2 at room temperature, and that a stable carbonate species is formed. In ultra-high vacuum, small amounts of preadsorbed atomic oxygen significantly lowers the activation barrier for carbonate formation. The observed vibrational modes are consistent with a configuration which is lying nearly flat on the surface in UHV and is slightly raised under high pressure. DFT calculations present steps and defects as the most likely carbonate adsorption sites and yield frequencies for stepped slabs close to those observed experimentally. Carbonate decomposition is seen in a wide range in TPD spectra with the main peak around 450 K for 0.9 ML Cu, and it is found with XPS that approx. one third of the adsorbed oxygen is left on the surface after TPD. Furthermore, results suggest that the carbonate may be hydrogenated into formate.

- It has been shown by means of PM-IRRAS and TPD that formate can be synthesized from a 0.5 bar gas mixture of 70 % CO_2 and balance H_2 on Cu/Pt(111), and that the optimal rate is found around 353-363 K. Formate decomposes at 415 K for 1 ML Cu, which is slightly lower than previously reported on low-index Cu surfaces, but in good agreement with studies on Cu-based catalysts. This suggests an altered reactivity of the stretched Cu compared to Cu(111). At higher Cu coverages (4.4 ML) an interesting situation arises, as only small amounts of formate is synthesized and carbonate is present.

Chapter 7

Trends of the water-gas shift reaction

In the following sections, work done during my M.Sc. thesis [171], which was continued throughout my Ph.D. [56, 172, 173] is presented. The microkinetic model covering multiple transition metals is summarized and results are presented. Furthermore it is attempted to simplify the description of the model by correlating the binding energies for carbon monoxide and oxygen, which are found to be good descriptors for the reaction. In the second part of this chapter, experiments relevant to the model are presented and compared to the computational results.

7.1 Microkinetic Modeling

Inspired by recent work with modeling and optimization of the ammonia synthesis catalyst [174, 175], a microkinetic model for WGS over copper catalysts [176, 177] was expanded to describe the reaction over other transition metals in order to provide insight into how the low-temperature WGS catalyst may be improved. The expanded microkinetic model has been described in detail in [56, 171, 178] and is based on the work of Ovesen and co-workers [26, 176, 177, 31], which involved microkinetic modeling of the water-gas shift reaction on different low index Cu facets.

It is assumed that the mean field approximation is valid. It states that all adsorbed species are distributed randomly on the active sites and that there are no adsorbate-adsorbate interactions. It must be noted that an exception from the approximation is made, as formate, HCOO, is modeled to possess a repulsive adsorbate-adsorbate interaction. Species like adsorbed hydroxyl groups and water molecules will also interact as they form islands on the surface, but this is neglected. It was furthermore assumed that a Langmuir-Hinshelwood mechanism applies, allowing only reaction between species adsorbed on the catalyst surface.
In order to build the model the overall reaction is split up into elementary steps, describing how the reactants will adsorb onto the surface, dissociate, react with one another, and finally desorb as products. The theory needed for the kinetic model has previously been published by Ovesen et al. [176, 177]. Kinetic and thermodynamic parameters for

the elementary reactions involved were taken from data presented by Ovesen et al. [31]. It must be noted that the model, which is summarized in the following sections, only treats metallic Cu, whereas Cu^+ also has been suggested as a possible active site [16].

7.1.1 Reaction Mechanism

Two types of reaction mechanisms have been proposed for the WGS reaction; the associative reaction mechanism, which is also known as the adsorptive mechanism, and the surface redox or regenerative reaction mechanism. Both mechanisms were described in 1920 by Armstrong and Hilditch [179]. The associative mechanism generally depicts a reaction path in which CO and H_2O adsorb on a catalyst surface and then combine to form an intermediate, such as formate (HCOO), which subsequently decomposes into CO_2 and H_2. The surface redox pathway on the other hand describes a situation where water oxidizes a reduced site on the surface yielding H_2. Carbon dioxide is then formed by reduction of the oxidized active site with carbon monoxide. The literature on both mechanisms has been reviewed by Rhodes et al. [8].

The WGS reaction has previously been studied extensively by Campbell and co-workers [180, 181, 182] and modeled by Ovesen et al. [176, 177, 183, 31] on Cu surfaces and industrial Cu catalysts for the low-temperature shift with the use of the surface redox mechanism [182]. The reaction mechanism used by Ovesen and co-workers consists of the following elementary steps:

1. $H_2O(g) + * \rightleftharpoons H_2O*$
2. $H_2O* + * \rightleftharpoons OH* + H*$
3. $2OH* \rightleftharpoons H_2O* + O*$
4. $OH* + * \rightleftharpoons O* + H*$
5. $2H* \rightleftharpoons H_2(g) + 2*$
6. $CO(g) + * \rightleftharpoons CO*$
7. $CO* + O* \rightleftharpoons CO_2* + *$
8. $CO_2* \rightleftharpoons CO_2(g) + *$
9. $CO_2* + H* \rightleftharpoons HCOO* + *$

Where * represents an active site on the surface, and X* depicts an adsorbed species.

Elementary steps 2 and 4, the dissociation of the first and second hydrogen atom from the water molecule, together with step 7, the reaction between adsorbed CO and O to

form adsorbed CO_2, are considered as slow, rate-controlling steps. A reaction between two adsorbed hydroxyl intermediates to form adsorbed water and atomic oxygen, step 3, offers a low barrier pathway to a dissociation of the OH group. It is noted that a site is defined as two copper atoms, which can easily be seen, as formate, HCOO, is bidentate and binds through its two oxygen atoms to two surface atoms. This species is treated as a spectator species in the mechanism, which means that it may block the active sites and lower the net reaction rate, if the conditions favor its production.

The following analysis relies on the presented elementary steps comprising the surface redox mechanism, but the method can easily accommodate future alternative mechanisms that may prove more relevant for more metals/catalysts. In this respect, this approach addresses the performance of an optimal WGS catalyst operating by the surface redox mechanism. The same methodology can then be implemented elsewhere as information about alternative WGS reaction mechanisms becomes available. Based on the redox model, it is investigated whether it is possible to describe the WGS activity of transition metals in general. In principle, this is done by assuming that the reaction mechanism is the same for all metals.

7.1.2 Estimating Parameter Changes

To extend the microkinetic model to describe the WGS activity of other transition metals besides Cu, it is necessary to reevaluate the parameters such as vibrational frequencies, adsorption energies[1], and activation energies of the rate-controlling steps.
The vibrational frequencies of the species on different metals may be found via vibrational spectroscopy methods such as electron energy loss spectroscopy (EELS) and infrared spectroscopy experiments, or they can be estimated through DFT-calculations. However, based on previous experience with the ammonia synthesis reaction [184], the changes in vibrational frequencies are neglected, as it is assumed that the vibrations are the same as they are on Cu. The adsorption energies for the adsorbed species are calculated from periodic, self-consistent density functional theory (DFT) calculations [185], whereas the activation energies are estimated with the Brøndsted-Evans-Polanyi (BEP) relation, see eq. 7.1. For an activated reaction the BEP relation involves a linear dependence between the activation energy, E_a, and the reaction energy, E_r [186, 187].

$$E_a = \alpha \cdot E_r + \beta \tag{7.1}$$

The reaction paths of two metals from reactants to products are shown in figure 7.1. The reactants level is defined as zero, and the activation, E_a, and reaction energies, E_r, for the different metals are identified.

[1]The correct term is ground-state energies [176, 177] of the surface intermediates, but this is not critical, as the relative change from one metal to another will be equivalent for ground-state and adsorption energies.

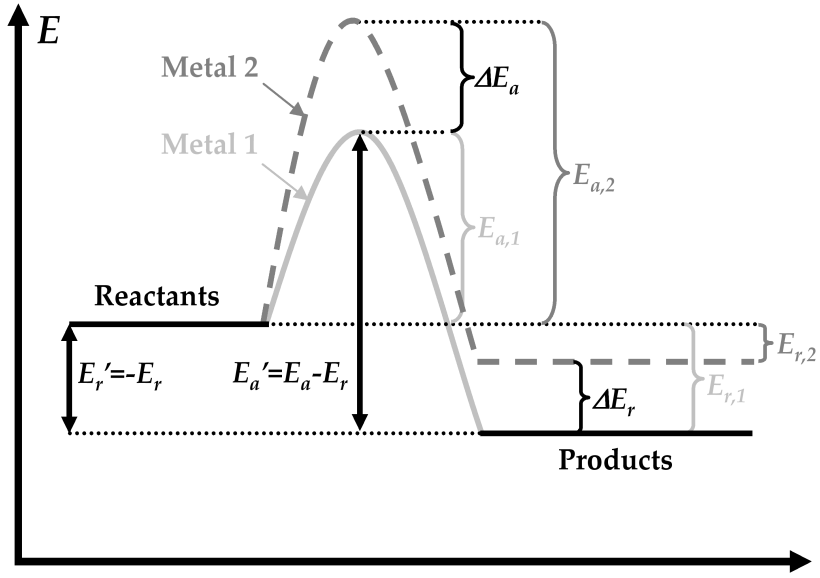

Figure 7.1: Energy diagram for an activated reaction on two different metals, 1 and 2. $E_{a,1}$ and $E_{a,2}$ are the activation energies on the respective metals, and ΔE_a is the difference. The same nomenclature is used for the reaction energy E_r. Energies marked with ($'$) are for the reverse reaction. From the figure it can be deduced that if $\Delta E_a = \alpha \Delta E_r$ then $\Delta E'_a = (1-\alpha)\Delta E'_r$.

The differences are defined as

$$\Delta E_a = E_{a,2} - E_{a,1} \tag{7.2}$$
$$\Delta E_r = E_{r,2} - E_{r,1} \tag{7.3}$$

The activation energy for the reverse reaction is

$$E'_{a,j} = E_{a,j} - E_{r,j} \quad j = 1,2 \tag{7.4}$$
$$\Updownarrow$$
$$\Delta E'_a = \Delta E_a - \Delta E_r \tag{7.5}$$

and the reaction energy is

$$E'_{r,j} = -E_{r,j} \quad j = 1,2 \tag{7.6}$$
$$\Updownarrow$$
$$\Delta E'_r = -\Delta E_r \tag{7.7}$$

Together with equation 7.1 the correlation between ΔE_a and ΔE_r becomes

$$\Delta E_a = \alpha \cdot \Delta E_r \tag{7.8}$$

When equations 7.5 and 7.7 are combined with 7.8, the correlation for the reverse reaction becomes:

$$\begin{aligned} \Delta E'_a &= \Delta E_a - \Delta E_r = (\alpha - 1)\Delta E_r \\ &= (1 - \alpha)\Delta E'_r \end{aligned} \tag{7.9}$$

Because the concern here is the changes in the activation energy, ΔE_a, which is encountered when switching to a metal other than Cu, the BEP relation is used in the form depicted in eq. 7.8 and 7.9, where α is the BEP correlation constant. Nørskov and coworkers [187] found that for the dissociation of N_2, CO, NO, and O_2 on close-packed surfaces, $\alpha = 0.90 \pm 0.04$, and for steps sites, $\alpha = 0.87 \pm 0.05$. For simplicity, a common value of $\alpha = 0.9$ is assumed for a reaction where bonds that does not involve hydrogen are broken. Equivalently, the correlation factor is 0.1 when such bonds are formed (elementary reaction step 7). The value $\alpha = 0.65$ estimated by Pallassana and Neurock [188] is used for reactions where bonds containing hydrogen are broken (elementary reaction steps 2 and 4).

The trends of the reaction energies for the rate-controlling steps and the adsorption energies of the seven adsorbed species can be estimated from data for molecular and dissociative chemisorption energies on the metals in question, which are obtained from DFT calculations. Two sets were used: one from Nørskov and co-workers [186] calculated with the RPBE functional for chemisorption of species on step sites, and one from Mavrikakis and co-workers[2] calculated with PW91 for chemisorption of species on close-packed surface terraces. In general, steps bind species stronger than do terraces, whereas PW91 overestimates binding compared with RPBE. It should therefore be acceptable to compare the results based on the two different data sets.

A total of ten parameters must be evaluated, namely the activation energies of the three rate-controlling steps and the adsorption energies of the seven adsorbed species, OH, H, O, CO, CO_2, H_2O, and HCOO. It is examined whether they can be correlated linearly, as the determination of the trends for the kinetic model is significantly simplified, when the number of independent parameters or descriptors, ΔE_x, is reduced. The general equations for the linear fits between the 10 activation and adsorption energies are given by eq. (7.10), where s_i is the slope of the fit.

$$\Delta E_{e,i} \approx s_i \cdot \Delta E_x \tag{7.10}$$

$$\Delta E_{a,i} = \alpha \cdot \Delta E_r \approx \alpha \cdot s_i \cdot \Delta E_x \tag{7.11}$$

[2] A. A. Gokhale, S. Kandoi, L. C. Grabow, J. A. Dumesic, M. Mavrikakis, unpublished observations.

The linear correlation between the reaction energies of the three rate controlling steps and the chemisorption energy for oxygen are shown in figure 7.2, and the correlation between the seven chemisorption energies and the chemisorption energy for oxygen are shown in figures 7.3 and 7.4. Figure 7.5, 7.6, and 7.7 display the corresponding correlations with the chemisorption energy for CO. From these figures it is clear that all of the energies correlate linearly with the chemisorption energy of either oxygen or CO. This behavior is illustrated in Table 7.1, where the deviation s from the linear fits obtained using the set from Mavrikakis and co-workers are given. s is calculated as

$$s = \sqrt{\frac{\sum_i (y_i - y_{r,i})^2}{n}} \tag{7.12}$$

where y_i is a value from the data set, $y_{r,i}$ is the corresponding value from the regression, and n is the number of values in the data set. Similar values are obtained for the fits based on the calculations from Nørskov and co-workers, except for rate-controlling step no. 4, the dissociation of hydroxyl, where oxygen is a better descriptor.

	E_{CO}	E_{O}
$E_{\mathrm{r},2}$ ($H_2O^* + * \rightarrow OH^* + H^*$)	0.446	**0.139**
$E_{\mathrm{r},4}$ ($OH^* + * \rightarrow O^* + H^*$)	**0.215**	0.322
$E_{\mathrm{r},7}$ ($CO^* + O^* \rightarrow CO_2^* + *$)	0.540	**0.446**
E_{CO} ($CO(g) + * \rightleftharpoons CO^*$)	**0**	0.450
E_{OH} ($OH(g) + * \rightleftharpoons OH^*$)	0.407	**0.174**
E_{H} ($\frac{1}{2}\,H_2(g) + * \rightleftharpoons H^*$)	**0.081**	0.172
E_{O} ($\frac{1}{2}\,O_2(g) + * \rightleftharpoons O^*$)	0.550	**0**
E_{HCOO} ($HCOO(g) + * \rightleftharpoons HCOO^*$)	0.304	**0.146**
$E_{\mathrm{CO_2}}$ ($CO_2(g) + * \rightleftharpoons CO_2^*$)	0.057	**0.055**
$E_{\mathrm{H_2O}}$ ($H_2O(g) + * \rightleftharpoons H_2O^*$)	**0.092**	0.101

Table 7.1: Comparison of deviation from the linear fits, s, of chemisorption and reaction energies vs. chemisorption energies for CO and O. Notice that the deviation factor for CO and oxygen naturally is zero. The bold values are the best correlations for E_{CO} and E_{O}. Chemisorption energies from Mavrikakis and co-workers for adsorption on terrace sites were used.

When the trends in the parameters are determined, the rate or turn-over frequency (TOF) can be found as a function of the ΔE_x's which have the best correlations to the other energies. This yields an $[N+1]$-dimensional volcano plot, where N is the number of descriptors needed. This type of correlation is a reflection of the principle of Sabatier which states that the optimal catalyst binds adsorbates moderately to the surface. With a too weak adsorption, the reaction rate will be low due to low coverage of reaction intermediates (and/or too low reactivity to activate some of the reactants like e.g. water). Conversely, it will be difficult to release reaction products into the gas phase with a too

strong adsorption, and the reaction rate will be low due to the lack of free adsorption sites on the surface [189].

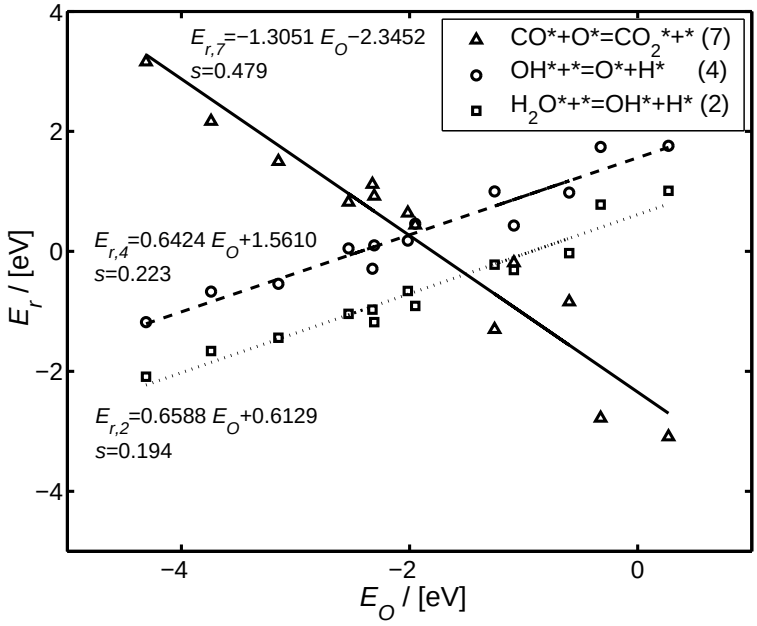

Figure 7.2: The linear correlations between the chemisorption energy for oxygen, E_O, and the reaction energies, E_r, of the rate determining steps from [186].

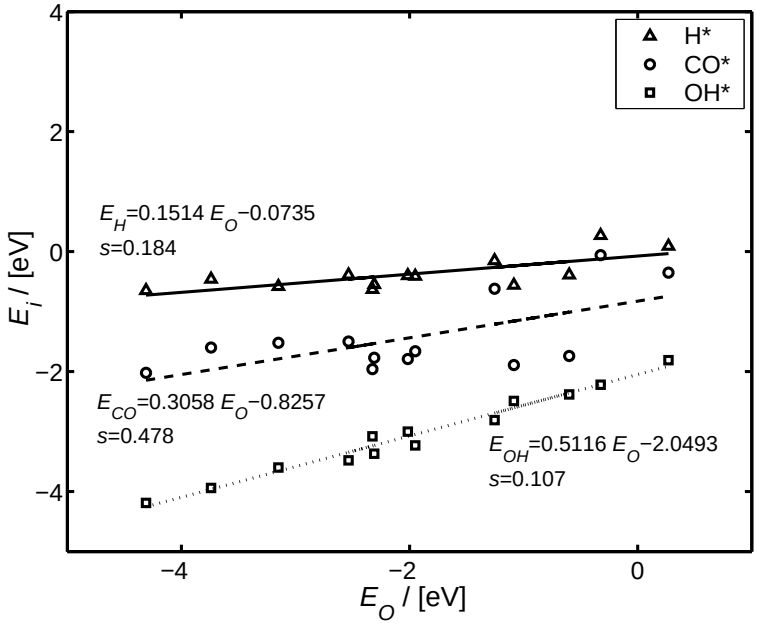

Figure 7.3: The correlations between the chemisorption energy for oxygen and the energies for OH, H, and CO. From [186].

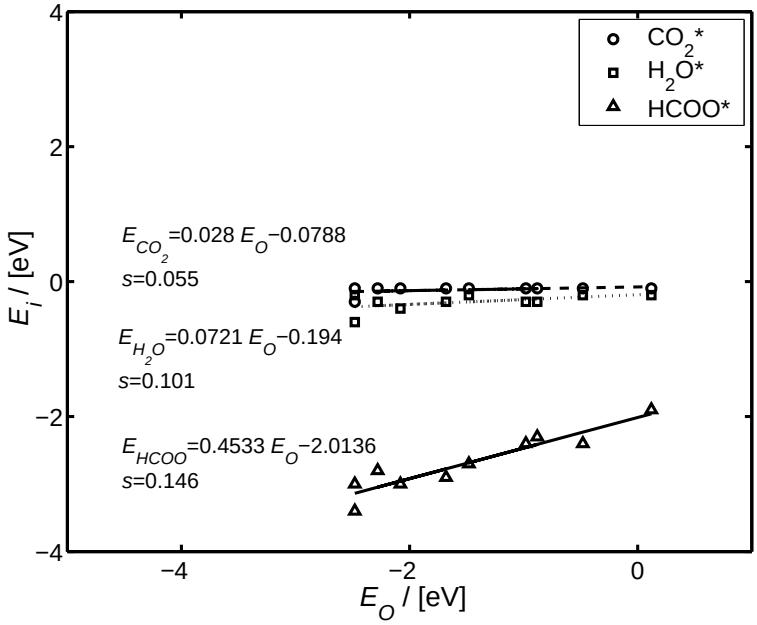

Figure 7.4: Correlations between the chemisorption energy for oxygen and the energies for HCOO, CO_2, and H_2O, PW91 data from Mavrikakis and co-workers.

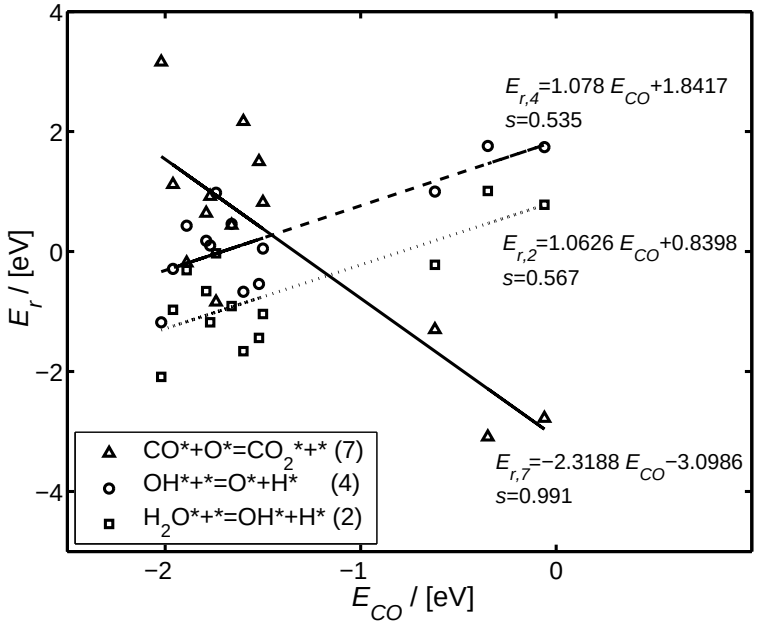

Figure 7.5: The linear correlations between the chemisorption energy for carbon monoxide, E_{CO}, and the reaction energies, E_r, of the rate determining steps. From [186].

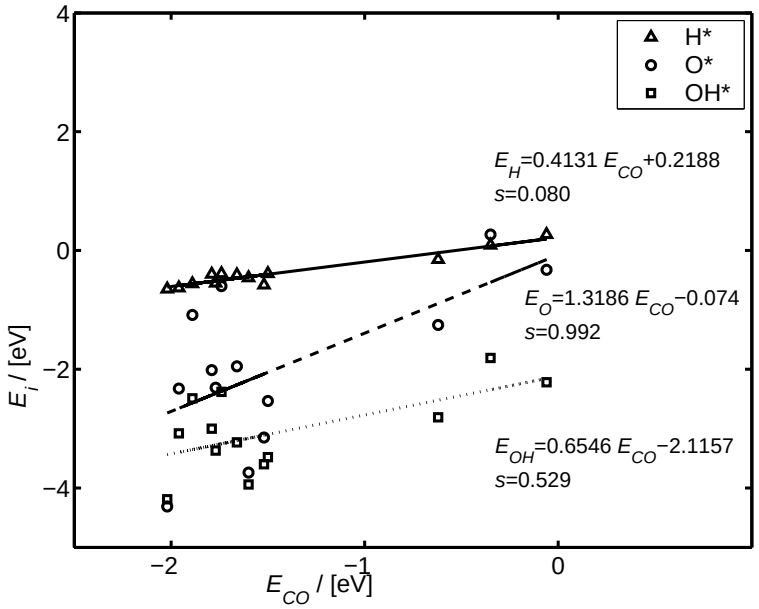

Figure 7.6: The correlations between the chemisorption energy for carbon monoxide and the energies for OH, H, and O. From [186].

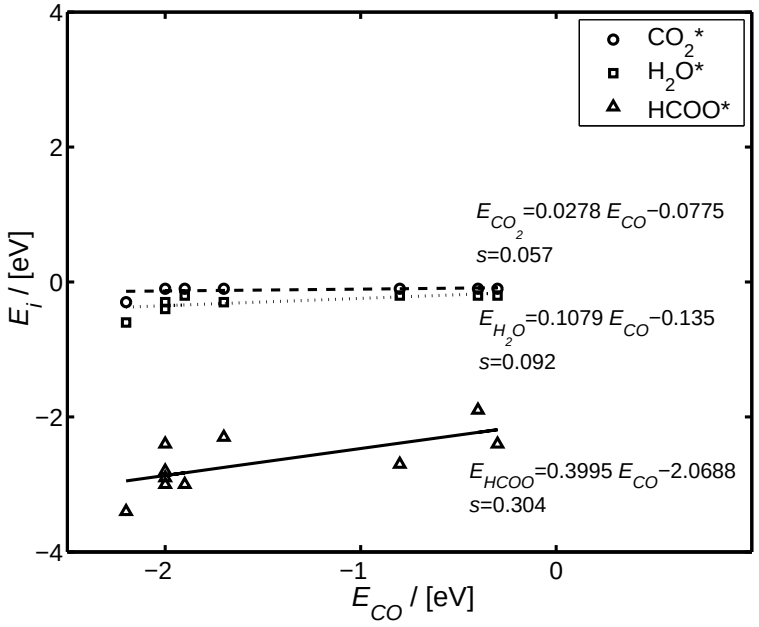

Figure 7.7: Correlations between the chemisorption energy for CO and the energies for HCOO, CO_2, and H_2O, PW91 data from Mavrikakis and co-workers.

7.1.3 Results and discussion

The water-gas shift reaction rate for multiple transition metal surfaces may now be described as a function of the binding energies of atomic oxygen and of carbon monoxide. A three-dimensional volcano plot based on chemisorption energies on terraces calculated by Mavrikakis and co-workers is shown in figure 7.8, and a closeup of the area around the maximum turnover frequency (TOF) is displayed in figure 7.9. Furthermore, an insert depicting the curve given by a cut through the maximum TOF and the TOF for Cu are shown. Note that the chemisorption energies for all metals are relative to the copper values (negative ΔE means stronger adsorption than on Cu). It is seen that the Cu coordinates are close to the coordinates for the maximum TOF, and that the optimal WGS catalyst is a metal that binds O and CO slightly stronger than Cu.

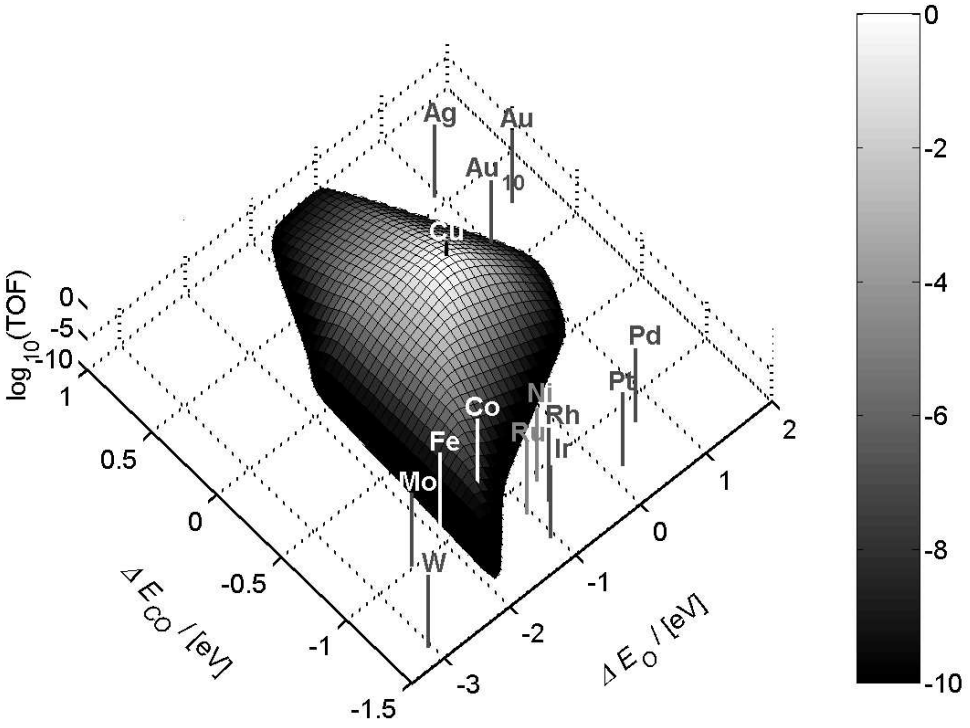

Figure 7.8: The turnover frequency of the WGS reaction at varying adsorption energies of carbon monoxide and oxygen is illustrated. Extent of reaction $\xi = 0$, $p = 30$ bar, $T = 225$°C, and the feed gas composition is 2.5% CO, 12.5% CO_2, 37.5% H_2, 25%, H_2O, and balance N_2. The two-dimensional volcano plot is based on chemisorption energies from Mavrikakis and co-workers for chemisorption on terrace sites.

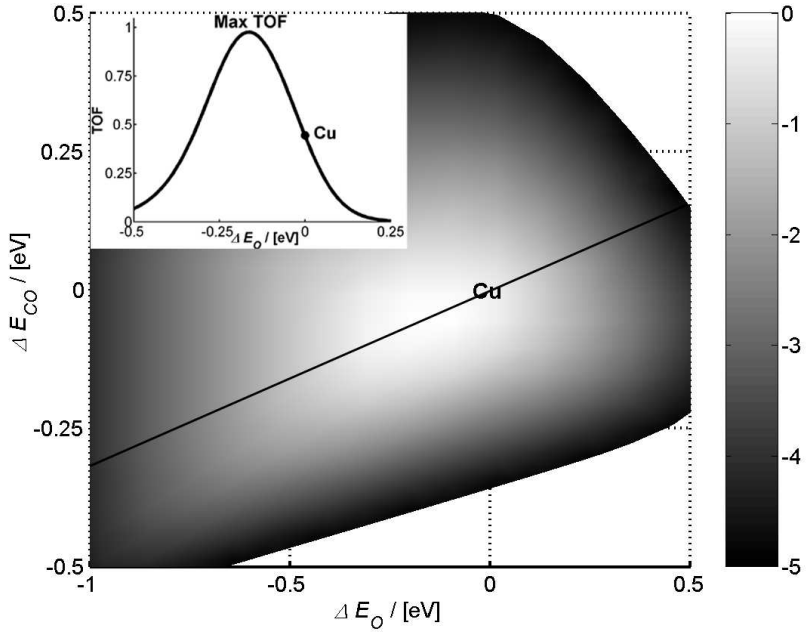

Figure 7.9: A close up of the maximum turnover frequency (TOF) at zero conversion, $p =$ 30 bar, $T = 225$ °C, and a feed gas composition of 2.5% CO, 12.5% CO_2, 37.5% H_2, 25%, H_2O, and balance N_2. Based on chemisorption energies from Mavrikakis and co-workers for chemisorption on terrace sites. Insert displays a cut through the maximum TOF and the TOF for Cu.

An analysis of the most abundant reaction intermediates (MARI) on the surface offers an explanation of the 3D volcano. The variation in surface coverages of the various intermediates when the adsorption energies of CO and O are changed relative to Cu are illustrated in figure 7.10 together with contour lines of the volcano.
It is seen that CO is the predominant surface intermediate at ΔE_{CO} below 0 eV. However, when ΔE_{O} becomes lower than -1 eV, oxygen begins to dominate the surface. Hydroxyl species are abundant and formate is adsorbed when $\Delta E_{\mathrm{O}} \in [-1; 0]$ eV, and $\Delta E_{\mathrm{CO}} \in [-0.5; 1]$ eV. A considerable coverage of surface hydrogen is present when ΔE_{O} ranges from 0 to 2 eV, and $\Delta E_{\mathrm{CO}} = 0$ eV. H_2O and CO_2 are present on the surface only when all other coverages are low and free sites are available. On the various metals, it is observed that Fe, Mo, and W are almost entirely covered with O probably forming stable oxides at the given reaction conditions, whereas Ni, Rh, Ru, Ir, Pd, and Pt are covered with CO. Cu, Au_{10}[3], Au, and Ag present only small coverages of both of these species.

[3]Binding energies from Lopez and Nørskov [190]

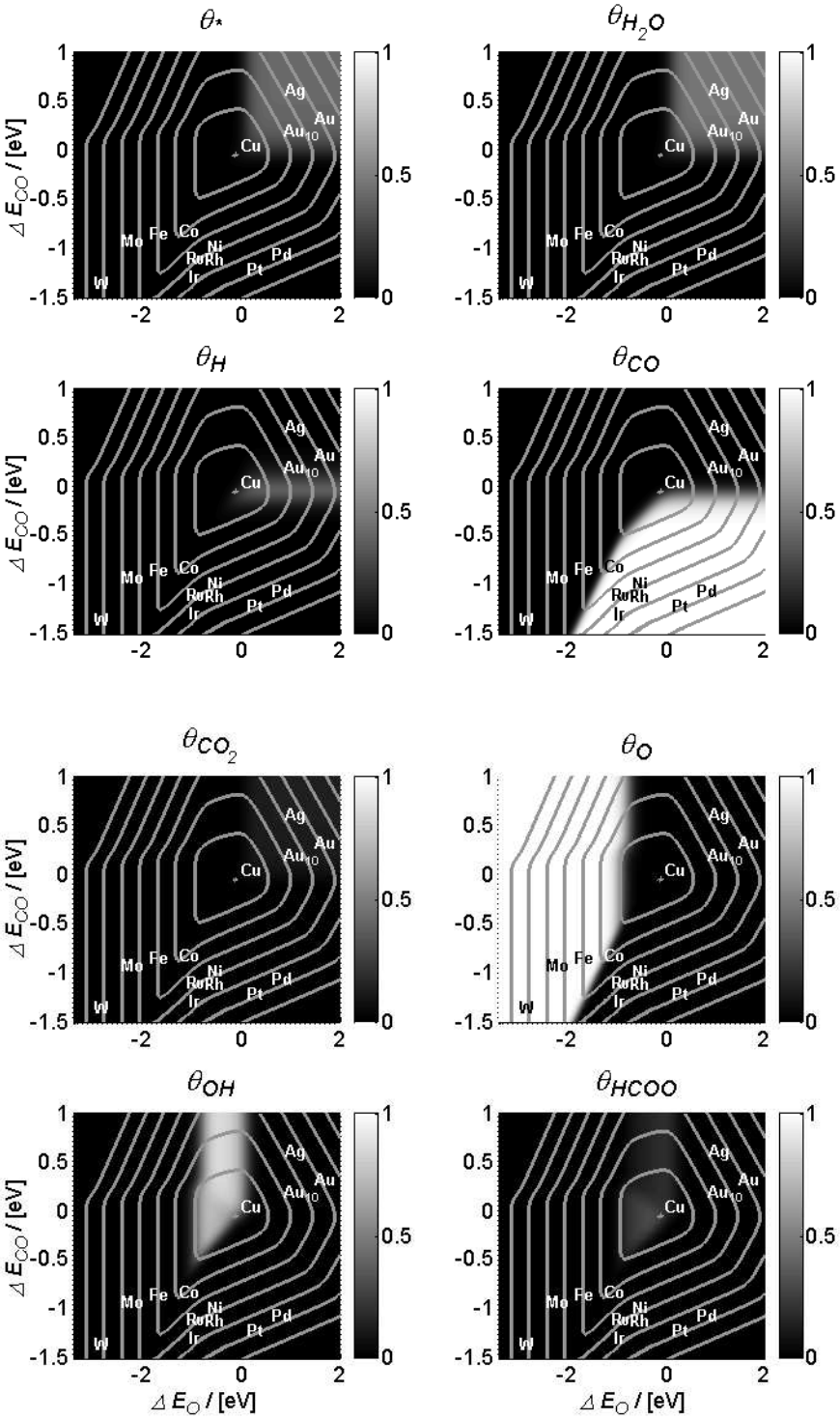

Figure 7.10: Surface coverage of the reaction intermediates at varying adsorption energies of carbon monoxide and oxygen relative to Cu (negative ΔE means more reactive than Cu). Contours corresponding to the turn-over frequency are superimposed. Extent of reaction $\xi = 0$, $p = 30$ bar, $T = 225$°C, and the feed gas composition is 2.5% CO, 12.5% CO_2, 37.5% H_2, 25%, H_2O, and balance N_2. Chemisorption energies from Nørskov and co-workers [186] for adsorption on step sites are used.

The position of the maximum of the volcano plot is sensitive to reaction conditions, as can be seen in figures 7.11 and 7.12. As a result, the optimal catalyst is not the same as the reaction proceeds and CO and H_2O are converted. Figure 7.11 shows that as conversion increases when passing through the reactor, the optimal catalyst changes to one that binds CO more strongly and O more weakly. The concept of an optimal catalyst curve has previously been introduced for ammonia synthesis [175]. Figure 7.12a illustrates how increasing pressure results in movement of the maximum turnover frequency toward higher ΔE_{CO} and ΔE_{O}, that is, toward weaker adsorption. At high pressure (20-40 bar) the predominant effect on the optimal TOF is caused by changing ΔE_{CO}, which may imply that at the position of the maximum TOF the CO coverage is high compared with that of oxygen. This behavior corresponds well with the findings in figure 7.10 for 30 bar. Increasing the temperature (see Fig. 7.12b) produces an effect that is the opposite of that produced by increasing the pressure. The reduction in coverage now has to be compensated for by a change in ΔE_{CO}. Again it is seen that the coverage of carbon monoxide is higher than that of oxygen in the region in question, and the effect of changing ΔE_{O} is small.

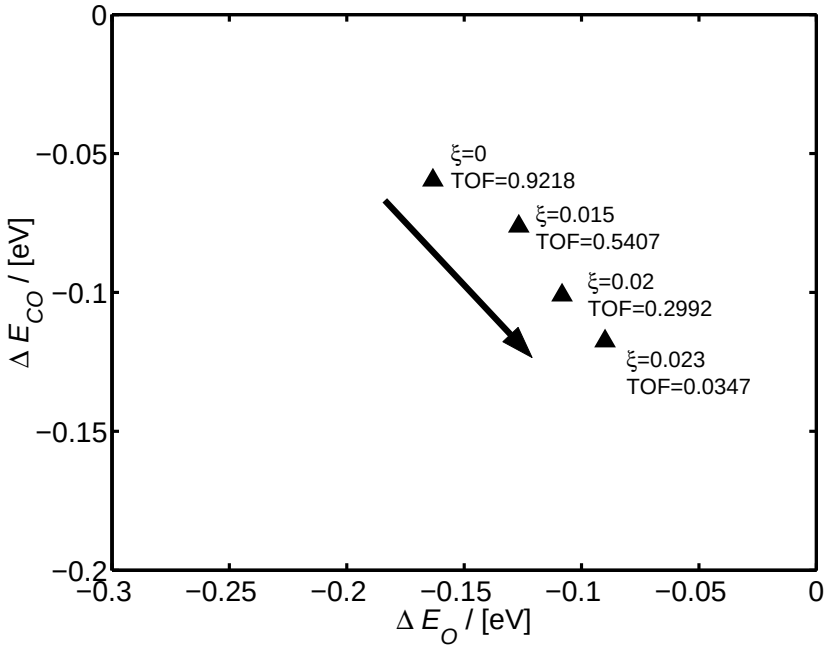

Figure 7.11: Coordinates (ΔE_{O},ΔE_{CO}) for the position of the maximum TOF at different extents of reaction ξ with $p = 30$ bar, $T = 225$ °C. Feed gas composition 2.5% CO, 12.5% CO_2, 37.5% H_2, 25% H_2O, balance N_2. The arrow indicates the shift in optimal adsorption energies, as the chosen variable increases. Based on the adsorption energies from [186].

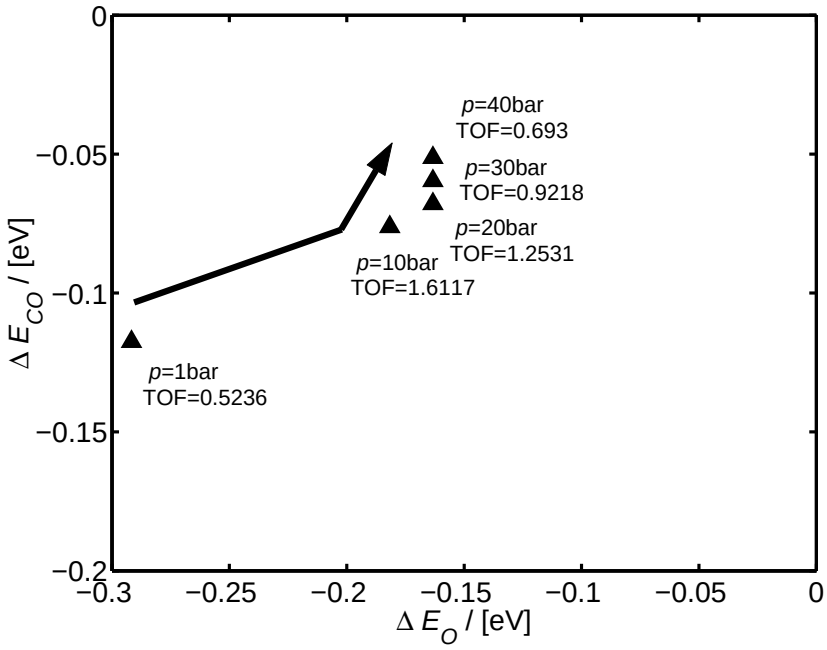

a)

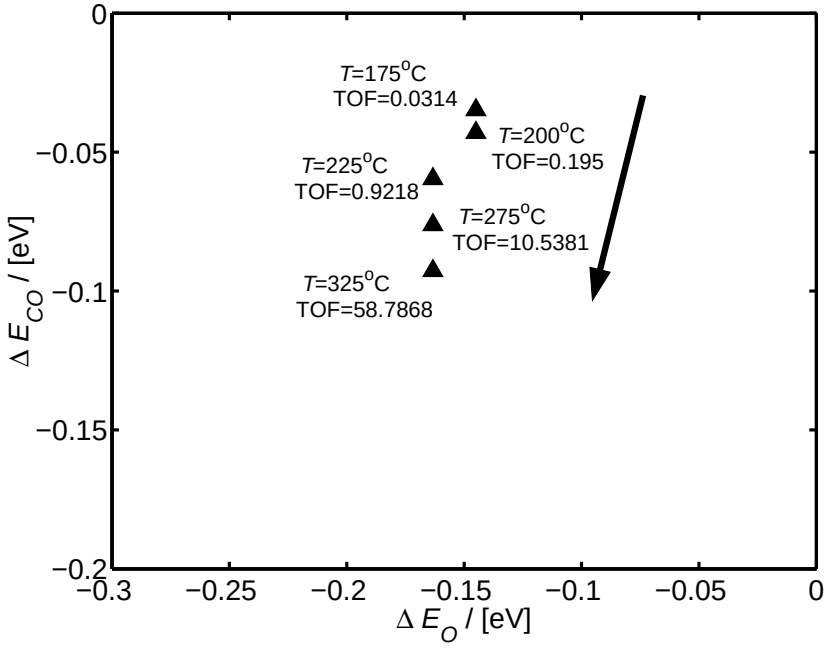

b)

Figure 7.12: Coordinates (ΔE_{O},ΔE_{CO}) for the position of the maximum TOF at (a) Varying pressures p with $\xi = 0$, $T = 225$ °C, and (b) varying temperatures T with $\xi = 0$, $p = 30$ bar. Feed gas composition 2.5% CO, 12.5% CO_2, 37.5% H_2, 25% H_2O, balance N_2. The arrow indicates the shift in optimal adsorption energies, as the chosen variable increases. Based on the adsorption energies from [186].

Basically the same results are obtained for the two DFT data sets. It is difficult to address whether the WGS reaction occurs on either steps or terraces, or to distinguish between the choice of DFT functionals. In addition, the reaction may be considerably more complex than suggested here. Different elementary steps of the reaction sequence may occur either solely on the terrace or at step sites, thereby involving the participation of two types of sites on the metal particles.
To limit the number of variables used to describe the activity trends, it is necessary to make several approximations, thereby limiting the validity of the model as one moves away from Cu. The impact of these assumptions have to be addressed. First of all, it was assumed that the reaction mechanism is the same on all metals. This may not be justified, since other reaction mechanisms may be suggested for the WGS reaction. Furthermore, the fact that the binding energies are coverage dependent is neglected. This is a particular problem at high coverages, which seems to be the case for the majority of the metals, see figure 7.10. This behavior is the most likely reason for the model to underestimate the reaction rate for a number of low-activity metals. Another source of uncertainties is the linear fitting of the chemisorption data, see table 7.1. Elementary step 7 in particular has large deviation values, and differences between the regression line and the individual data points can be substantial, see figure 7.2. This leads to the result that some of the metal parameters are reproduced quite well, whereas others are far from the linear estimate, leading to deviations in the reaction rate on a number of metals. As long as the model is used only in the vicinity of Cu, the error made in the estimates of the energies will be small, even though there are quite large uncertainties in the slopes, which are used to estimate the energies.

7.1.4 Improving the water-gas shift catalyst

As a consequence of the aforementioned limitations, the model is most reliable in the parameter space close to Cu. Because there are no other metals in the vicinity of Cu, the most important result of this study is that it gives an idea of what should be done to achieve an improved Cu catalyst. Even though Cu is placed near the maximum of the volcano plot, the WGS reaction rate on a Cu catalyst can be improved, if it is modified to bind both CO and O more strongly to the surface. According to the d-band model developed by Hammer and Nørskov [1], an enhancement of the reactivity of copper may be obtained by growing it as a pseudomorphic layer on top of another metal with a larger lattice constant [191, 192]. Here it is important that Cu does not dissolve into the bulk of the host metal, but rather forms islands on the surface of the host metal [193], a property that Cu deposited on Pt possesses [96]. It can be questioned whether this approach is favorable, as it is seen in figure 7.9 that the predicted activity can only be improved by approximately a factor of 2. Alloying may also enhance the activity of the catalyst, but this effect has not been fully clarified in the case of the methanol catalyst, where, for example, Zn may improve the overall rate [194, 195, 42]. Improvement in catalyst performance in this case is probably related to the well-known sintering of copper catalysts [9].

7.1.5 May WGS be modeled with one descriptor?

To achieve a simpler description of the WGS reaction it was examined, whether the volcano could be described using just one energy parameter. This parameter, E_{red}, should be a simple function of the adsorption energies for atomic oxygen and carbon monoxide for it to have any physical meaning. Equations 7.13 and 7.14 were used to describe E_{red}. An angle θ, and a parameter γ were then both varied to achieve the best possible fit. Ranges used were $\theta \in [0° : 180°]$ and $\gamma \in [0 : 20]$.

$$E_{red} = |E_{CO}\cos(\theta) - E_O\sin(\theta)| + \gamma \cdot |E_{CO}\sin(\theta) + E_O\cos(\theta)| \quad (7.13)$$

$$E_{red} = (E_{CO}\cos(\theta) - E_O\sin(\theta))^2 + \gamma \cdot (E_{CO}\sin(\theta) + E_O\cos(\theta))^2 \quad (7.14)$$

A first order linear regression between E_{red} and $\log_{10}(\text{TOF})$ using least squares were applied to both functions in addition to a second order regression to equation 7.14. The maximum of the volcano was chosen as the origo for the fits, and the data points to which the fit was made were limited to a distance max. 1 eV away from the maximum turn-over frequency. The curves corresponding to the best fits obtained for the two equations are given in figures 7.13, 7.14, and 7.15. All a) panels show the logarithm of the turn-over frequency versus the reduced energy parameter. The series of data points are plotted together with the line describing the fit. The b) panels depict the contour of the original volcano together with the ones resulting from the corresponding fit. No particular good description was obtained for any of the equations all though the function in eq. 7.14 yielded slightly better results. The second order fit provided the best description with an R^2 around 0.888, but it was not significantly better than the linear fit with $R^2 = 0.881$. Eq. 7.13 resulted in the lowest value with $R^2 = 0.847$. It should be noted that multiple combinations of γ and θ resulted in fits of equal quality.

No fairly simple relation may be employed to reduce the number of descriptors to one parameter. An explanation for this is offered by the asymmetric shape of the iso-rate curves diplayed in the E_O, E_{CO} coordinate system in figure 7.13b. Furthermore, the fit made here will deviate when the pressure, temperature, or gas composition is changed, which in it self poses a problem.

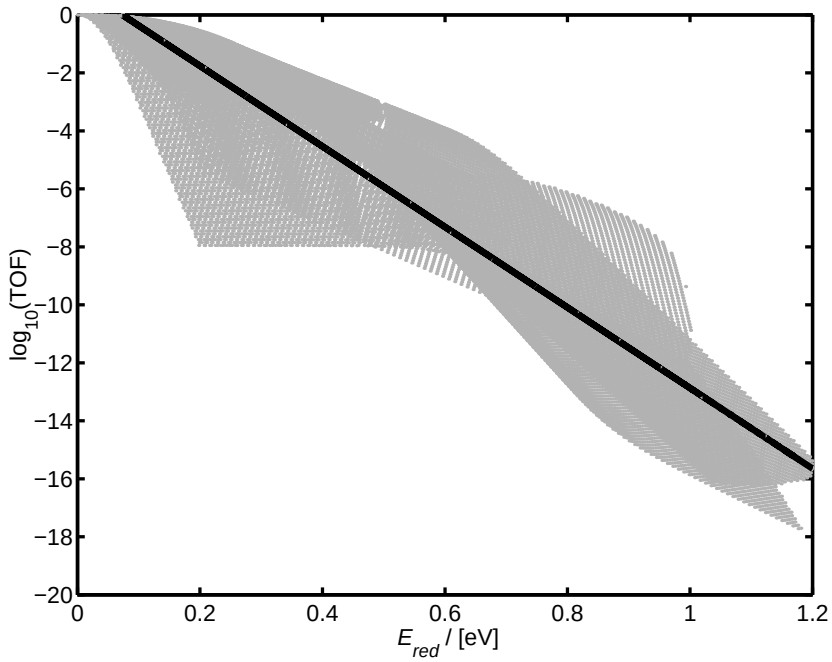

a)

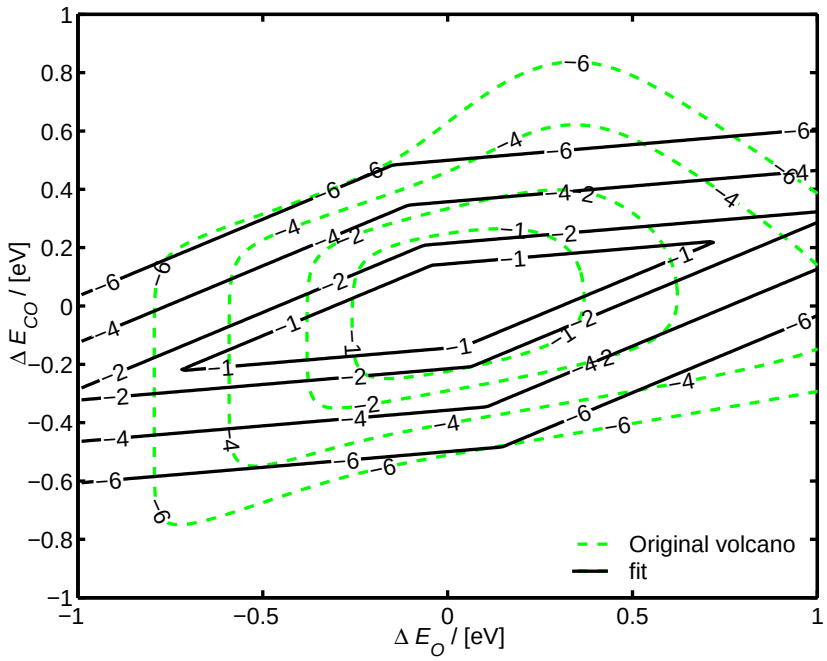

b)

Figure 7.13: First order fit using eq. 7.13. Best fit was achieved for $\gamma = 0.191$, $\theta = 141.7°$ with $R^2 = 0.847$. a) $\log_{10}$(TOF) versus E_{red}. The data points and the linear fit are shown. b) Original volcano contour together with the fit contours in (E_O,E_{CO}) coordinates. Conditions used to calculate the TOF were $p = 1.02$ bar and $T = 270$ °C. The feed gas composition was 0.15 bar CO, 0.01 bar CO_2, 0.01 bar H_2, 0.15 bar H_2O, and 0.7 bar Ar.

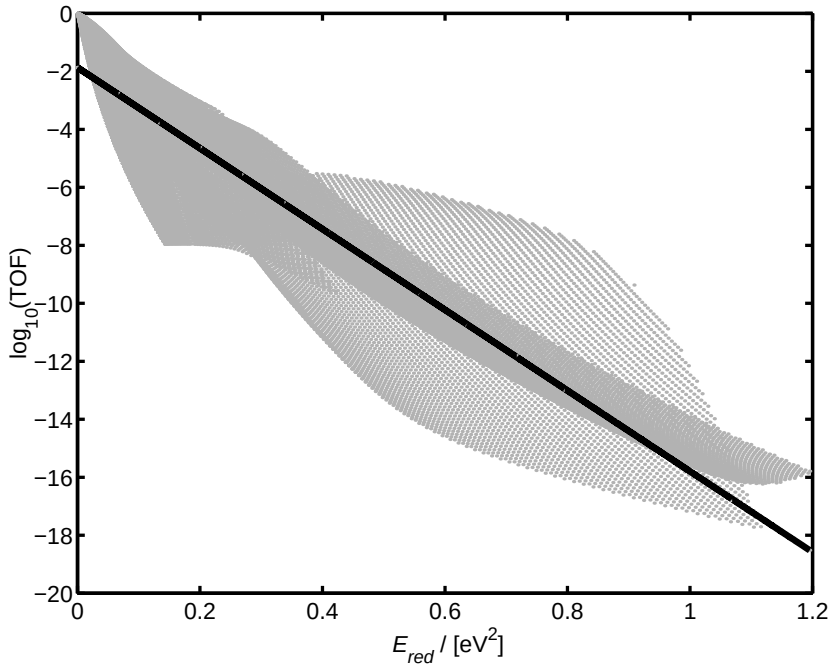

a)

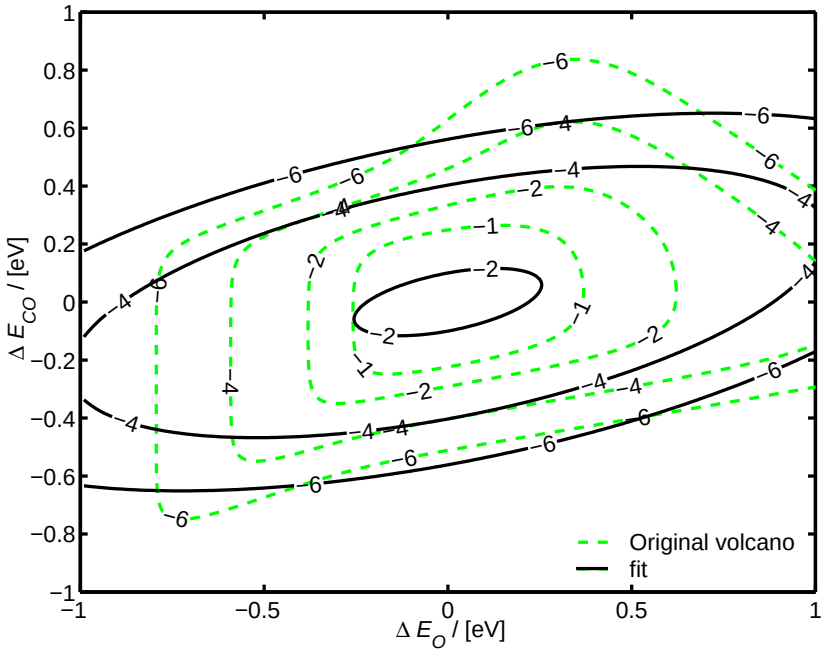

b)

Figure 7.14: First order fit using eq. 7.14. Best fit was achieved for $\gamma = 0.136$, $\theta = 44.2°$ with $R^2 = 0.881$. a) $\log_{10}$(TOF) versus E_{red}. The data points and the linear fit are shown. b) Original volcano contour together with the fit contours in (E_O,E_{CO}) coordinates. Conditions used to calculate the TOF were $p = 1.02$ bar and $T = 270$ °C. The feed gas composition was 0.15 bar CO, 0.01 bar CO_2, 0.01 bar H_2, 0.15 bar H_2O, and 0.7 bar Ar.

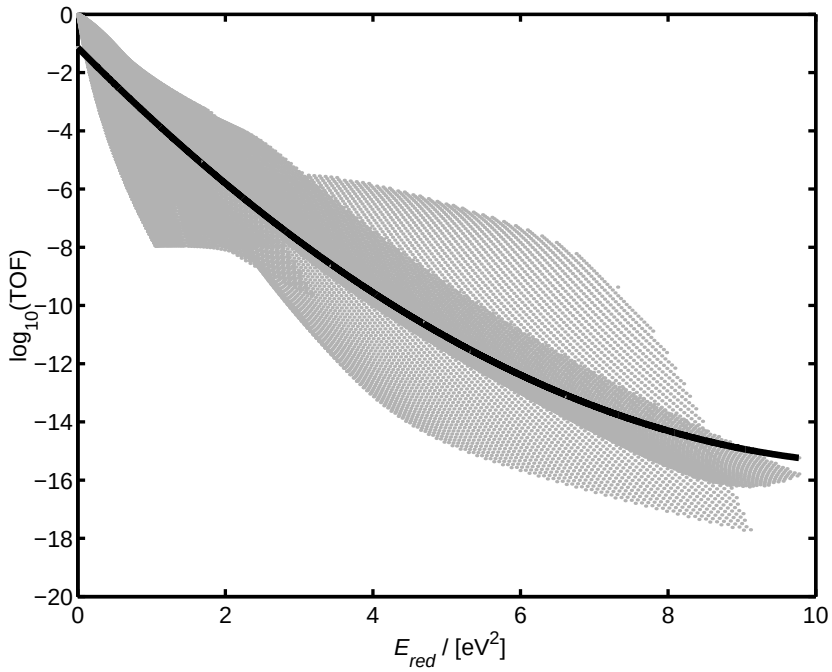

a)

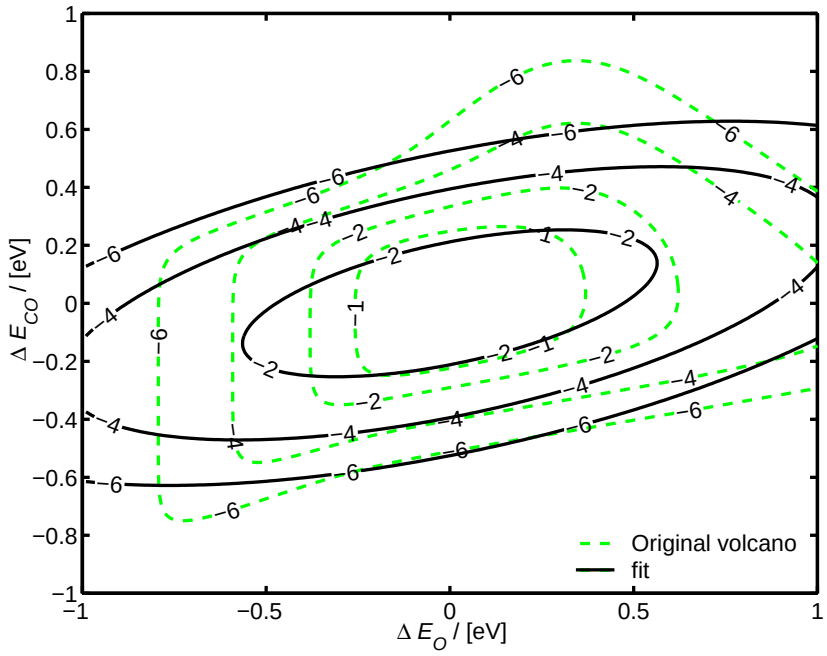

b)

Figure 7.15: Second order fit using eq. 7.14. Best fit was achieved for $\gamma = 8.105$, $\theta = 36.4°$ with $R^2 = 0.888$. a) $\log_{10}$(TOF) versus E_{red}. The data points and the linear fit are shown. b) Original volcano contour together with the fit contours in (E_O,E_{CO}) coordinates. Conditions used to calculate the TOF were $p = 1.02$ bar and $T = 270$ °C. The feed gas composition was 0.15 bar CO, 0.01 bar CO_2, 0.01 bar H_2, 0.15 bar H_2O, and 0.7 bar Ar.

7.2 Water-gas shift experiments

WGS catalysts based on iron oxide, chromium oxide, and copper are as previously mentioned primarily used in industry. During the last three decades a great variety of metals, supports and dopants have been examined in order to achieve high activity and selectivity toward the WGS reaction thus avoiding unwanted reactions like methanation. Stability and poison tolerance are also required, as species like sulfur and halides may be present in the feed, and elevated temperatures may lead to sintering of the metal particles.

As the WGS model only deals with the relative activity of transition metal surfaces, and support effects are neglected, the results from the model must be compared to studies of several metals on fairly inert supports like alumina, silica, or magnesia. Studies which cover a wide range of metals were done by Grenoble et al. [196] and Boisen et al. [173].

7.2.1 Grenoble et al.

Grenoble et al. [196] examined several Al_2O_3-supported transition metals. The catalysts were prepared by impregnating the alumina with aqueous solutions of different salts. The catalysts were reduced in H_2 for 1 hr at 500 °C except for Cu and Au, where 250 °C was used, and the fraction exposed was then measured using CO and H_2 chemisorption uptake and X-ray diffraction. The experiments were carried out with varying reaction temperature to maintain a CO conversion of less than 5% thus avoiding heat and mass transfer effects. It was reported that a volcano-shaped curve was obtained when the water-gas shift activity of alumina supported metal catalysts was plotted against the strength of interaction of molecular CO on the metal. At 300 °C, with partial pressures $p_{CO} = 0.243$ bar and $p_{H_2O} = 0.314$ bar, the turn-over frequency (TOF) for the WGS reaction decreased in the order:

$$\text{Cu} > \text{Re} > \text{Co} > \text{Ru} > \text{Ni} > \text{Pt} > \text{Os} > \text{Au} > \text{Fe} > \text{Pd} > \text{Rh} > \text{Ir}$$

The alumina is not completely inactive for WGS, but compared to ceria [197], this is negligible.
When the model is used to estimate the trends in catalytic WGS activity for various transition metals, it is clear that the model is not quantitatively reliable for metals other than Cu. If the predicted rates are compared with the rates measured by Grenoble et al. [196], one finds that, for all metals other than Cu, the predicted rate is several orders of magnitude lower than the measured rate. However, the model reproduces the trends found experimentally by Grenoble et al. surprisingly well.
The estimated WGS activity order for transition metals based on chemisorption on step sites [186] is at low conversion[4] predicted to be:

[4] As Grenoble et al. found the TOF for conversions below 5%, the best conditions for examining the model estimates should be initial rates for a given gas mixture.

$$\text{Cu} > \text{Co} > \text{Ru} > \text{Fe} > \text{Ni} > \text{Rh} > \text{Au} > \text{Ir} > \text{Pd} > \text{Pt}$$

From the chemisorption energies on terraces by Mavrikakis and co-workers, the order of activity is predicted to be:

$$\text{Cu} > \text{Ni} > \text{Pt} > \text{Rh} > \text{Ru} > \text{Au} > \text{Ir} > \text{Pd}$$

From the chemisorption data of Nørskov and co-workers [186], it is seen that the model overestimates the rates for Fe and Rh, whereas the rate over Pt is underestimated, and the rates over the rest of the metals are placed fairly well. When the data from Mavrikakis and co-workers are used, the rate over Rh is overestimated, the rate over Ru is underestimated, but the representation of Pt is good. Iron will most likely be present as an oxide under WGS conditions, which has not been taken into consideration in the present model, and therefore the estimated reaction rate on Fe will be misleading. Regarding Pt, the model predicts that it is essentially WGS inactive, but it is found experimentally to be quite active. This metal seems to be highly poisoned by adsorbed carbon monoxide, see figure 7.10, however, the CO chemisorption energy depends on CO coverage [198, 199], a fact that has not been incorporated into the model. As already discussed, a similar coverage effect may also influence a number of other metals, particularly those where the surface coverage is predicted to be close to unity. Because there are no extensive data on this coverage dependence, it was decided not to include it. Using the data on steps from Nørskov and co-workers [186], a better description of the experimental metal-activity ranking is generally obtained than when the data on terraces from Mavrikakis and co-workers is used. Of course, a complete fit cannot be expected, because other mechanisms may dominate on metals different from copper. For example, spillover of oxygen or hydroxide from the support to the metal particles may also occur, leading to a rate higher than the one estimated here. This is the case, for example, for Au, which becomes a good WGS catalyst when supported on Fe_2O_3, TiO_2, and CeO_2 [200, 201, 202]. Finally, there may be undesirable reactions, like the methanation process, which takes place on Ru and Rh [203]. The latter reaction is not a problem for Cu, as it is inactive for methane formation. Nonetheless, it is remarkable that this simplified model can account for so many of the trends.

7.2.2 Boisen et al.

In connection with the limited literature on the subject, activity measurements for twelve transition metals (Fe, Co, Ni, Cu, Ru, Rh, Pd, Ag, Re, Ir, Pt, and Au) supported on inert $MgAl_2O_4$ were performed at Haldor Tøpsoe A/S by Astrid Boisen, Ton Jannsens, and Søren Dahl, as presented in [173]. In order to evaluate the influence of a redox-active support, $Ce_{0.75}Zr_{0.25}O_2$ was also investigated. The fabrication and characterization of the different catalysts, as well as the results on the $Ce_{0.75}Zr_{0.25}O_2$ support are all given in detail in [173].

The most active inert support catalyst is $Cu/MgAl_2O_4$ with a H_2O conversion of 9.8% at a temperature[5] of 270 °C and a space time of $W/F = 1779$ g·s/mol. Conditions were $p = 1.02$ bar and $T = 270$ °C. The feed gas composition was 0.15 bar CO, 0.01 bar CO_2, 0.01 bar H_2, 0.15 bar H_2O, and 0.7 bar Ar. At these conditions the measured activities follow the order

$$Cu > Pt > Rh > Pd > Re > Ni > Au > Ru \approx Co \approx Ag > Ir \approx Fe$$

Cu is five times more active than Pt, 15 times more than Rh, and 300 times more active than Fe and Ir. Interestingly, Co and Ru are not found to be very active, whereas the activity on Rh and Pd is high in the present work, when compared to the results from Grenoble et al. [196].

The model predicts for the same reaction conditions and feed gas composition the order depicted below.

$$Cu > Co > Fe > Ru > Ag > Ni > Au > Rh > Ir > Mo > Pd > Pt$$

For Mavrikakis and co-workers the following order is obtained:

$$Cu > Co > Ag > Ni > Pt > Rh > Au > Ru > Ir > Pd$$

Again, especially Pt and Pd is underrated, which may be explained by the shortcomings mentioned in the previous section.

The metal activity order is very different when using the redox active $Ce_{0.75}Zr_{0.25}O_2$ support. The platinum catalyst displays the highest activity with a H_2O conversion of 22.1% at 270 °C and a space time of $W/F = 1962$ g·s/mol. At these conditions the activity follows the order

$$Pt > Re > Rh \approx Pd > Ru > Ni > Ir \approx Co > Cu > Ag > Fe > Au$$

where Pt is approximately three times more active than Re, 4-5 times more active than Rh and Pd, and roughly 500 times more active than Au. Only the Cu and Au catalysts are more active on the $MgAl_2O_4$ support, compared to $Ce_{0.75}Zr_{0.25}O_2$.

In order to examine the model predictions, the experimental activities were evaluated with respect to the adsorption energies for carbon monoxide and oxygen using the DFT calculations for step sites on the pure metals obtained from [186]. These seem the most relevant ones as it minimizes the influence of the crystal structure of the metal, since the step sites are more alike than the low index planes in the different crystal structures. Secondly,

[5]It was chosen to report the rate constants at 270 °C, because at higher temperature conversions above 40% are measured for the most active catalysts, and at lower temperatures the least active catalysts give very low conversion.

as step sites are generally more reactive [187], it is likely that the difficult water dissociation occurs on these sites or similar sites, rather than on the close packed crystal facets.

The relation of the activities with the binding energies requires that the active components in the catalysts is in a metallic state. When assessing the thermodynamic driving force for oxidation, it is found that only Fe forms a stable bulk oxide in the equilibrated WGS gas at the relevant temperatures. The measured WGS activity on the Fe catalysts is possibly due to the activity of Fe oxide, and it is thus omitted in the plots as the binding energy of CO and O on metallic Fe is not relevant. Furthermore, Re is omitted because data for CO and O on this metal is not available.

The activity of the $MgAl_2O_4$ supported catalysts as a function of the adsorption energies for carbon monoxide and oxygen are displayed in figure 7.16 a and b, respectively. When examining panel a) it is not obvious that the use of E_{CO} as a descriptor results in a volcano type relationship, as none of the metals result in a clear maximum. Grenoble et al. [196] who obtained a good correlation found a high turn-over frequency on Cu relative to the other metals. This was not found to the same extent here.
In figure 7.16b a clearer volcano-shaped curve is obtained with E_O as a descriptor. However, one also has to take into account the division of the metals into a group with a weak CO adsorption (Cu, Ag, Au) where the reaction is not inhibited by a high CO coverage, and a group with a strong CO adsorption. This is depicted in figure 7.17 where the calculated CO coverage as a function of E_O and E_{CO} at approximately the reactions conditions used is shown.
A trend-line, see figure 7.16b, for the weak CO adsorption group Cu, Ag, and Au indicates that improved activity could be obtained, if Cu were made more active with respect to the adsorption of atomic oxygen (i. e. water activation). This agrees well with the conclusion reached on the basis of the microkinetic model, namely that a more active WGS catalyst could be obtained by making Cu more reactive [56]. A firm conclusion can, however, not be made as there are only three data points available.

The volcano drawn for the group with a strong CO adsorption suggests that an activity maximum may be found around Pt or Pd. This observation, combined with the Sabatier principle and the high CO coverage in this region, suggest that metals that bind atomic oxygen stronger than Pt is limited in activity by a slow release of reaction intermediates that have an adsorption energy correlated with E_O (e.g., O* or OH*), whereas the activity of metals that binds O less strong is limited by slow water activation. Interestingly, when combining the data for all metals it seems that Cu is more active than all metals with strong CO adsorption when an inert support is used. This suggests that metals with a low CO binding energy are preferred when applying inert supports. Assuming that the interpolation principle can be used to assess the adsorption energies of alloys, a possible candidate would be a CuNi alloy, since the oxygen adsorption then is strengthened compared to pure Cu without increasing the CO adsorption energy too much. However, Ni is also a very good methanation catalyst, which is an unwanted side reaction in the

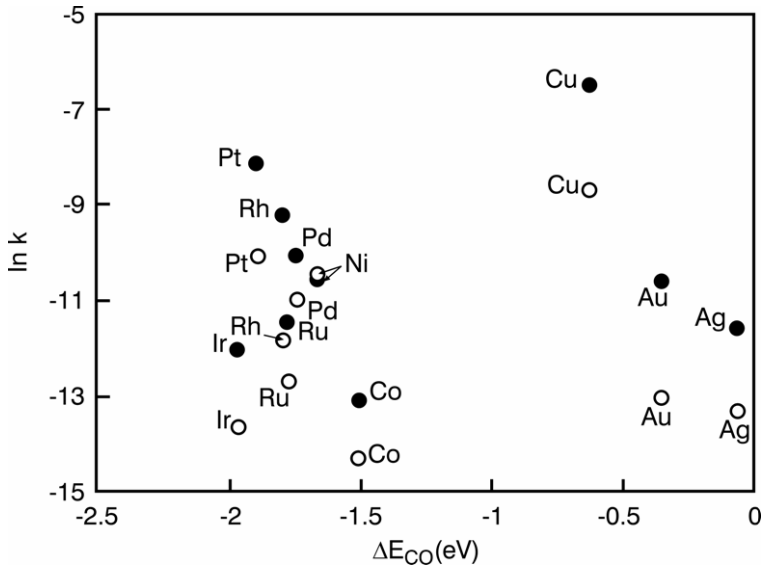

a)

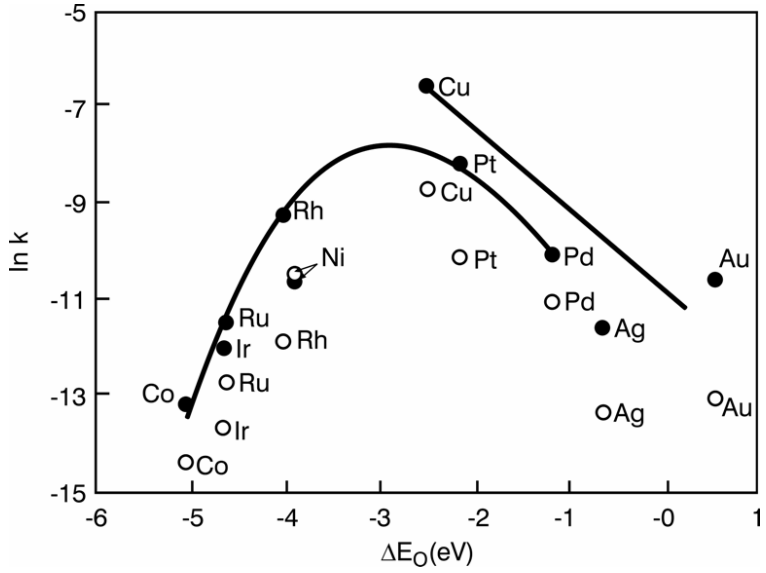

b)

Figure 7.16: The natural logarithm of the rate constant, k, for the $MgAl_2O_4$-supported catalysts at 270 °C plotted against the adsorption energy of carbon monoxide, E_{CO} (top panel) and atomic oxygen, E_O (bottom panel). Black circles symbolize the rate constant mol/(μmol metal·s·bar^2). Open circles symbolize the rate constant mol/(m^2 metal surface·s·bar^2). In the bottom panel two lines have been put in to guide the eye

WGS process, and CO is known to be able to pull Ni to the surface of Cu [204]. Another possibility is CuPt alloys where the composition should be appropriate to keep the CO adsorption energy low enough on the active sites. CuPt has recently been suggested as a good WGS catalyst by Knudsen et al. [108]. The same components could also be combined to form pseudomorphic layers of Cu on top of Pt, thus increasing both the O

and CO adsorption energy. Based on the present experimental results for the water-gas shift reaction, the increase in the latter may however pose a problem.

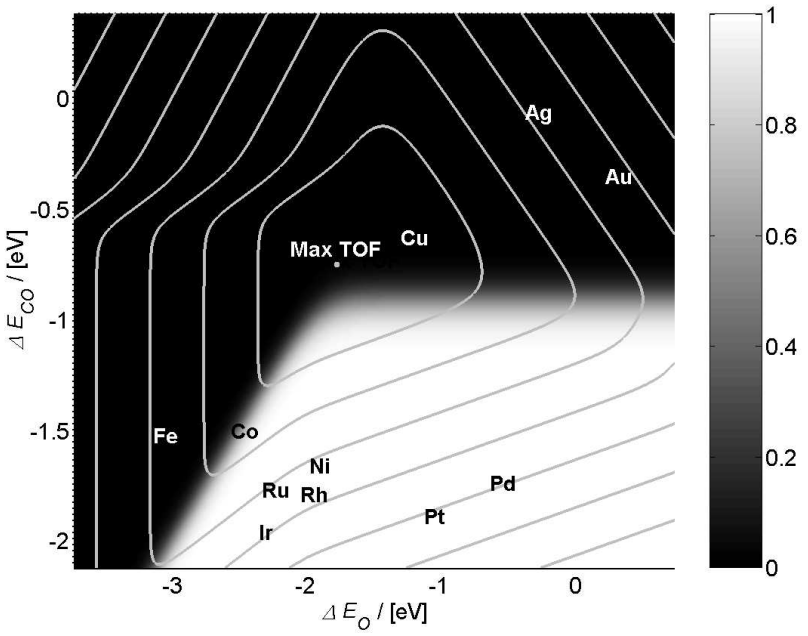

Figure 7.17: Surface coverage of carbon monoxide at varying adsorption energies of oxygen and carbon monoxide relative to values for Cu as predicted by the kinetic model that describe the water-gas shift reaction over transition metals. The turn-over frequencies are superimposed as contour lines and the corresponding energy coordinates for the included metals are marked. Each contour line marks a drop in rate corresponding to four orders of magnitude. Notice that the coordinates are absolute. Conditions are $p = 1.02$ bar and $T = 270$ °C. The feed gas composition is 0.15 bar CO, 0.01 bar CO_2, 0.01 bar H_2, 0.15 bar H_2O, and 0.7 bar Ar.

It is noted that the iso-rate curves in figure 7.17 predict that the WGS activity of the metals with strong CO adsorption should not have a peak around Pt on the E_O axis as observed experimentally, see figure 7.16b, indicating that the assumptions in the model, which are valid for Cu, do not apply to all metals. Since the redox reaction mechanism could be used to model the WGS reaction over a Pt/Al_2O_3 if a coverage dependent CO adsorption energy was included [205], the omitted coverage dependence is a likely contributor to the failure of the model.

7.3 Conlusions

Trends for the catalytic activity of the WGS reaction on various transition metals have been studied by estimation of the reaction rate with the use of a microkinetic model, which assumes that a simple surface redox mechanism is dominant over all metal catalysts.

By comparing the DFT-derived binding energies for all involved surface intermediates and activation energies for the rate-controlling steps, a strong linear correlation between most of the parameters was found, and the initial ten model parameters could be reduced to two descriptors, namely the binding energies of carbon monoxide and oxygen. It was sought to reduce the number of descriptors to one reduced energy parameter by employing a relationship between the binding energies of atomic oxygen and carbon monoxide. The behavior of the reaction rate is, however, too complicated to be described in a simple way using a single descriptor.

A surprisingly good qualitative estimation of the relative activity order of the different transition metal catalysts was found. However, the model fails to quantitatively reproduce experimental data over such a broad range of metals. This discrepancy can be explained, to some extent, by the fact that the coverage dependence of all binding energies except formate have been neglected in the model.
Copper is found to be close to the optimum of the rate calculation, although there is room for improvement. In the vicinity of copper the model is expected to describe the catalyst performance well, and it thus predicts that the activity of the copper-based WGS catalyst may be improved by an increase in the reactivity toward carbon monoxide and oxygen. This conclusion was not obvious prior to the present investigation. Furthermore, this study suggests possible directions for improving the WGS catalyst. It is noted here that one cannot exclude the possibility that another improved WGS catalyst may be found, which operates through a reaction mechanism different from the simple redox mechanism used to estimate trends in the present study.
Water-gas shift activity measurements for several transition metals were correlated to the binding energies of atomic oxygen and carbon monoxide to elucidate the modeling results. It was found that the metals could be divided into two groups with a weak and a strong CO interaction, respectively. Further improvement of the water-gas shift activity may according to the experimental results be obtained by modifying Cu such that the binding energy of oxygen is increased, and the CO adsorption remains unaffected.

Chapter 8

Conclusions and outlook

8.1 Overall conclusion

The presented work has combined computational and experimental approaches to gain a better understanding of the reactivity changes caused by the modification of copper surfaces as well as the interaction of CO_2 and H_2.
Regarding the bimetallic model system, it has been found that deposition of Cu on a Pt(111) crystal at a substrate temperature of 425 K results in the onset of second overlayer growth around 0.6 ML Cu. Surface alloy formation is found to start at approximately 460 K, which is low compared to other investigations in the literature.
Furthermore, evidence has been presented for the dissociative adsorption of CO_2 and subsequent formation of a stable carbonate species (CO_3) when subjecting the Cu/Pt(111) sample to high pressures of CO_2 at room temperature. PM-IRRAS and EELS spectra show that the intensities of the observed vibrational modes of carbonate are pressure dependent. This is interpreted as a shift in the geometry of the carbonate compared to the sample. The modes are consistent with a molecule configuration which is lying nearly flat on the surface in UHV and is slightly raised under high pressure.
DFT calculations present steps and defects as the likely sites for carbonate adsorption with a 0.5-0.7 eV larger binding energy than observed on terraces. Frequencies calculated for carbonate on stepped slabs are moreover close to those observed experimentally.
Decomposition of the carbonate is seen in a wide temperature range in TPD spectra with the main peak around 450 K for 0.9 ML Cu, and it is found with XPS that approximately one third of the adsorbed oxygen is left on the surface after TPD corresponding to the expected ratio. Furthermore, it is observed under UHV conditions that small amounts of preadsorbed atomic oxygen significantly lowers the activation barrier for carbonate formation.
The hydrogenation of carbonate produced with 0.3 bar CO_2 at room temperature has been monitored with XPS and TPD, and a significant loss of carbonate is found when it is subjected to 0.2 bar H_2 at room temperature. The presence of formate is not clearly observed with TPD, possibly due to rapid hydrogenation of the formate species itself. It is possible that the key step in methanol synthesis is the activation of CO_2 through a

carbonate intermediate and this activation is necessary to form formate.
Formate synthesis from a 0.5 bar gas mixture of 70 % CO_2 and balance H_2 has been shown to occur by means of PM-IRRAS and TPD on Cu/Pt(111) with an optimal temperature around 353-363 K. Formate decomposes into CO_2 and H_2 at 415 K for 1 ML Cu, which is slightly lower than previously reported on low-index Cu surfaces, but in good agreement with studies on Cu-based catalysts. This suggests the reactivity of the stretched Cu is significantly different compared to Cu(111). At higher Cu coverages (4.4 ML) only small amounts of formate is synthesized and carbonate is present.
Generally, it is found that strained Cu(111) overlayers behave differently than pristine Cu(111) in relation to the interaction with CO_2 and the formate synthesis. It is however also clear that further studies with other techniques such as STM are needed to elucidate the mechanism of carbonate and formate hydrogenation, as well as the presence of a possible adsorbate induced reconstruction of the surface.

Trends for the catalytic activity of the water-gas shift reaction for several transition metals have been studied by development of a microkinetic model utilizing the surface redox mechanism. By comparison of the DFT-derived binding energies for all involved surface intermediates and activation energies for the rate-controlling steps, strong linear correlations between most of the parameters are found. Two descriptors, the binding energies for carbon monoxide and atomic oxygen, are identified and used to describe surface reactivity. It has been sought to decrease the number of descriptors to one reduced energy by employing a relationship between the two binding energies. The behavior of the reaction rate is, however, too complicated to be described in a simple way using a single descriptor.
A fair qualitative estimation of the relative activity order of the different transition metal catalysts is found. However, the model fails to quantitatively reproduce experimental data over such a broad range of metals. This discrepancy can to some extent be explained by the fact that the coverage dependence of binding energies has been neglected. In the vicinity of copper the model is expected to describe the catalyst performance well, and it thus predicts that the activity of the copper-based WGS catalyst may be improved by an increase in the reactivity toward carbon monoxide and oxygen. This conclusion was not obvious prior to the present investigation.
Water-gas shift activity measurements for several transition metals on an inert $MgAl_2O_4$ support are correlated to the binding energies of atomic oxygen and carbon monoxide to elucidate the modeling results. It is found that the metals may be be divided into two groups with a weak and strong CO interaction, respectively. The experimental results suggest that further improvement of the water-gas shift activity could be obtained by modifying Cu such that the binding energy of oxygen is increased, and the CO adsorption remains fairly unaffected.

8.2 Outlook

During the course of the presented investigations, several areas of interest as well as experiments have been identified, which would help clarify the nature and behavior of the different systems.
Some speculations of the state of the Cu surface have arisen during the study of the growth, as there are some discrepancies when reviewing the literature on the subject. It would especially be interesting to obtain knowledge of the extent of second layer island formation at low coverages of Cu to understand under which conditions a true pseudomorphic layer is obtained. It has furthermore been speculated that an adsorbate (O, CO_3, HCOO) induced reconstruction of the Cu surface may be taking place during reaction. To elucidate both the growth and the reconstruction, it would however be required to employ scanning tunneling microscopy, which is presently not available on the setup.
In connection with the studies of the reactivity of Cu layers on Pt, it would be interesting to look further into the hydrogenation of carbonate. such that conclusive evidence for the existence of formate and possibly other hydrogenation products could be found. This would require further tuning of the reaction parameters. The next logical step would then be to carry out water-gas shift measurements on Cu/Pt(111) and compare the reactivity to Cu(111), which would give the means needed to examine the validity of the findings of the microkinetic model.
After looking into these reactions on the Cu-Pt bimetallic system, the reactivity of stepped copper samples could be addressed, as the examination of the methanol and formate synthesis, as well as the decomposition on high-index copper single crystal surfaces is somewhat overlooked. This may ultimately help elucidate the connection between carbonate and formate. Two double-sided single crystals with facets Cu(211) / Cu(111) and Cu(14 13 13) / Cu(111) are presently available, over which the formation and hydrogenation of carbonate, water-gas shift, and methanol synthesis could be examined. The latter would require the installation of a new sniffer design, a freeze vessel, and a gas chromatograph to gather the produced methanol and analyze it.
The microkinetic model which is deemed most reliable at binding energies for carbon monoxide and atomic oxygen close to that of Cu, may benefit from an inclusion of coverage dependent binding energies, as it has been found to be one of the main shortcomings when describing reactivity of metals estimated to be completely covered by CO or O. This will however in all probability affect the possibility for making linear correlations and hence ruin the fairly simple description. As previously mentioned the model is not necessarily restricted to the redox-mechanism, and it would be interesting to examine the changes when employing other reaction mechanisms like the associative. Furthermore, the estimation of trends on different transition metals could be expanded to describe the methanol synthesis reactivity. This however requires further DFT calculations to estimate changes in binding and reaction energies for the added intermediates and rate-controlling steps.

Bibliography

[1] B. Hammer and J. K. Nørskov, "Theoretical surface science and catalysis - calculations and concepts," *Adv. Catal.*, vol. 45, pp. 71–129, 2000.

[2] P. Stoltze and J. K. Nørskov, "Bridging the "pressure gap" between ultrahigh-vacuum surface physics and high-pressure catalysis," *Phys. Rev. Lett.*, vol. 55, pp. 2502–2505, 1985.

[3] P. Stoltze and J. K. Nørskov, "An interpretation of the high-pressure kinetics of ammonia synthesis based on a microscopic model," *J. Catal.*, vol. 110, pp. 1–10, 1988.

[4] J. Greeley, T. F. Jaramillo, J. Bonde, I. Chorkendorff, and J. K. Nørskov, "Computational high-throughput screening of electrocatalytic materials for hydrogen evolution," *Nature Mater.*, vol. 5, pp. 909–913, 2006.

[5] M. P. Andersson, T. Bligaard, A. Kustov, K. E. Larsen, J. Greeley, T. Johannessen, C. H. Christensen, and J. K. Nørskov, "Toward computational screening in heterogeneous catalysis: Pareto-optimal methanation catalysts," *J. Catal.*, vol. 239, pp. 501–506, 2006.

[6] J. Pantförder, S. Pöllmann, J. F. Zhu, D. Borgmann, R. Denecke, and H.-P. Steinrück, "New setup for in situ x-ray photoelectron spectroscopy from ultrahigh vacuum to 1 mbar," *Rev. Sci. Instrum.*, vol. 76, pp. 014102–1–9, 2005.

[7] P. L. Hansen, S. Helveg, and A. K. Datye, "Atomic-scale imaging of supported metal nanocluster catalysts in the working state," *Adv. Catal.*, vol. 50, pp. 77–95, 2006.

[8] C. Rhodes, G. J. Hutchings, and A. M. Ward, "Water-gas shift reaction: finding the mechanistic boundary," *Catal. Today*, vol. 23, pp. 43–58, 1995.

[9] M. Twigg and M. Spencer, "Deactivation of supported copper metal catalysts for hydrogenation reactions," *Appl. Catal. A*, vol. 212, pp. 161–174, 2001.

[10] Y. Tanaka, T. Utaka, R. Kikuchi, K. Sasaki, and K. Eguchi, "Water gas shift reaction over Cu-based mixed oxides for CO removal from the reformed fuels," *Appl. Catal. A*, vol. 242, pp. 287–295, 2003.

[11] H. F. Oetjen, V. M. Schmidt, U. Stimming, and F. Trila, "Performance data of a proton exchange membrane fuel cell using H_2/CO as fuel gas," *J. Electrochem. Soc.*, vol. 143, pp. 3838–3842, 1996.

[12] P. Davies, F. Snowden, G. Bridger, D. Huges, and D. Young, "Us patent 1,010,871," 1966.

[13] I. Chorkendorff and J. W. Niemantsverdriet, *Concepts of Modern Catalysis and Kinetics*. Wiley-VCH, 2003.

[14] http://www.methanol.org/.

[15] M. Maack, H. Friis-Jensen, S. Sckerl, J. H. Larsen, and I. Chorkendorff, "Methanol synthesis on potassium-modified Cu(100) from CO + H," *Top. Catal.*, vol. 22, pp. 151–160, 2003.

[16] K. Klier, "Methanol synthesis," *Adv. Catal.*, vol. 31, pp. 243–313, 1982.

[17] K. C. Waugh, "Methanol synthesis," *Catal. Today*, vol. 15, pp. 51–75, 1992.

[18] J. Nakamura, Y. Choi, and T. Fujitani, "On the issue of the active site and the role of ZnO in Cu/ZnO methanol synthesis catalysts," *Top. Catal.*, vol. 22, pp. 277–285, 2003.

[19] X.-M. Liu, G. Q. Lu, Z.-F. Yan, and J. Beltramini, "Recent advances in catalysts for methanol synthesis via hydrogenation of CO and CO_2," *Ind. Eng. Chem. Res.*, vol. 42, pp. 6518–6530, 2003.

[20] A. Y. Rozovskii and G. I. Lin, "Fundamentals of methanol synthesis and decomposition," *Top. Catal.*, vol. 22, pp. 137–150, 2003.

[21] Y. B. Kagan, A. Y. Rozovskii, L. G. Liberov, E. V. Slivinskii, G. I. Lin, S. M. Loktev, and A. N. Bashkirov, "Study of mechanism of methanol synthesis from carbon-monoxide and hydrogen using carbon isotope C-14," *Dokl. Akad. Nauk. SSSR*, vol. 224, pp. 1081–1084, 1975.

[22] G. C. Chinchen, P. J. Denny, D. G. Parker, M. S. Spencer, K. Waugh, and D. Whan, "Mechanism of methanol synthesis from CO_2/CO/H_2 mixtures over copper/zinc oxide/alumina catalysts - use of C-14-labeled reactants," *Appl. Catal.*, vol. 30, pp. 333–338, 1987.

[23] P. B. Rasmussen, M. Kazuta, and I. Chorkendorff, "Synthesis of methanol from a mixture of H_2 and CO_2 on Cu(100)," *Surf. Sci.*, vol. 318, pp. 267–280, 1994.

[24] P. B. Rasmussen, P. M. Holmblad, T. Askgaard, C. V. Ovesen, P. Stoltze, J. K. N. rskov, and I. Chorkendorff, "Methanol synthesis on Cu(100) from a binary gas mixture of co$_2$ and h$_2$," *Catal. Lett.*, vol. 26, pp. 373–381, 1994.

[25] M. Bowker, R. A. Hadden, H. Houghton, J. N. K. Hyland, and K. C. Waugh, "The mechanism of methanol synthesis on copper / zinc oxide / alumina catalysts," *J. Catal.*, vol. 109, pp. 263–273, 1988.

[26] T. S. Askgaard, J. K. Nørskov, C. V. Ovesen, and P. Stoltze, "A kinetic model of methanol synthesis," *J. Catal.*, vol. 156, pp. 229–242, 1995.

[27] H. Nakano, I. Nakamura, T. Fujitani, and J. Nakamura, "Structure-dependent kinetics for synthesis and decomposition of formate species over Cu(111) and Cu(110) model catalysts," *J. Phys. Chem. B*, vol. 105, pp. 1355–1365, 2001.

[28] G. J. Millar, C. H. Rochester, C. Howe, and K. C. Waugh, "A combined infrared, temperature programmed desorption and temperature programmed reaction spectroscopy study of CO_2 and H_2 interactions on reduced and oxidized silica-supported copper catalysts," *Mol. Phys.*, vol. 76, pp. 833–849, 1991.

[29] S. Bailey, G. F. Froment, J. W. Snoeck, and K. C. Waugh, "A DRIFTS study of the morphology and surface adsorbate composition of an operating methanol synthesis catalyst," *Catal. Lett.*, vol. 30, pp. 99–111, 1995.

[30] K. C. Waugh, "The absorption and locking-in of hydrogen in copper," *Sol. Stat. Ion.*, vol. 168, pp. 327–342, 2004.

[31] C. V. Ovesen, B. S. Clausen, J. S. tz, P. Stoltze, H. Topsøe, and J. K. Nørskov, "Kinetic implications of dynamical changes in catalyst morphology during methanol synthesis over Cu/ZnO catalysts," *J. Catal.*, vol. 168, pp. 133–142, 1997.

[32] K. M. V. Bussche and G. F. Froment, "A steady-state kinetic model for methanol synthesis and the water gas shift reaction on a commercial $Cu/ZnO/Al_2O_3$ catalyst," *J. Catal.*, vol. 161, pp. 1–10, 1996.

[33] T. Fujitani, I. Nakamura, T. Uchijima, and J. Nakamura, "The kinetics and mechanism of methanol synthesis by hydrogenation of CO_2 over a Zn-deposited Cu(111) surface," *Surf. Sci.*, vol. 383, pp. 285–298, 1997.

[34] P. A. Taylor, P. B. Rasmussen, and I. Chorkendorff, "Is the observed hydrogenation of formate the rate-limiting step in methanol synthesis?," *J. Chem. Soc. Faraday Trans.*, vol. 91, pp. 1267–1269, 1995.

[35] P. L. Hansen, J. B. Wagner, S. Helveg, J. Rostrup-Nielsen, B. S. Clausen, and H. Topsøe, "Atom-resolved imaging of dynamic shape changes in supported copper nanocrystals," *Science*, vol. 295, pp. 2053–2055, 2002.

[36] O. Dulub, M. Batzill, and U. Diebold, "Growth of copper on single crystalline ZnO: Surface study of a model catalyst," *Top. Catal.*, vol. 36, pp. 65–76, 2005.

[37] G. C. Chinchen, K. Waugh, and D. Whan, "The activity and state of the copper surface in methanol synthesis catalysts," *Appl. Catal.*, vol. 25, pp. 101–107, 1986.

[38] J. Yoshihara, S. C. Parker, A. Schafer, and C. T. Campbell, "Methanol synthesis and reverse water-gas shift kinetics over clean polycrystalline copper," *Catal. Lett.*, vol. 31, pp. 313–324, 1995.

[39] J. Yoshihara and C. T. Campbell, "Methanol synthesis and reverse water-gas shift kinetics over Cu(110) model catalysts: Structural sensitivity," *J. Catal.*, vol. 161, pp. 776–782, 1996.

[40] I. Nakamura, T. Fujitani, T. Uchijima, and J. Nakamura, "A model catalyst for methanol synthesis: Zn-deposited and Zn-free Cu surfaces," *J. Vac. Sci. Technol. A*, vol. 14, pp. 1464–1468, 1996.

[41] N.-Y. Topsøe and H. Topsøe, "FTIR studies of dynamic surface structural changes in Cu-based methanol synthesis catalysts," *J. Mol. Catal. A*, vol. 141, pp. 95–105, 1999.

[42] J. Greeley, A. A. Gokhale, J. Kreuser, J. A. Dumesic, H. Topsøe, N.-Y. Topsøe, and M. Mavrikakis, "CO vibrational frequencies on methanol synthesis catalysts: a DFT study," *J. Catal.*, vol. 213, pp. 63–72, 2003.

[43] R. G. Herman, K. Klier, G. W. Simmons, B. P. Finn, and J. B. Bulko, "Catalytic synthesis of methanol from CO/H_2. (i.) phase composition, electronic properties, and activities of the $Cu/ZnO/M_2O_3$ catalysts," *J. Catal.*, vol. 56, pp. 407–429, 1979.

[44] S. Mehta, G. W. Simmons, K. Klier, and R. G. Herman, "Catalytic synthesis of methanol from CO/H_2. II. Electron microscopy (TEM, STEM, microdiffraction, and energy dispersive analysis) of the Cu/ZnO and $Cu/ZnO/Cr_2O_3$ catalysts," *J. Catal.*, vol. 57, pp. 339–360, 1979.

[45] Y. Okamoto, K. Fukino, T. Imanaka, and S. Teranishi, "Surface characterization of copper(II) oxide-zinc oxide methanol-synthesis catalysts by x-ray photoelectron spectroscopy. 2. Reduced catalysts," *J. Phys. Chem.*, vol. 87, pp. 3747–3754, 1983.

[46] J. C. Frost, "Junction effect interactions in methanol synthesis catalysts," *Nature*, vol. 334, pp. 577–580, 1988.

[47] T. Fujitani and J. Nakamura, "The effect of ZnO in methanol synthesis catalysts on Cu dispersion and the specific activity," *Catal. Lett.*, vol. 56, pp. 119–124, 1998.

[48] T. Fujitani and J. Nakamura, "The chemical modification seen in the Cu/ZnO methanol synthesis catalysts," *Appl. Catal. A*, vol. 191, pp. 111–129, 2000.

[49] Y. Choi, K. Futagami, T. Fujitani, and J. Nakamura, "The role of ZnO in Cu/ZnO methanol synthesis catalysts - morphology effect or active site model?," *Appl. Catal. A*, vol. 208, pp. 163–167, 2001.

[50] J.-D. Grunwaldt, A. M. Molenbroek, N.-Y. Topsøe, H. Topsøe, and B. S. Clausen, "In situ investigations of structural changes in Cu/ZnO catalysts," *J. Catal.*, vol. 194, pp. 452–460, 2000.

[51] J. B. Wagner, P. L. Hansen, A. M. Molenbroek, H. Topsøe, B. S. Clausen, and S. Helveg, "In situ electron energy loss spectroscopy studies of gas-dependent metal-support interactions in Cu/ZnO catalysts," *J. Phys. Chem. B*, vol. 107, pp. 7753–7758, 2003.

[52] H. Topsøe, "Developments in operando studies and in situ characterization of heterogeneous catalysts," *J. Catal.*, vol. 216, pp. 155–164, 2003.

[53] M. M. Günter, T. Ressler, B. Bems, C. Büscher, T. Genger, O. Hinrichsen, M. Muhler, and R. Schlögl, "Implication of the microstructure of binary Cu/ZnO catalysts for their catalytic activity in methanol synthesis," *Catal. Lett.*, vol. 71, pp. 37–44, 2001.

[54] R. Burch, S. E. Golunski, and M. S. Spencer, "The role of hydrogen in methanol synthesis over copper catalysts," *Catal. Lett.*, vol. 5, pp. 55–60, 1990.

[55] M. S. Spencer, "Role of ZnO in methanol synthesis on copper catalysts," *Catal. Lett.*, vol. 50, pp. 37–40, 1998.

[56] N. Schumacher, A. Boisen, S. Dahl, A. A. Gokhale, S. Kandoi, L. C. Grabow, J. A. Dumesic, M. Mavrikakis, and I. Chorkendorff, "Trends in low-temperature water-gas shift reactivity on transition metals," *J. Catal.*, vol. 229, pp. 265–275, 2005.

[57] M. Johansson, J. H. Jørgensen, and I. Chorkendorff, "Combined high-pressure cell-ultrahigh vacuum system for fast testing of model metal alloy catalysts using scanning mass spectrometry," *Rev. Sci. Instrum.*, vol. 75, pp. 2082–2093, 2004.

[58] I. Chorkendorff, "Experimental surface physics - course notes," 2004.

[59] J. W. Niemantsverdriet, *Spectroscopy in Catalysis*. VCH, 1993.

[60] F. M. Propst and T. C. Piper, "Detection of the vibrational states of gases adsorbed on tungsten by low-energy electron scattering," *J. Vac. Sci. Technol.*, vol. 4, pp. 53–56, 1967.

[61] P. A. Thiry, M. Liehr, J. J. Pireaux, and R. Caudano, "Electron interaction mechanisms in high-resolution electron-energy loss spectroscopy," *Phys. Scr.*, vol. 35, pp. 368–379, 1987.

[62] H. Ibach, "Electron energy loss spectroscopy: the vibration spectroscopy of surfaces," *Surf. Sci.*, vol. 299/300, pp. 116–128, 1994.

[63] C. D. Wagner, W. M. Riggs, L. E. Davis, J. F. Moulder, and G. E. M. (Editor), *Handbook of X-ray photoelectron spectroscopy*. Perkin-Elmer Corporation, Physical Electronics Division, 1979.

[64] http://srdata.nist.gov/xps/.

[65] R. M. Nix, *An Introduction to Surface Chemistry*. http://www.chem.qmul.ac.uk/surfaces/scc/, 2003.

[66] A. E. Dowrey and C. Marcott, "A double-modulation fourier transform infrared approach to studying adsorbates on metal surfaces," *Appl. Spectrosc.*, vol. 36, pp. 414–416, 1982.

[67] T. Buffeteau, B. Desbat, and J. M. Turlet, "Polarization modulation FT-IR spectroscopy of surfaces and ultra-thin films: Experimental procedure and quantitative analysis," *Appl. Spectrosc.*, vol. 45, pp. 380–389, 1991.

[68] R. G. Greenler, "Design of a reflection-absorption experiment for studying the ir spectrum of molecules adsorbed on a metal surface," *J. Vac. Sci. Technol.*, vol. 12, pp. 1410–1417, 1975.

[69] F. M. Hoffmann, "Infrared reflection-absorption spectroscopy of adsorbed molecules," *Surf. Sci. Rep.*, vol. 3, pp. 107–192, 1983.

[70] D. R. Lide, ed., *CRC Handbook of Chemistry and Physics*. CRC Press, 87th edition ed., 2006-2007.

[71] R. G. Greenler, "Infrared study of adsorbed molecules on metal surfaces by reflection techniques," *J. Chem. Phys.*, vol. 44, pp. 310–315, 1966.

[72] D. P. Woodruff and T. A. Delchar, *Modern Techniques of Surface Science*. Cambridge University Press, 2nd edition ed., 1994.

[73] J. D. E. McIntyre and D. E. Aspnes, "Differential reflection spectroscopy of very thin surface films," *Surf. Sci.*, vol. 24, p. 417, 1971.

[74] Y.-S. Yen and J. S. Wong, "Infrared reflectance properties of surface thin films," *J. Phys. Chem.*, vol. 93, pp. 7208–7216, 1989.

[75] M. Andersen, *Implementation of in situ vibrational spectroscopy in studies of surface reactions on platinum*. PhD thesis, Technical University of Denmark (DTU), 2005.

[76] X. Cao, R. D. Shah, R. K. Dukor, C. Guo, T. B. Freedman, and L. A. Nafie, "Extension of fourier transform vibrational circular dichroism into the near-infrared region: Continuous spectral coverage from 800 to 10000 cm^{-1}," *App. Spec.*, vol. 58, pp. 1057–1064, 2004.

[77] H. I. Inc., *PEM-90*^{TM} *photoelastic modulator systems user manual*, 1998.

[78] B. J. Barner, M. J. Green, E. I. Sáez, and R. M. Corn, "Polarization modulation Fourier transform infrared reflectance measurements of thin films and monolayers at metal surfaces utilizing real-time sampling electronics," *Anal. Chem.*, vol. 63, pp. 55–60, 1991.

[79] K. W. Hipps and G. A. Crosby, "Applications of the photoelastic modulator to polarization spectroscopy," *J. Phys. Chem.*, vol. 83, pp. 555–562, 1979.

[80] M. J. Green, B. J. Barner, and R. M. Corn, "Real-time sampling electronics for double modulation experiments with Fourier transform infrared spectrometers," *Rev. Sci. Instrum.*, vol. 62, pp. 1426–1430, 1991.

[81] D. Stacchiola, A. W. Thompson, M. Kaltchev, and W. T. Tysoe, "Photoelastic modulation-reflection absorption infrared spectroscopy of CO on Pd(111)," *J. Vac. Sci. Technol. A*, vol. 20, pp. 2101–2105, 2002.

[82] W. N. Richmond, P. W. Faguy, R. S. Jackson, and S. C. Weibel, "Comparison between real-time polarization modulation and static linear polarization for in situ infrared spectroscopy at electrode surfaces," *Anal. Chem.*, vol. 68, pp. 621–628, 1996.

[83] R. P. Eischens and W. A. Pliskin, "The infrared spectra of adsorbed molecules," *Advan. Catal.*, vol. 10, pp. 1–56, 1958.

[84] G. Blyholder, "Molecular orbital view of chemisorbed carbon monoxide," *J. Phys. Chem.*, vol. 68, pp. 2772–2777, 1964.

[85] G. Blyholder, "CNDO model of carbon monoxide chemisorbed on nickel," *J. Phys. Chem.*, vol. 79, pp. 756–761, 1975.

[86] M. Scheffler, "The influence of lateral interactions on the vibrational spectrum of adsorbed CO," *Surf. Sci.*, vol. 81, pp. 562–570, 1979.

[87] G. D. Mahan and A. A. Lucas, "Collective vibrational modes of adsorbed CO," *J. Chem. Phys.*, vol. 68, p. 1344, 1978.

[88] B. N. J. Persson and R. Ryberg, "Vibrational interaction between molecules adsorbed on a metal surface: The dipole-dipole interaction," *Phys. Rev. B*, vol. 24, pp. 6954–6970, 1981.

[89] M. W. Severson, C. Stuhlmann, I. Villegas, and M. J. Weaver, "Dipole-dipole coupling effects upon infrared spectroscopy of compressed electrochemical adlayers: application to the Pt(111)/CO system," *J. Chem. Phys.*, vol. 103, pp. 9832–9843, 1995.

[90] H. Pfnür, D. Menzel, F. M. Hoffmann, A. Ortega, and A. M. Bradshaw, "High resolution vibrational spectroscopy of CO on Ru(001): The importance of lateral interactions," *Surf. Sci.*, vol. 93, pp. 431–452, 1980.

[91] A. Ruban, B. Hammer, P. Stoltze, H. L. Skriver, and J. K. N. rskov, "Surface electronic structure and reactivity of transition and noble metals," *J. Mol. Catal. A*, vol. 115, pp. 421–429, 1997.

[92] G. Chinchen, P. Denny, J. Jennings, M. Spencer, and K. Waugh, "Synthesis of methanol - Part 1. catalysts and kinetics," *Appl. Catal.*, vol. 36, pp. 1–65, 1988.

[93] F. R. de Boer, R. Boom, W. C. M. Mattens, A. R. Miedema, and A. K. Niessen, *Cohesion in Metals, Transition Metal Alloys.* North-Holland Physics Publishing, 1989.

[94] M. L. Shek, P. M. Stefan, I. Lindau, and W. E. Spicer, "Photoemission study of the adsorption of Cu on Pt(111)," *Phys. Rev. B*, vol. 27, pp. 7277–7287, 1983.

[95] M. L. Shek, P. M. Stefan, I. Lindau, and W. E. Spicer, "CO chemisorption on Cu adlayers on Pt(111)," *Phys. Rev. B*, vol. 27, pp. 7301–7312, 1983.

[96] R. C. Yeates and G. A. Somorjai, "The growth and alloy formation of copper on the platinum (111) and stepped (553) crystal surfaces: characterization by LEED, AES, and CO thermal desorption," *Surf. Sci.*, vol. 134, pp. 729–744, 1983.

[97] M. T. Paffett, C. T. Campbell, T. N. Taylor, and S. Srinivasan, "Cu adsorption on Pt(111) and its effects on chemisorption: A comparison with electrochemistry," *Surf. Sci.*, vol. 154, pp. 284–302, 1985.

[98] J. A. Rodriguez, C. M. Truong, and D. W. Goodman, "Infrared vibrational studies of co adsorption on Cu/Pt(111) and CuPt(111)," *J. Chem. Phys.*, vol. 96, pp. 7814–7825, 1992.

[99] J. A. Rodriguez and M. Kuhn, "Electronic and chemical properties of Ag/Pt(lll) and Cu/Pt(lll) surfaces: Importance of changes in the d electron populations," *J. Phys. Chem.*, vol. 98, pp. 11251–11255, 1994.

[100] M. Nohlen, M. Schmidt, and K. Wandelt, "On the influence of adsorbates on heteroepitaxy: work function oscillations during deposition of copper on platinum (111)," *Surf. Sci.*, vol. 331-333, pp. 902–907, 1995.

[101] M. Kolodzejczyk, R. E. R. Colen, B. Delmon, and J. H. Block, "Interaction between Cu and Pt(111) in the reaction CO + O_2. modification by Cu sub-monolayers and cooperation between pure and Cu-modified Pt(111)," *Appl. Surf. Sci.*, vol. 121-122, pp. 480–483, 1997.

[102] B. Holst, M. Nohlen, K. Wandelt, and W. Allison, "The growth of ultra thin Cu-films on Pt(111), probed by helium atom scattering and scanning tunnelling microscopy," *Surf. Sci.*, vol. 377-379, pp. 891–894, 1997.

[103] B. Holst, M. Nohlen, K. Wandelt, and W. Allison, "RAPID COMMUNICATIONS - Surface physics, low-dimensional systems, and related topics - Observation of an adlayer-driven substrate reconstruction in Cu-Pt(111)," *Phys. Rev. B. - Condensed Matter*, vol. 58, pp. 195–198, 1998.

[104] J. S. Tsay, T. Mangen, R.-J. Linden, and K. Wandelt, "Comparative study of annealing effects for cu/pt(111) films with and without oxygen," *Surf. Sci.*, vol. 482-485, pp. 866–871, 2001.

[105] J. S. Tsay, T. Mangen, R.-J. Linden, and K. Wandelt, "Adsorption of oxygen on ultrathin Cu/Pt(111) films," *J. Vac. Sci. Technol. A*, vol. 19, pp. 2217–2221, 2001.

[106] J. S. Tsay, T. Mangen, and K. Wandelt, "Kinetic study of the formation of a surface-confined $Cu_{50}Pt_{50}$ alloy," *Thin Sol. Films*, vol. 397, pp. 152–156, 2001.

[107] A. Canzian, H. O. Mosca, and G. Bozzolo, "Atomistic modeling of Pt deposition on Cu(111) and Cu deposition on Pt(111)," *Surf. Rev. Lett.*, vol. 11, pp. 235–243, 2004.

[108] J. Knudsen, A. U. Nilekar, R. T. Vang, J. Schnadt, E. L. Kunkes, J. A. Dumesic, M. Mavrikakis, and F. Besenbacher, "A Cu/Pt near-surface alloy for water-gas shift catalysis," *J. Am. Chem. Soc.*, vol. 129, pp. 6485–6490, 2007.

[109] D. A. MacLaren, R. T. Bacon, W. Allison, D. J. O'Connor, P. C. Dastoor, T. C. Q. Noakes, and P. Bailey, "Submonolayer alloying of copper on vicinal platinum: A combined atom and ion scattering study," *Phys. Rev. B*, vol. 70, p. 125403, 2004.

[110] L.-W. H. Leung, T. W. Gregg, and D. W. Goodman, "Electrochemical and ultrahigh vacuum characterization of ultrathin Cu films on Pt(111)," *Langmuir*, vol. 7, pp. 3205–3210, 1991.

[111] F. Jensen, F. Besenbacher, E. Lægsgaard, and I. Stensgaard, "Surface reconstruction of cu(110) induced by oxygen chemisorption," *Phys. Rev. B*, vol. 41, no. 14, pp. 10233–10236, 1990.

[112] F. Solymosi, "The bonding, structure and reactions of CO_2 adsorbed on clean and promoted metal surfaces," *J. Mol. Catal.*, vol. 65, pp. 337–358, 1991.

[113] H.-J. Freund and M. W. Roberts, "Surface chemistry of carbon dioxide," *Surf. Sci. Rep.*, vol. 25, pp. 225–273, 1996.

[114] S. S. Fu and G. A. Somorjai, "Interactions of O_2, co, CO_2, and D_2 with the stepped Cu(311) crystal face: comparison to Cu(110)," *Surf. Sci.*, vol. 262, pp. 68–76, 1992.

[115] I. A. Bönicke, W. Kirstein, and F. Thieme, "A study on CO_2 dissociation on a stepped (332) copper surface," *Surf. Sci.*, vol. 307-309, pp. 177–181, 1994.

[116] Adsorption, reactivity of CO_2 on the K/Cu(110) interface, and the effect of photon irradiation, "E. v. thomsen and b. jørgensen and j. onsgaard," *Surf. Sci.*, vol. 304, pp. 85–97, 1994.

[117] A. F. Carley, M. W. Roberts, and A. J. Strutt, "Activation of carbon monoxide and carbon dioxide at cesium-promoted Cu(110) and Cu(110)-O surfaces," *J. Phys. Chem.*, vol. 98, pp. 9175–9181, 1994.

[118] F. H. P. M. Habraken, E. P. Kieffer, and G. A. Bootsma, "A study of the kinetics of the interactions of O_2 and N_2O with a Cu(111) surface and of the reaction of CO with adsorbed oxygen using AES, LEED and ellipsometry," *Surf. Sci.*, vol. 83, pp. 45–59, 1979.

[119] C. T. Campbell, K. A. Daube, and J. M. White, "Cu/zno$(000\bar{1})$ and zno$_x$/cu(111): Model catalysts for methanol synthesis," *Surf. Sci.*, vol. 182, pp. 458–476, 1987.

[120] J. A. Rodriquez, W. D. Clendering, and C. T. Campbell, "Adsorption of CO and CO_2 on clean and cesium-covered Cu(110)," *J. Phys. Chem.*, vol. 93, pp. 5238–5248, 1989.

[121] J. Krause, D. Borgmann, and G. Wedler, "Photoelectron spectroscopic study of the adsorption of carbon dioxide on Cu(ll0) and Cu(110)/K - as compared with the systems Fe(110)/CO_2 and Fe(ll0)/K + CO_2," *Surf. Sci.*, vol. 347, pp. 1–10, 1996.

[122] K.-H. Ernst, D. Schlatterbeck, and K. Christmann, "Adsorption of carbon dioxide on Cu(110) and on hydrogen and oxygen covered Cu(110) surfaces," *Phys. Chem. Chem. Phys.*, vol. 1, pp. 4105–4112, 1999.

[123] S. Funk, B. Hokkanen, J. Wang, U. Burghaus, G. Bozzolo, and J. E. Garcés, "Adsorption dynamics of CO_2 on Cu(110): A molecular beam study," *Surf. Sci.*, vol. 600, pp. 583–590, 2006.

[124] I. E. Wachs and R. J. Madix, "Selective oxidation of CH_3OH to H_2CO on a copper(110) catalyst," *J. Catal.*, vol. 53, pp. 208–227, 1978.

[125] T. Schneider and W. Hirschwald, "Interaction of carbon-dioxide with clean and oxygenated Cu(110) surfaces," *Catal. Lett.*, vol. 14, pp. 197–205, 1992.

[126] C. T. Campbell, "Interaction of carbon-dioxide with clean and oxygenated Cu(110) surfaces - comment," *Catal. Lett.*, vol. 16, pp. 455–457, 1992.

[127] T. Schneider and W. Hirschwald, "Interaction of carbon-dioxide with clean and oxygenated Cu(110) surfaces - responce," *Catal. Lett.*, vol. 16, pp. 459–460, 1992.

[128] J. Nakamura, J. A. Rodriguez, and C. T. Campbell, "Does CO_2 dissociatively adsorb on Cu surfaces," *J. Phys. Condens. Matter*, vol. 1, pp. SB149–SB160, 1989.

[129] P. B. Rasmussen, P. A. Taylor, and I. Chorkendorff, "The interaction of carbon dioxide with Cu(100)," *Surf. Sci.*, vol. 269/270, pp. 352–359, 1992.

[130] R. G. Copperthwaite, P. R. Davies, M. A. Morris, M. W. Roberts, and R. A. Ryder, "The reactive chemisorption of carbon dioxide at magnesium and copper surfaces at low temperature," *Catal. Lett.*, vol. 1, pp. 11–20, 1988.

[131] R. A. Hadden, H. D. Vandervell, K. C. Waugh, and G. Webb, "The adsorption and decomposition of carbon dioxide on polycrystalline copper," *Catal. Lett.*, vol. 1, pp. 27–34, 1988.

[132] A. F. Carley, A. Chambers, P. R. Davies, G. G. Mariotti, R. Kurian, and M. W. Roberts, "Surface oxygen and chemical specificity at copper and caesium surfaces," *Faraday Discuss.*, vol. 105, pp. 225–235, 1996.

[133] T. Haas and J. Pritchard, "Adsorption of carbon dioxide on polycrystalline copper," *J. Chem. Soc. Faraday Trans.*, vol. 86, pp. 1889–1892, 1990.

[134] V. M. Browne, A. F. Carley, R. G. Copperthwaite, P. R. Davies, E. M. Moser, and M. W. Roberts, "Activation of carbon-dioxide at bismuth, gold and copper surfaces," *Appl. Surf. Sci.*, vol. 47, pp. 375–379, 1991.

[135] G. C. Chinchen, M. S. Spencer, K. C. Waugh, and D. A. Whan, "Promotion of methanol synthesis and the water-gas shift reactions by adsorbed oxygen on supported copper catalysts," *J. Chem. Soc. Faraday Trans. I*, vol. 83, pp. 2193–2212, 1987.

[136] A. J. Elliott, R. A. Hadden, J. Tabatabaei, K. C. Waugh, and F. W. Zemicael, "Inverted temperature-dependence of the decomposition of carbon-dioxide on oxide-supported polycrystalline copper," *J. Catal.*, vol. 157, pp. 153–161, 1995.

[137] E. M. Stuve, R. J. Madix, and B. A. Sexton, "An EELS study of CO_2 and CO_3 adsorbed on oxygen covered Ag(110)," *Chem. Phys. Lett.*, vol. 89, pp. 48–53, 1982.

[138] G. Herzberg, *Molecular Spectra and Molecular Structure, Volume II Infrared and Raman Spectra of Polyatomic Molecules*. Krieger Publishing Company, 1991.

[139] B. Hammer, L. B. Hansen, and J. K. Nørskov, "Improved adsorption energetics within density-functional theory using revised Perdew-Burke-Ernzerhof functionals," *Phys. Rev. B (Condensed Matter)*, vol. 59, pp. 7413–7421, 1999.

[140] J. Greeley, J. K. Nørskov, and M. Mavrikakis, "Electronic structure and catalysis on metal surfaces," *Annu. Rev. Phys. Chem.*, vol. 53, pp. 319–348, 2002.

[141] N. Schumacher, K. Andersson, L. C. Grabow, M. Mavrikakis, J. Nerlov, and I. Chorkendorff, "Interaction of carbon dioxide with Cu overlayers on Pt(111)," *To be submitted*.

[142] L. H. Little, *Infrared spectra of adsorbed species*. Academic Press Inc., 1966.

[143] P. R. Norton, "Surface analysis of platinum by x-ray photoelectron spectroscopy (XPS)," *Surf. Sci.*, vol. 44, pp. 624–628, 1974.

[144] R. J. Behm and C. R. Brundle, "On the formation and bonding of a surface carbonate on Ni(100)," *Surf. Sci.*, vol. 255, pp. 327–343, 1991.

[145] M. A. Barteau and R. J. Madix, "Lateral interaction effects on the reaction of CO_2 and oxygen adsorbed on Ag(110)," *J. Chem. Phys.*, vol. 74, pp. 4144–4149, 1981.

[146] M. Bowker, M. A. Barteau, and R. J. Madix, "Oxygen induced adsorption and reaction of H_2, H_2O, CO and CO_2 on single crystal Ag(110)," *Surf. Sci.*, vol. 92, pp. 528–548, 1980.

[147] A. Kiennemann, H. Idriss, J. P. Hindermann, J. C. Lavalley, A. Vallet, P. Chaumette, and P. Courty, "Methanol synthesis on $Cu/ZnAl_2O_4$ and Cu/ZnO-Al_2O_3 catalysts. Influence of carbon monoxide pretreatment on the formation and concentration of formate species," *Appl. Catal.*, vol. 59, pp. 165–184, 1990.

[148] G. J. Millar, C. H. Rochester, S. Bailey, and K. C. Waugh, "A combined temperature-programmed reaction spectroscopy and fourier-transform infrared-spectroscopy study of CO_2-H_2 and CO-CO_2-H_2 interactions with model ZnO/SiO_2, Cu/SiO_2 and $Cu/ZnO/SiO_2$ methanol synthesis catalysts," *J. Chem. Soc. Faraday Trans.*, vol. 88, pp. 2085–2093, 1992.

[149] S. G. Neophytides, A. J. Marchi, and G. F. Froment, "Methanol synthesis by means of diffuse reflectance infrared Fourier transform and temperature-programmed reaction spectroscopy," *Appl. Catal. A*, vol. 86, pp. 45–64, 1992.

[150] P. A. Taylor, P. B. Rasmussen, C. V. Ovesen, P. Stoltze, and I. Chorkendorff, "Formate synthesis on cu(100)," *Surf. Sci.*, vol. 261, pp. 191–206, 1992.

[151] T. Fujitani, I. Nakamura, S. Ueno, T. Uchijima, and J. Nakamura, "Methanol synthesis by hydrogenation of CO_2 over a Zn-deposited Cu(111): formate intermediate," *Appl. Surf. Sci.*, vol. 121/122, pp. 583–586, 1997.

[152] B. A. Sexton, "Observation of formate species on a copper (100) surface by high resolution electron loss spectroscopy," *Surf. Sci.*, vol. 88, pp. 319–330, 1979.

[153] L. H. Dubois, T. H. Ellis, B. R. Zegarski, and S. D. Kevan, "New insights into the kinetics of formic acid decomposition on copper surfaces," *Surf. Sci.*, vol. 172, pp. 385–397, 1986.

[154] D. H. S. Ying and R. J. Madix, "Thermal desorption study of formic acid decomposition on a clean cu(110) surface," *J. Catal.*, vol. 61, pp. 48–56, 1980.

[155] M. Bowker and R. J. Madix, "XPS, UPS and thermal desorption studies of the reactions of formaldehyde and formic acid with the cu(110) surface," *Surf. Sci.*, vol. 102, pp. 542–565, 1981.

[156] B. E. Hayden, K. Prince, D. P. Woodruff, and A. M. Bradshaw, "An IRAS study of formic acid and surface formate adsorbed on Cu(110)," *Surf. Sci.*, vol. 133, pp. 589–604, 1983.

[157] B. A. Sexton, A. E. Hughes, and N. R. Avery, "A spectroscopic study of the adsorption and reactions of methanol, formaldehyde and methyl formate on clean and oxygenated Cu(110) surfaces," *Surf. Sci.*, vol. 155, pp. 366–386, 1985.

[158] E. Iglesia and M. Boudart, "Unimolecular and bimolecular formic acid decomposition on copper," *J. Phys. Chem.*, vol. 90, pp. 5272–5274, 1986.

[159] G. J. Millar, D. Newton, G. A. Bowmaker, and R. P. Cooney, "In situ FT-IR investigation of formic acid adsorption on reduced and reoxidized copper catalysts," *Appl. Spectrosc.*, vol. 48, pp. 827–832, 1994.

[160] T. Yatsu, H. Nishimura, T. Fujitani, and J. Nakamura, "Synthesis and decomposition of formate on a Cu/SiO_2 catalyst: Comparison to Cu(111)," *J. Catal.*, vol. 191, pp. 423–429, 2000.

[161] J. Yoshihara and C. T. Campbell, "Chemisorption of formic acid and CO on Cu particles on the Zn-terminated ZnO(0001) surface," *Surf. Sci.*, vol. 407, pp. 256–267, 1998.

[162] J. Onsgaard, L. Bech, C. Svensgaard, P. J. Godowski, and S. V. Hoffmann, "Reactions on alkali-modified low-index stepped copper surfaces," *Prog. Surf. Sci.*, vol. 67, pp. 205–216, 2001.

[163] J. Onsgaard, S. V. Hoffmann, P. Møller, P. J. Godowski, J. B. Wagner, G. Paolucci, A. Baraldi, G. Comelli, and A. Groso, "Adsorption of CO_2 and coadsorption of H and CO_2 on potassium-promoted Cu(115)," *Chem. Phys. Chem.*, vol. 4, pp. 466–473, 2003.

[164] K. Christmann, "Adsorption of hydrogen on a Pt(111) surface," *Surf. Sci.*, vol. 54, pp. 365–392, 1976.

[165] P. B. Rasmussen, P. M. Holmblad, H. Christoffersen, P. A. Taylor, and I. Chorkendorff, "Dissociative adsorption of hydrogen on Cu(100) at low temperatures," *Surf. Sci.*, vol. 287/288, pp. 79–83, 1993.

[166] I. Nakamura, H. Nakano, T. Fujitani, T. Uchijima, and J. Nakamura, "Synthesis and decomposition of formate on Cu(111) and Cu(110) surfaces: Structure sensitivity," *J. Vac. Sci. Technol. A*, vol. 17, pp. 1592–1595, 1999.

[167] D. J. Coulman, J. Wintterlin, R. J. Behm, and G. Ertl, "Novel mechanism for the formation of chemisorption phases: The (2x1)o-cu(110) "added-row" reconstruction," *Phys. Rev. Lett.*, vol. 64, pp. 1761–1764, 1990.

[168] S. J. Harrington, K. V. Kilway, D.-M. Zhu, J. M. Phillips, and F. M. Leibsle, "Formate-induced destabilization of the Cu(110) surface," *Surf. Sci.*, vol. 600, pp. 1193–1200, 2006.

[169] G. C. Chinchen, K. Mansfield, and M. S. Spencer, "The methanol synthesis: How does it work?," *Chemtech*, pp. 692–699, 1990.

[170] I. Chorkendorff, P. A. Taylor, and P. B. Rasmussen, "Synthesis and hydrogenation of formate on cu(100) at high pressures," *J. Vac. Sci. Technol. A*, vol. 10, pp. 2277–2281, 1992.

[171] N. Schumacher, "A microkinetic model of the water gas shift reaction," Master's thesis, Technical University of Denmark (DTU), 2004.

[172] M. Andersen, O. Lytken, J. Engbæk, G. Nielsen, N. Schumacher, M. Johansson, and I. Chorkendorff, "Search for new catalysts from a fundamental basis," *Catalysis Today*, vol. 100, pp. 191–197, 2005.

[173] A. Boisen, T. Janssens, N. Schumacher, I. Chorkendorff, and S. Dahl, "Support effects and catalytic trends for water gas shift activity of transition metals," *To be submitted.*

[174] S. Dahl, J. Sehested, C. J. H. Jacobsen, E. T. rnqvist, and I. Chorkendorff, "Surface science based microkinetic analysis of ammonia synthesis over ruthenium catalysts," *J. Catal.*, vol. 192, pp. 391–399, 2000.

[175] C. J. H. Jacobsen, S. Dahl, A. Boisen, B. S. Clausen, H. Topsøe, A. Logadottir, and J. K. Nørskov, "Optimal catalyst curves: Connecting density functional theory calculations with industrial reactor design and catalyst selection," *J. Catal.*, vol. 205, pp. 382–387, 2002.

[176] C. V. Ovesen, *Kinetic Modeling of Reactions on Cu Surfaces.* PhD thesis, DTU, 1992.

[177] C. V. Ovesen, P. Stoltze, J. K. Nørskov, and C. T. Campbell, "A kinetic model of the water gas shift reaction," *J. Catal.*, vol. 134, pp. 445–468, 1992.

[178] A. Boisen, *Study of Transition Metal Catalysts for use in Production of Hydrogen.* PhD thesis, Technical University of Denmark (DTU) & Haldor Topsøe A/S, 2004.

[179] E. F. Armstrong and T. P. Hilditch, "A study of catalytic actions at solid surfaces. IV. the interaction of carbon monoxide and steam as conditioned by iron oxide and by copper," *Proc. Roy. Soc.*, vol. A97, pp. 265–273, 1920.

[180] C. T. Campbell and K. A. Daube, "A surface science investigation of the water-gas shift reaction on Cu(111)," *J. Catal.*, vol. 104, pp. 109–119, 1987.

[181] C. T. Campbell, B. E. Koel, and K. A. Daube, "Surface science studies of the water gas shift reaction on a model Cu(111) catalyst," *J. Vac. Sci. Technol. A*, vol. 5, pp. 810–813, 1987.

[182] J. Nakamura, J. M. Campbell, and C. T. Campbell, "Kinetics and mechanism of the water-gas shift reaction catalyzed by the clean and Cs-promoted Cu(110) surface - a comparison with Cu(111)," *J. Chem. Soc., Faraday Trans.*, vol. 86, pp. 2725–2734, 1990.

[183] C. V. Ovesen, B. S. Clausen, B. S. Hammershøi, G. Steffensen, T. Askgaard, I. Chorkendorff, J. K. Nørskov, P. B. Rasmussen, P. Stoltze, and P. Taylor, "A microkinetic analysis of the water-gas shift reaction under industrial conditions," *J. Catal.*, vol. 158, pp. 170–180, 1996.

[184] T. Bligaard, K. Honkala, A. Logadottir, J. K. Nørskov, S. Dahl, and C. J. H. Jacobsen, "On the compensation effect in heterogeneous catalysis," *J. Phys. Chem. B.*, vol. 107, pp. 9325–9331, 2003.

[185] J. Greeley, J. K. Nørskov, and M. Mavrikakis, "Electronic structure and catalysis on metal surfaces," *Ann. Rev. Phys. Chem.*, vol. 53, pp. 319–348, 2002.

[186] T. Bligaard, J. K. Nørskov, S. Dahl, J. Matthiesen, C. H. Christensen, and J. S. Sehested, "The Brø nsted-Evans-Polanyi relation and the volcano curve in heterogeneous catalysis," *J. Catal.*, vol. 224, pp. 206–217, 2004.

[187] J. K. Nørskov, T. Bligaard, A. Logadottir, S. Bahn, L. B. Hansen, M. Bollinger, H. Bengaard, B. Hammer, Z. Sljivancanin, M. Mavrikakis, Y. Xu, S. Dahl, and C. J. H. Jacobsen, "Priority communication, universality in heterogeneous catalysis," *J. Catal.*, vol. 209, pp. 275–278, 2002.

[188] V. Pallassana and M. Neurock, "Electronic factors governing ethylene hydrogenation and dehydrogenation of pseudomorphic Pd_{ML}/Re(0001), Pd_{ML}/Ru(0001), Pd(111) and Pd_{ML}/Au(111) surfaces," *J. Catal.*, vol. 191, pp. 301–317, 2000.

[189] P. Sabatier, "in: La catalyse en chimique organique, Bérange, Paris," 1920.

[190] N. Lopez and J. K. Nørskov, "Catalytic CO oxidation by a gold nanoparticle: A density functional study," *J. Am. Chem. Soc.*, vol. 124, pp. 11262–11263, 2002.

[191] M. Mavrikakis, B. Hammer, and J. K. Nørskov, "Effect of strain on the reactivity of metal surfaces," *Phys. Rev. Lett.*, vol. 81, pp. 2819–2822, 1998.

[192] Y. Xu and M. Mavrikakis, "Adsorption and dissociation of O_2 on Cu(111): thermochemistry, reaction barrier and the effect of strain," *Surf. Sci.*, vol. 494, pp. 131–144, 2001.

[193] A. Christensen, A. V. Ruban, P. Stoltze, K. W. Jacobsen, H. L. Skriver, J. K. Nørskov, and F. Besenbacher, "Phase diagrams for surface alloys," *Phys. Rev. B*, vol. 56, pp. 5822–5834, 1997.

[194] N.-Y. Topsøe and H. Topsøe, "On the nature of surface structural changes in Cu/ZnO methanol synthesis catalysts," *Top. Catal.*, vol. 8, pp. 267–270, 1999.

[195] J. Nakamura, I. Nakamura, T. Uchijima, Y. Kanai, T. Watanabe, M. Saito, and T. Fujitani, "A surface science investigation of methanol synthesis over a Zn-deposited polycrystalline Cu surface," *J. Catal.*, vol. 160, pp. 65–75, 1996.

[196] D. C. Grenoble, M. M. Estadt, and D. F. Ollis, "The chemistry and catalysis of the water gas shift reaction," *J. Catal.*, vol. 67, pp. 90–102, 1981.

[197] T. Bunluesin, R. J. Gorte, and G. W. Graham, "Studies of the water-gas-shift reaction on ceria-supported Pt, Pd, and Rh; implications for oxygen-storage properties," *Appl. Catal. B: Env.*, vol. 15, pp. 107–114, 1998.

[198] E. K. Vestergaard, P. Thostrup, T. An, E. Lægsgaard, I. Stensgaard, B. Hammer, and F. Besenbacher, "Comment on "High pressure adsorbate structures studied by scanning tunneling microscopy: CO on Pt(111) in equilibrium with the gas phase"," *Phys. Rev. Lett.*, vol. 88, p. 259601, 2002.

[199] J. C. Davies, R. M. Nielsen, L. B. Thomsen, I. Chorkendorff, A. Logadottir, Z. Lodziana, J. K. Norskov, W. X. Li, B. Hammer, S. Longwitz, J. Schnadt, E. K. Vestergaard, R. T. Vang, and F. Besenbacher, "CO desorption rate dependence on CO partial pressure over platinum fuel cell catalysts," *Fuel Cells*, vol. 4, pp. 309–319, 2004.

[200] D. Andreeva, V. Idakiev, T. Tabakova, and A. Andreev, "Low-temperature water-gas shift reaction over Au/α-Fe_2O_3," *J. Catal.*, vol. 158, pp. 354–355, 1996.

[201] F. Boccuzzi, A. Chiorino, M. Manzoli, D. Andreeva, T. Tabakova, L. Ilieva, and V. Iadakiev, "Gold, silver and copper catalysts supported on TiO_2 for pure hydrogen production," *Catal. Today*, vol. 75, pp. 169–175, 2002.

[202] Q. Fu, S. Kudriavtseva, H. Saltsburg, and M. Flytzani-Stephanopoulos, "Gold-ceria catalysts for low-temperature water-gas shift reaction," *Chem. Eng. J.*, vol. 93, pp. 41–53, 2003.

[203] T. Utaka, T. Okanishi, T. Takeguchi, R. Kikuchi, and K. Eguchi, "Water gas shift reaction of reformed fuel over supported Ru catalysts," *Appl. Catal. A*, vol. 245, pp. 343–351, 2003.

[204] J. Nerlov and I. Chorkendorff, "Methanol synthesis from CO_2, CO, and H_2 over Cu(100) and Ni/Cu(100)," *J. Catal.*, vol. 181, pp. 271–279, 1999.

[205] A. A. Phatak, N. Koryabkina, S. Rai, J. L. Ratts, W. Ruettinger, R. J. Farrauto, G. E. Blau, W. N. Delgass, and F. H. Ribeiro, "Kinetics of the water-gas shift reaction on Pt catalysts supported on alumina and ceria," *Catal. Today*, vol. 123, pp. 224–234, 2007.

List of Publications

Paper I:
Trends in low-temperature water-gas shift reactivity on transition metals
N. Schumacher, A. Boisen, S. Dahl, A.A. Gokhale, S. Kandoi, L.C.Grabow, J.A. Dumesic, M. Mavrikakis, I. Chorkendorff J. Catal, 229 (2005) 265.

Paper II:
Search for new catalysts from a fundamental basis
M. Andersen, O. Lytken, J. Engbæk, G. Nielsen, N. Schumacher, M. Johansson, I. Chorkendorff, Catal. Today 100, 191 (2005)

Paper III:
Support effects and catalytic trends for water gas shift activity of transition metals
A. Boisen, T.V.W. Janssens, N. Schumacher, I. Chorkendorff, S. Dahl, To be submitted

Paper IV:
Interaction of carbon dioxide with Cu overlayers on Pt(111)
N. Schumacher, K. Andersson, L. C. Grabow, M. Mavrikakis, J. Nerlov, I. Chorkendorff, Submitted to Surf. Sci.

Paper V:
Formate synthesis on Cu overlayers on Pt(111)
N. Schumacher, K. Andersson, J. Nerlov, I. Chorkendorff, To be submitted